



UNIVERSITÀ
DEGLI STUDI
FIRENZE

PhD in Atomic and Molecular Photonics

CYCLE XXXVII

COORDINATOR Prof. Diederik S. Wiersma

Kelvin-Helmholtz Instability in annular Fermi superfluids

Doctoral Candidate

Diego Hernandez Rajkov

Supervisor

Dr Giacomo Roati

Coordinator

Prof. Diederik S. Wiersma

Years 2021-2024

Abstract

In this thesis I investigate the onset and evolution of the Kelvin-Helmholtz instability in fermionic superfluids across the BEC-BCS crossover. The system involves two counter-rotating annular superflows separated by a thin potential barrier. Each annular superfluid holds an opposite-sign persistent current with the same number of circulation quanta. By tuning the barrier height, we control the merging dynamics of the superfluid, and observe how the interface deforms into an ordered array of quantized vortices, which then loses stability and rolls up into vortex clusters. The Kelvin-Helmholtz instability in superfluids can be seen as the instability breaking the symmetry of the regular array of vortices. Extracting the instability growth rates from the experimental data, we find that they obey the same scaling relations across the different superfluid regimes, although vortex dynamics appears to be consistently slower than predicted.

I performed the experimental results reported in this thesis, starting from the characterization of persistent currents, observation of the vortex arrays, developing the tracking and analysis tools to unveil the Kelvin-Helmholtz instability across the BEC-BCS crossover. I also developed the theoretical framework describing the instability using the dissipative point-vortex model. This model describes the motion of superfluid vortices in the presence of a mutual friction with the normal component of the system, and offers a mechanism through which vortex dynamics can be generally slower. Moreover, to provide more insights about the transition from the persistent currents to vortex arrays, we made use of the Gross-Pitaevskii equation, valid for the molecular BEC. The observed dynamics can be mapped to the ones of linear atomic Josephson junctions, explaining the emergence of the vortices as a natural solution to the merging problem.

These results link vortex arrays to shear flow instabilities. Our findings offer new perspectives on the Kelvin-Helmholtz instability in quantum fluids and provide a foundation for further studies in strongly correlated superfluids.

Contents

Abstract	ii
Dedication	v
Acknowledgments	vi
1 Introduction	1
1.1 Ultracold fermions as quantum simulators	1
1.2 Fermionic superfluidity	2
1.3 Thesis Overview	4
2 Basic theory of Fermi gases	6
2.1 Ideal Fermi gas	7
2.2 Interacting Fermi gases: BEC-BCS crossover	9
2.2.1 Tuning the interaction: Feshbach Resonances	11
2.2.2 The BEC-BCS crossover	13
2.2.3 Thermodynamic properties in the crossover	15
2.3 Superfluidity and quantum vortices	17
2.3.1 Superfluidity	17
2.3.2 Quantum vortices	19
2.3.3 Dynamics in a Bose-Einstein condensate	23
2.3.4 Two Fluid Model	24
2.4 Dissipative Point vortex model	25
2.4.1 Mapping to the complex plane	27
2.4.2 Point vortex model in finite systems	29
3 Kelvin-Helmholtz instability: from classical fluids to point vortex models	34
3.1 Classical Kelvin-Helmholtz instability	34

3.1.1	Kelvin-Helmholtz model	34
3.1.2	Rayleigh model	37
3.2	From the continuum to the discrete: Helmholtz's results	40
3.3	Instability of point vortex arrays	41
3.3.1	Instability of a row vortex array	41
3.3.2	Thickness of the interface layer	44
3.4	Kelvin-Helmholtz instability in superfluids	45
4	From persistent currents to vortex arrays in superfluids	47
4.1	Preparation of a superfluid gas ^6Li	48
4.1.1	Ultra-high vacuum system	48
4.1.2	Lithium in the presence of magnetic fields	49
4.1.3	Laser sources	51
4.1.4	Reaching quantum degeneracy	54
4.2	High-resolution imaging	56
4.2.1	Absorption imaging	56
4.2.2	Vertical imaging setup	58
4.3	Arbitrary optical potentials with DMD	59
4.3.1	DMD optical path	60
4.3.2	Controlling the DMD	61
4.4	Density excitations	62
4.5	Excitation of persistent current states	66
4.6	Counter-rotating superfluids: emergence of a vortex necklace	71
4.6.1	Concentric persistent currents	71
4.6.2	Merging of concentric superfluids	73
5	Kelvin-Helmholtz Instability in atomic superfluids	83
5.1	Vortex array temporal evolution	84
5.1.1	Breaking of the vortex array	84
5.2	Linear Stability analysis of a vortex necklace	86
5.2.1	Stability of the vortices polygon inside a circular boundary	87
5.2.2	Stability of the vortices polygon outside a circular boundary	90
5.2.3	Vortices inside an annular boundary	92
5.2.4	Finite α correction	94
5.3	Vortex ensemble trajectories	96

5.3.1	Deterministic of trajectories	96
5.3.2	Effect of vortex dissipation	101
5.4	Growth rate and dispersion relation	102
5.4.1	Vortex structure factor	102
5.4.2	Measured instability growth rate	105
5.4.3	Geometrical instability suppression	108
6	Conclusions and Outlook	110
	Bibliography	111

To my wife, Luzallie, my inspiration and the strongest person I know.

Acknowledgments

To my wife, Luzallie, whose constant support and love have been my greatest strength throughout this journey. Her resilience and encouragement have inspired me every step of the way, and I am endlessly grateful to have her by my side.

I am deeply grateful to Giacomo for his invaluable guidance, expertise, and unwavering support throughout this journey.

I would like to thank Nicola and Giulia for their camaraderie and insightful discussions, which made this journey productive, enjoyable and memorable.

A heartfelt thanks to Jorge and Giacomo for opening doors to invaluable opportunities and helping set the path for this and for future works together.

And finally, to my family.

Chapter 1

Introduction

1.1 Ultracold fermions as quantum simulators

The exploration of strongly interacting Fermi systems is a central endeavor in modern physics, bridging fields from condensed matter [1–3], to nuclear physics [4], and astrophysics [5]. When interactions within a fermionic system reach extreme strengths, the specific details of the system can be ignored, leading to universal behaviors that are shared by seemingly different systems [6] such as neutron matter in neutron stars, quark-gluon plasmas in the early universe [4]. Theoretical approaches to such systems face considerable obstacles due to the large correlations inherent to strong interactions, which challenge the conventional quasi-particle descriptions of the traditional many-body tools [6]. The complexity from the theoretical understanding is further compounded by the fermion sign problem, arising from the antisymmetric nature of fermionic wavefunctions, which greatly limits computational methods such as Monte Carlo simulations [7].

Quantum simulation offers an innovative route to addressing the challenges presented by these systems. Originally envisioned by Feynman [8], quantum simulation leverages simple experimentally controllable quantum systems to encapsulate the physics of much more complex systems, allowing the understanding of the physics involved in the complex quantum behaviors, and that would be otherwise difficult to access. Ultracold atomic gases, specifically ultracold fermions, have emerged as exceptionally adaptable quantum simulators over the past two decades, offering a unique level of control over the system parameters [9]. The overall potential landscape of these systems (dimensionality, confining potential, defects, etc...) can be

precisely engineered through the use of optical potentials, which can be designed at spatial resolutions close to the coherence length of the gas [10]. Additionally, atomic Feshbach resonances allow experimentalists to tune inter-particle interactions continuously, accessing both attractive and repulsive, weakly and strongly interacting regimes within the same system [9].

Ultracold fermions have been pivotal in realizing key theoretical models [6, 11], including the Bose-Hubbard [12] and Fermi-Hubbard models [13], and in exploring the crossover between Bose-Einstein condensate (BEC) and Bardeen-Cooper-Schrieffer (BCS) superfluidity [6, 11, 14]. The control over the atomic interactions enables the continuous transition from strong to weak interactions, allowing for direct comparison with well established theories like for a BEC and a BCS superfluids which are based on first principles. At the center of Feshbach resonances, ultracold Fermi gases reach quantum limited interactions [9], offering the possibility to access experimentally a system with universal properties that resemble phenomena seen in neutron stars and quark-gluon plasma.

Ultracold fermions, have established themselves as a fundamental tool for uncovering the intricate dynamics of strongly interacting quantum matter, illuminating pathways toward a deeper understanding of universal phenomena across multiple domains of physics.

1.2 Fermionic superfluidity

As a consequence of the strong interactions, ultracold Fermi gases behave as nearly perfect quantum fluids, with their hydrodynamic behavior determining both the equilibrium and the transport properties [15]. Understanding their behavior in precise and controlled situations could open new perspectives for simulating the hydrodynamical behavior of other strongly interacting systems. In particular, they provide a clean test bed to understand the similarities and differences between classical and quantum hydrodynamic behavior. One key feature that differentiates quantum from classical fluids is that the circulation of vortices in a quantum fluid is quantized [16]. These stable topological defects have a circulation that is quantized in units of h/m , where h is Planck's constant and m is the mass of the superfluid particle. Since the discovery of atomic superfluids, experiments with rotating gases across the BEC-BCS crossover have demonstrated the superfluid behavior through the observation of

quantized vortex lattices [17, 18].

Despite quantization of circulation, the emergence of classical phenomena from quantum vortex dynamics might be expected provided many quantum vortices of the same sign are bundled together, mimicking classical vortex tubes with arbitrary circulation. Additionally, many features of more complex behavior of many vortices systems are common to both classical and quantum fluids, such is the case for the emergence of turbulent dynamics [19, 20]. In three-dimensional system, quantum turbulence has been extensively studied in superfluid helium [21, 22], including the Kolmogorov energy cascade [23, 24], the dissipation anomaly [25], and boundary layers [26]. More recently, experimental advances in quasi two-dimensional ultracold atomic gases [27–31] and superfluid opto-mechanical systems with thin film helium [32] have renewed interest in turbulence and vortex dynamics in two dimensions, where contrastingly different behavior to three dimensions is often observed [22]. In two-dimensional quantum fluids analogues of classical phenomena such as the Von Karman vortex street [33, 34], vortex clustering [35–38], turbulent vortex relaxation [37, 39, 40], and negative temperature vortex equilibrium [39] have recently been demonstrated experimentally. Such experiments focused on the behavior of weakly interacting BEC and the mechanisms for relaxation after the injection of energy into the system [24]. However, the spontaneous appearance of non trivial vortex dynamics has been missing.

In classical fluids, the Kelvin-Helmholtz instability at the interface between two fluid layers flowing at different velocities (shear flow) is known to be a precursor for turbulent behavior, without requiring further excitation the system [20, 41–44]. Making the Kelvin-Helmholtz instability mechanism a new avenue for the exploration of the transition from superfluid shear flow to quantum turbulence. Experimental evidence of this phenomenon have only been regarded at the interface between two distinct superfluid phases He3 A and He3 B using indirect probes [45], lacking a clear vortex-by-vortex experimental observation. While the observation of this phenomenon in atomic gases has been attributed limited to the observation of the formation of vortices between two rotating BECs [46], a dynamical understanding of this phenomenon is lacking. A particular interest for studying this mechanism in unitary Fermi superfluids comes from the possibility to extrapolate some of the observed dynamics to rotating neutron stars, where superfluid shear flows are expected to be present [47, 48].

1.3 Thesis Overview

In this thesis I investigate the onset and evolution of the Kelvin-Helmholtz instability in fermionic superfluids across the BEC-BCS crossover [49]. The system involves two counter-rotating annular superflows separated by a thin potential barrier. Each annular superfluid holds an opposite-sign persistent current with the same number of circulation quanta. By tuning the barrier height, we control the merging dynamics of the superfluid, and observe how the interface deforms into an ordered array of quantized vortices, which then loses stability and rolls up into vortex clusters. The Kelvin-Helmholtz instability in superfluids can be seen as the instability breaking the symmetry of the regular array of vortices. Extracting the instability growth rates from the experimental data, we find that they obey the same scaling relations across the different superfluid regimes, although vortex dynamics appears to be consistently slower than predicted. These results link vortex arrays to shear flow instabilities, and offers new perspectives on Kelvin-Helmholtz instability in quantum fluids and provide a foundation for further studies in strongly correlated superfluids.

This thesis is organized as it follows:

- In Chapter 2, I provide an introduction to the general theoretical framework regarding strongly-interacting Fermi gases. After a short overview of low energy scattering and Feshbach resonances, I introduce the BEC-BCS crossover. Then, I focus on the general superfluid properties of those systems, namely the presence of a critical velocity below which excitations are not created in the system; and the presence of quantum vortices, and briefly introduce their dynamics in superfluids. Next, I introduce the two-fluid model firstly discuss for superfluid Helium, and comment how they modify the motion of quantum vortices in infinite and finite systems.
- In Chapter 3, I introduce the main topic of this thesis: the Kelvin-Helmholtz instability. I start with a brief summary of the derivation of the instability both sharp and smooth interface in classical fluids, introducing Kelvin-Helmholtz and Rayleigh results. Next, I discuss Helmholtz results of the modeling of the vorticity of classical fluids using point vortices, to latter derive the Kelvin-Helmholtz instability from this perspective. Finally, I discuss the extensions of this instability to the superfluid regime.

- In Chapter 4, I provide a description of our experimental setup, focusing on the methods for reaching quantum degeneracy, on the high-resolution microscope objective, and on the Digital Micromirror Device (DMD) that are implemented in the experimental setup, and which are fundamental to image the atomic cloud and imprint dynamical repulsive optical potentials with a sub-micron spatial resolution. Next, I present the phase imprinting protocol used for exciting persistent currents states in annular superfluids, and the interferometric measurement to detect the state of the system. Following the discussion, I describe our approach for generating the counter-flow between two superfluids, engineering two counter-rotating annular superfluids. Finally, I comment the dynamics occurring during the merging of both superfluids leading to the formation of a polygonal array of quantum vortices.
- In Chapter 5, I introduce the dynamics behind the breaking dynamics of the polygonal array of quantum vortices. I provide the experimental tools we employed to study the reliability of the system. I provide an in-depth discussion of the linear stability analysis polygonal array of vortices, showing their correspondence to the Kelvin-Helmholtz instability. Next, I show that the system is inherently sensitive to the initial conditions and displays a positive maximal Lyapunov exponent when analyzing the vortex trajectories. Finally, I compare the experimental data with the available models.

Chapter 2

Basic theory of Fermi gases

Fermions are ubiquitous in nature. They make up a significant portion of the matter in the universe, including electrons, protons, and neutrons. Understanding their behavior is crucial for unraveling many physical phenomena, from the properties of ordinary matter to the behavior of exotic states of matter. Their statistical nature leads to a variety of collective behaviors, making them a key focus in fields like condensed matter physics and quantum mechanics. Researching fermions in different scenarios can unlock new insights into quantum systems and their interactions.

Ultracold atomic gases offer the opportunity to study dilute systems where we have control over the interactions through magnetic Feshbach resonances. By adjusting the magnitude of the applied magnetic field near an atomic Feshbach resonance, the effective interaction between atoms can be tuned smoothly from strongly attractive to strongly repulsive.

In this chapter, I present the theoretical frame necessary for understanding the physics behind the experimental work realized in this thesis. In the first section, I summarize the main properties of a non-interacting Fermi gas and follow with interacting fermionic systems composed of two spin components. Starting from a review of scattering theory, I explain how interactions in the system can be manipulated externally through Feshbach resonances, introducing the BEC-BCS crossover.

In the last section, I present an overview of superfluidity and the special behavior of quantum vortices. Finally, I discuss the different models employed in this thesis to describe vortex dynamics, from the Gross-Pitaevskii equation to the dissipative point vortex model.

2.1 Ideal Fermi gas

To describe the thermodynamic properties of a system composed by fermions, let's consider the description in the grand-canonical ensemble. The system is in contact with a reservoir with which it can exchange particles and energy, the Fermi-Dirac distribution gives the average occupation of the state i of energy ε_i [14]:

$$\langle n_i \rangle = \frac{1}{e^{(\varepsilon_i - \mu)/(k_B T)} + 1}, \quad (2.1)$$

where μ is the chemical potential of the ensemble, k_B the Boltzmann constant, and T the temperature of the ensemble. In the zero temperature limit, the density of states is defined as unity up to the Fermi Energy, $E_F = \mu(T = 0)$, and null occupation for higher energies.

For a homogeneous Fermi gas, the average density is given by:

$$n = \int \langle n_i \rangle g(\varepsilon_i) d\varepsilon_i = \frac{1}{\lambda_T^3} \text{Li}_{3/2}(e^{\mu/k_B T}), \quad (2.2)$$

where $\lambda_T = \hbar/\sqrt{2\pi m k_B T}$ is the thermal De Broglie wavelength, with m the mass of the particle, and $\text{Li}_{3/2}(z)$ is the polylogarithmic function of order 3/2 defined as:

$$\text{Li}_\nu(z) = \sum_{k=1}^{\infty} \frac{z^k}{k^\nu}. \quad (2.3)$$

As temperature is lowered, λ_T increase, and it becomes of relevant importance when it is of the order of the mean inter-particle distance $n^{-1/3}$. In particular, when $n\lambda_T^3 \sim 1$ quantum degenerate regime is reached and quantum statistics play a huge role determining the properties of the system [14, 50].

Generally, ultracold gas experiments don't work with infinite homogeneous Fermi gas but with confined Fermi gases. In this case, the density is no longer homogeneous, but rather follows the behavior of the trapping potential V_{trap} . Assuming V_{trap} vary slowly on both the scale of the de Broglie wavelength λ_T , and the mean interparticle distance $n^{-1/3}$; we can take into account the inhomogeneities using the so-called local density approximation (LDA) [16]. Here, each volume, described by its position \mathbf{r} , is considered an independent homogeneous system, characterized by the local chemical

potential μ defined as

$$\mu(\mathbf{r}) = \mu_0 - V_{trap}(\mathbf{r}), \quad (2.4)$$

where μ_0 is the maximum chemical potential. Therefore, for trapped Fermi gases the average density follows:

$$n(\mathbf{r}) = \frac{1}{\lambda_T^3} \text{Li}_{3/2}(e^{(\mu_0 - V_{trap}(\mathbf{r}))/k_B T}). \quad (2.5)$$

In the present thesis, we are going to work with a trapping potential of the form:

$$V_{trap}(\mathbf{r}) = V_{box}(r, \theta) + \frac{1}{2} M \omega_z^2 z^2, \quad (2.6)$$

where $r = |\mathbf{r}|$ and θ are the radial and azimuthal coordinates, and the box potential V_{box} is defined as $V(r, \theta) = 0$ if r is inside the trap boundaries Ω and ∞ otherwise. In particular, in the experiments presented in this thesis V_{box} represents an annular box with internal and external radii R_i and R_e , as discussed in section 4.3.2. The vertical confinement set by ω_z is such that the system remain always in the three-dimensional regime regarding thermodynamic quantities. Moreover, the extent in the plane is much larger than the vertical extension of the system. Given this trapping potential, some of the system properties can be computed analytically, such as the Fermi energy. In the limit $T \rightarrow 0$, the density profile can be written as:

$$n(\mathbf{r}) = \frac{1}{3\pi^2} \left(\frac{2m}{\hbar^2} \right)^{3/2} (E_F - V_{trap}(\mathbf{r}))^{3/2}. \quad (2.7)$$

Integrating the density over the configuration space, we can obtain a relation between the Fermi energy and the total number of fermions in the system:

$$N = \frac{1}{3\pi} \left(\frac{2m}{\hbar} \right)^{3/2} \int (E_F - V_{trap}(\mathbf{r}))^{3/2} d\mathbf{r}. \quad (2.8)$$

For the specific trapping potential given by Eq. (2.6), the integral can be solved analytically, yielding:

$$E_F = \left[\frac{4\pi \hbar^3 \omega_z N}{mA} \right]^{1/2}, \quad (2.9)$$

where, A is the area defined in the x - y plane set by the box potential $V_{box}(r) = 0$.

For the potentials considered, A is the area of the annular box $A = n\pi(R_e^2 - R_i^2)$, see section 4.3.2. Notice the similarity of this expression of the one obtained from a 3D harmonically confined Fermi gas [14], where $E_F = (3\hbar^3\omega_x\omega_y\omega_zN)^{1/3}$, and to the one of a homogeneous gas [14]: $E_F = \frac{\hbar^2}{2m}(3\pi^2\frac{N}{V})^{2/3}$.

2.2 Interacting Fermi gases: BEC-BCS crossover

A system composed of two distinct spin fermions displays an even more exciting phase diagram depending on their interaction [6, 14]. Indeed as I'll discuss in the following sections interactions play a fundamental role in the emergence of superfluid behavior. For a non-interacting system, the ground state correspond to a two-spin Fermi Sea, where atoms occupy all the energy states below their respective Fermi Energy. From here on, we will only consider the case of a balanced mixture between both spin components, creating a common Fermi energy scale, E_F .

For attractive interactions, correlations within the system allow for the formation of Cooper pairs at the surface of the Fermi Sea [14]. This phenomenon, similar to superconductors, is at the origin of fermionic superfluidity below a certain critical temperature. On the other hand, repulsive interactions between fermions can lead to the formation of weakly bound molecules, which are composite bosons. As per usual bosonic particles, below a certain critical temperature they can undergo Bose-Einstein condensation [16, 50], displaying bosonic superfluid behavior.

In dilute gases at low temperatures, the interaction between distinguishable fermions can be described by a small number of parameters that emerge from the description of a two-body collision analysis. The scattering process can be solved using the Schrödinger equation in the center-of-mass frame of reference [51]:

$$\left[-\frac{\hbar^2}{2m^*}\nabla^2 + U(\mathbf{r}) \right] \Psi(\mathbf{r}) = E\Psi(\mathbf{r}), \quad (2.10)$$

where $m^* = m_1m_2/(m_1 + m_2)$ is the reduced mass, \mathbf{r} is the relative position, $U(\mathbf{r})$ describes the interatomic potential, and $E = \frac{\hbar^2k^2}{2m^*}$ is the collision energy. The complete solution of the Schrödinger equation strongly depends on the interatomic potential $U(\mathbf{r})$. However, when $U(\mathbf{r})$ has a finite range r_u , we can obtain some insights of the solution simply by looking at the behavior of Ψ in the far field, $r \gg r_u$. The wavefunction Ψ can be decomposed in the superposition of an incoming wave, $e^{i\mathbf{k}\cdot\mathbf{r}}$,

and a scattered wave. For 3D systems, the outgoing scattered wave can be written as a modulated spherical wave [51]: $f(\theta, \phi) \frac{e^{ikr}}{r}$, where f indicates the scattering amplitude. The later is connected to the differential scattering cross-section by $\frac{d\sigma}{d\Omega} = \frac{4\pi}{k^2} |f(\theta, \phi)|^2$, with Ω the solid angle.

By considering an isotropic inter-atomic potential, we can make use of the symmetries of the problem, namely the azimuthal invariance, and expand the wavefunction into partial waves:

$$\Psi(r, \theta, \phi) = \sum_{l=0}^{\infty} Y_l^0(\theta) \frac{u_{kl}(r)}{r}, \quad (2.11)$$

where Y_l^0 are the spherical harmonics of degree l and order 0, and $u_{kl}(r)$ the corresponding radial wavefunction, that depends on the incoming momentum k . For every partial wave, with a well-defined angular momentum l , there is an independent Schrödinger equation with a potential given by the sum of the inter-atomic potential and the repulsive centrifugal barrier:

$$\left[-\frac{d^2}{dr^2} - k^2 + \frac{l(l+1)}{r^2} + \frac{2\mu}{\hbar^2} U(\mathbf{r}) \right] u(r) = 0. \quad (2.12)$$

In a low-temperature regime, only the lowest angular momenta components contribute to the scattering processes. The reason is that when the kinetic energy is much lower than the height of the centrifugal barrier the incoming particle is reflected, ignoring the details of the potential. Moreover, for identical fermions, the antisymmetric nature of the wavefunction allows only for odd values of l in the partial wave expansion. Therefore, the lowest scattering wave contribution is given by the p-wave $l = 1$, which is fully suppressed at sufficiently low temperatures [52].

In the ultra-cold regime, identical fermions behave like as the non-interacting Fermi gas discussed previously. For this reason, we consider the problem of a mixture of distinguishable fermions. The scattering between the same spin components is suppressed, while the scattering between distinct components isn't. In fact, for different spin components, the interaction is uniquely characterized by the lowest scattering $l = 0$ s-wave properties.

The solution to the Schrödinger equation for the s-wave scattering at large dis-

tances, $r \gg k^{-1}$, can be approximated by:

$$u(r) \sim \frac{1}{\cos \delta_0(k)} \sin(kr - \delta_0(k)), \quad (2.13)$$

where $\delta_0(k)$ correspond to the s-wave phase shift. In the low-energy limit, the scattering amplitude can be rewritten as [14]:

$$f(r) = \frac{1}{k \cot \delta_0(k) + ik} \sim \frac{1}{a^{-1} + \frac{1}{2}r_e k^2 + ik}, \quad (2.14)$$

where we introduced the effective range r_e , which depends on the details of the interaction potential, and the scattering length a defined as:

$$a = -\lim_{k \rightarrow 0} \frac{\tan \delta_0(k)}{k}. \quad (2.15)$$

Finally, the s-wave scattering cross-section between distinguishable fermions for vanishing momentum is [14]:

$$\sigma = \frac{4\pi a^2}{1 + k^2 a^2} = \frac{4\pi}{a^{-2} + k^2}. \quad (2.16)$$

In this scenario, the scattering cross-section can be interpreted *classically* as the collision between two spheres of radius $a/\sqrt{1 + k^2 a^2}$. In the limit when a is small such that the collision term $ka \ll 1$, the radius of the fictitious spheres coincides with the scattering length, and is independent of the incoming momentum. On the contrary, when the scattering length diverges, the cross-section is maximum $\sigma = 4\pi k^{-2}$, and strongly depends on the incoming momentum.

2.2.1 Tuning the interaction: Feshbach Resonances

The scattering length a so far can be described purely by the far field behavior of the collision process. However, a more detailed description of a can be obtained after considering the atomic internal structure [9, 14]. Due to the coupling between different hyperfine states, the scattering process can couple different inter-atomic potentials for the incoming and outgoing waves. This additional degree of freedom in the collision gives rise to the well-known Feshbach resonances [9, 14]. The description of such collisions resonances was first made in the context of nuclear collisions.

For ultra-cold systems, at low energy, the magnetic Feshbach resonance appears when considering the collision in the presence of an external bias magnetic field [9]. Due to the different magnetic moments associated to each of the possible hyperfine pairs ($\Delta\mu = \mu_2 - \mu_1 \neq 0$), the relative separation between the inter-atomic potentials can be tuned externally $\Delta E \propto \Delta\mu B$. In particular, for alkali atoms, these correspond to the singlet and triplet configuration of the valence electron spin, see Figure 2.1a.

The scattering process can couple such hyperfine pairs when a resonant condition is met. For convention [9], let us define the open channel as the incoming inter-atomic potential and the closed channel as the second out going inter-atomic potential. Whenever the bound state of the closed channel is close to the collision energy corresponding to the threshold energy of the open channel energy (see Figure 2.1a), the coupling between both channels becomes significantly greater [9]. Indeed, the crossing of the closed channel bound states and the collision energy gives rise to the Feshbach resonance. Close to it, the scattering length is well approximated by [9]:

$$a_s(B) = a_{bg} \left(1 - \frac{\Delta}{B - B_0} \right), \quad (2.17)$$

where Δ is the magnetic resonance width, B_0 is the magnetic field where the crossing occurs (the center of the resonance), and a_{bg} is the off-resonance background scattering length. The Feshbach resonances between all pairs of the three lowest hyperfine states of ${}^6\text{Li}$ are shown in Figure 2.1b. These resonances are extremely large ($\Delta \approx 300\text{G}$) compared with other atomic species [9] making lithium one of the most versatile species for tuning the interaction, without extreme stabilization of the magnetic fields.

From Eq. (2.17) and Figure 2.1b, it is clear that we can exploit the magnetic Feshbach resonances to tune from attractive to repulsive, and from weak to strongly interacting regimes [14]. More importantly, Feshbach resonances allow us to change the fundamental constituents of our system. Whenever, the energy of the close channel bound state is lower than the collision energy, the bound state can be populated, forming weakly bound molecules. The binding energy is $E_b = -\frac{\hbar^2}{ma^2}$ [9]. The weakly bound molecules form when the scattering length is positive, i.e. repulsive interactions, and display a bosonic character. Below a critical temperature they can condense into a Bose-Einstein condensate (BEC) of molecules [54]. Instead, when the energy of the close channel bound state is higher than the collision energy, the system remains behave as having attractive interactions. In this case, fermions with opposite spin and momentum can form Cooper pairs, and the system is described by

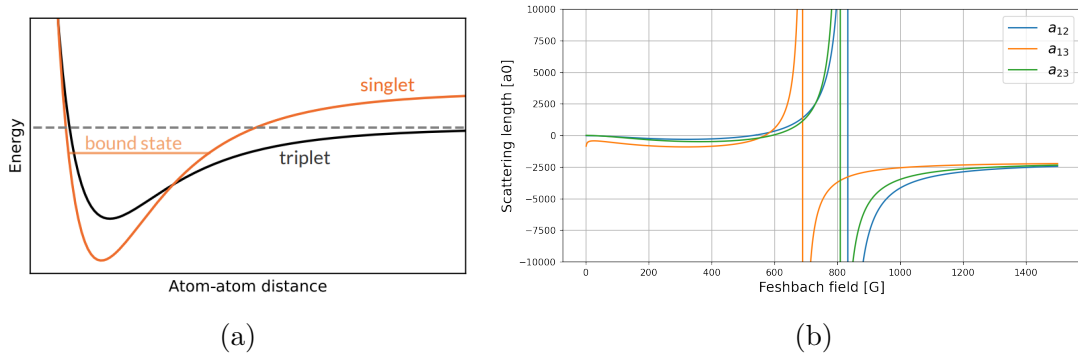


Figure 2.1: a) Triplet (open channel) and singlet (closed channel) scattering potential for two colliding atoms. The singlet scattering potential energy can be shifted by applying a bias magnetic field. The Feshbach resonance occurs when the bound state energy coincides with the collision energy (dashed line), Image taken from [53]. b) Feshbach resonances between the three lowest hyperfine states of ${}^6\text{Li}$.

the Bardeen-Cooper-Schrieffer (BCS) theory. Finally, the regime where the scattering length diverges, the energy of the bound state is at threshold $E_b \rightarrow 0$, and as mentioned before, the scattering cross-section reaches a maximum with $\sigma = 4\pi k^{-2}$. In this peculiar situation, there are only two length scales in the system, the mean inter-particle distance, or simple k_F^{-1} and the thermal de Broglie wavelength λ_T . This system, known as a Unitary Fermi gas (UFG), or unitary regime is expected to behave as an intermediate state having both bosonic and fermionic characteristic [6, 55], with all the thermodynamics properties being only a function of $n\lambda_T^3$ or equivalently T/T_F .

2.2.2 The BEC-BCS crossover

The possibility of changing the inter-atomic interaction by varying an external bias magnetic field makes ultracold atoms the perfect system for studying many-body physics such as superfluidity. Moreover, the BEC-BCS crossover allows the possibility of tuning the underlying quantum statistics giving origin to the superfluid behavior. From the BEC side, having bosonic statistics to the unitary and BCS side with fermionic statistics.

To describe the distinct interaction regimes, it is essential to parameterize the interaction coupling within the system using a single parameter [6, 11]. The two main parameters describing the interaction strength are the system's density and

the s-wave scattering length. With these parameters, it is possible to construct the dimensionless parameter $(k_F a)^{-1}$. For temperatures below the Fermi temperature, it is possible to distinguish between three distinct regimes:

- $1/k_F a > 1$: In this regime, atoms with different spin states couple together and form tightly bound molecules. The system behaves like a bosonic one and can undergo a phase transition into a Bose-Einstein condensate (BEC) when the temperature is below the critical temperature. However, quantum depletion effects modify the behavior of the condensed fraction for decreasing $1/k_F a$. In the limit $1/k_F a \rightarrow \infty$, the mean-field chemical potential can be approximated as

$$\mu_{BEC} = -\frac{\hbar^2}{2ma^2} + \frac{4\pi\hbar^2 a_M n_M}{2m}, \quad (2.18)$$

with $a_M = 0.6a$ the dimer-dimer scattering length [51], and n_M the molecular density. The first term represents the binding energy per fermion, while the second reflects the bosonic two fermion mean-field repulsion.

- $1/k_F a \ll -1$: In this regime, the atoms form long-range Cooper pairs-like described by the Bardeen-Cooper-Schrieffer (BCS) theory. In principle, the system can undergo a superfluid transition when the temperature is below the critical temperature. In this regime, the Cooper pairs have a characteristic size larger than the inter-particle spacing of the gas. In the limit $1/k_F a \rightarrow -\infty$, the mean-field chemical potential becomes the Fermi energy E_F , and the order parameter is the superconducting gap, Δ , that is characterized by [14]:

$$\Delta = \frac{8}{e^2} e^{-\frac{\pi}{2k_F |a|}}. \quad (2.19)$$

- $-1 < 1/k_F a < 1$: This regime is known as the BEC-BCS crossover, and shares similarities with both BEC and BCS regimes. Like the BCS regime, it is characterized by the formation of Cooper pairs but the pair size is comparable with the inter-particle spacing. The mean-field chemical potential correspond to a smooth transition from E_F towards μ_{BEC} [11]. At unitarity, $\frac{1}{k_F a} = 0$, the local chemical potential takes the form $\mu = \xi \epsilon_F$, where $\xi \approx 0.37$ is the Bertsch parameter [6].

2.2.3 Thermodynamic properties in the crossover

To evaluate some thermodynamic properties of the superfluids using a common framework throughout the BEC-BCS crossover we exploit the polytropic approximation to describe the chemical potential as function of the density [56, 57]. The polytropic index $\gamma = \partial \log \mu / \partial \log n$ defines the power-law relation $\mu \propto n^\gamma$ [56, 57]. For instance, in the BEC-limit, $\gamma = 1$, while at unitarity and in the BCS-limit, $\gamma = 2/3$. The polytropic approximation enables us to evaluate analytically μ and E_F of the crossover superfluids considering the vertical harmonic confinement and the hard-wall potential in the x - y plane.

Assuming the LDA, the Thomas-Fermi density profile is given by:

$$n(\mathbf{r}) = \left[\max \left(0, \frac{\mu - V_{box}(\mathbf{r})}{g_\gamma} \right) \right]^{1/\gamma}, \quad (2.20)$$

where the total potential is given by Eq. (2.6). The mean-field interaction, is characterized by the parameter g_γ through the relation $\mu = g_\gamma n^\gamma$. The total atom number N is given by the integral of the density over space:

$$N = \int n(\mathbf{r}) d^3 \mathbf{r} = \left(\frac{\mu}{g_\gamma} \right)^{1/\gamma} \int \left[\max \left(0, 1 - U_{box}(\mathbf{r}) \right) \right]^{1/\gamma} d^3 \mathbf{r}. \quad (2.21)$$

Where $U_{box}(\mathbf{r}) = V_{box}(\mathbf{r})/\mu$. Integrating over the potential, we arrive to the following expression:

$$N = \left(\frac{\mu}{g_\gamma} \right)^{1/\gamma} \frac{\pi^{1/2} \Gamma(\frac{1}{\gamma} + 1)}{\Gamma(\frac{1}{\gamma} + \frac{3}{2})} A R_z, \quad (2.22)$$

where $\Gamma(x)$ is the Gamma function, A is the area defined in the x - y plane set by the box potential $V_{box}(r) = 0$, $R_z = \sqrt{\frac{2\mu}{M\omega_z^2}}$ defines the Thomas-Fermi radius of the cloud along the vertical direction, and $M = 2m$ the mass of the pairs. Inverting the expression to obtain the chemical potential we get:

$$\mu = \left[\frac{\Gamma(\frac{1}{\gamma} + \frac{3}{2})}{\pi^{1/2} \Gamma(\frac{1}{\gamma} + 1)} \frac{\sqrt{M/2\omega_z} N g_\gamma^{1/\gamma}}{A} \right]^{\frac{2\gamma}{\gamma+2}}. \quad (2.23)$$

Properties	BEC limit ($k_F a_s)^{-1} > 1$	Unitarity ($k_F a_s)^{-1} = 0$	BCS limit ($k_F a_s)^{-1} < -1$
γ (in $\mu = g_\gamma n^\gamma$)	1	2/3	2/3
g_γ (in $\mu = g_\gamma n^\gamma$)	$\frac{4\pi\hbar^2 a_M}{M}$	$\xi \frac{\hbar^2}{2m} (6\pi^2)^{2/3}$	$\frac{\hbar^2}{2m} (6\pi^2)^{2/3}$
$\eta_\gamma = \frac{\Gamma(\frac{1}{\gamma} + \frac{3}{2})}{\pi^{3/2} \Gamma(\frac{1}{\gamma} + 1)}$	$\frac{3}{4\pi}$	$\frac{8}{3\pi^2}$	$\frac{8}{3\pi^2}$
(2D-Homogeneous + 1D Harmonic) trap			
Chemical potential	$\mu_M = \left[\frac{3}{2} \frac{\hbar^2 \omega_z N_\uparrow a_M}{\sqrt{m(R_0^2 - R_\uparrow^2)}} \right]^{2/3}$	$\xi^{3/4} E_F = \xi^{3/4} \left[\frac{4\hbar^3 \omega_z N_\uparrow}{m(R_0^2 - R_\uparrow^2)} \right]^{1/2}$	$E_F = \left[\frac{4\hbar^3 \omega_z N_\uparrow}{m(R_0^2 - R_\uparrow^2)} \right]^{1/2}$
Thomas Fermi radius i-th direction	$R_{BEC,i} = \sqrt{\frac{2\mu_M}{M\omega_i^2}}$	$R_{UFG,i} = \xi^{3/8} \sqrt{\frac{2E_F}{m\omega_i^2}}$	$R_{BCS,i} = \sqrt{\frac{2E_F}{m\omega_i^2}}$
Density profile: $n_\uparrow(\vec{r})/n_\uparrow^{peak}$	$1 - U_{box} - \frac{z^2}{R_{BEC,z}^2}$	$\left(1 - U_{box} - \frac{z^2}{R_{UFG,z}^2} \right)^{3/2}$	$\left(1 - U_{box} - \frac{z^2}{R_{BCS,r}^2} \right)^{3/2}$
Peak density: n_\uparrow^{peak}	$\frac{M\mu_M}{4\pi\hbar^2 a_M}$	$\left(\frac{\xi^{-1/4} E_F}{\frac{\hbar^2}{2m} (6\pi^2)^{2/3}} \right)^{3/2}$	$\left(\frac{E_F}{\frac{\hbar^2}{2m} (6\pi^2)^{2/3}} \right)^{3/2}$
Normalized speed of sound (c_s/v_F)	$\left(\frac{3}{2} \frac{k_F a_M}{2} \right)^{1/3}$	$\sqrt{\frac{\xi^{3/4}}{3}}$	$\frac{1}{\sqrt{3}}$
(3D-Harmonic) trap			
Chemical potential	$\mu_M = \frac{\hbar\bar{\omega}}{2} \left(\frac{15N_\uparrow a_M}{\sqrt{\hbar/M\bar{\omega}}} \right)^{2/5}$	$\xi^{1/2} E_F = \xi^{1/2} \hbar\bar{\omega} (6N_\uparrow)^{1/3}$	$E_F = \hbar\bar{\omega} (6N_\uparrow)^{1/3}$
Thomas Fermi radius i-th direction	$R_{BEC,i} = \sqrt{\frac{2\mu_M}{M\omega_i^2}}$	$R_{UFG,i} = \xi^{1/4} \sqrt{\frac{2E_F}{m\omega_i^2}}$	$R_{BCS,i} = \sqrt{\frac{2E_F}{m\omega_i^2}}$
Density profile: $n_\uparrow(\vec{r})/n_\uparrow(\vec{0})$	$1 - \frac{r^2}{R_{BEC,r}^2} - \frac{z^2}{R_{BEC,z}^2}$	$\left(1 - \frac{r^2}{R_{UFG,r}^2} - \frac{z^2}{R_{UFG,z}^2} \right)^{3/2}$	$\left(1 - \frac{r^2}{R_{BCS,r}^2} - \frac{z^2}{R_{BCS,r}^2} \right)^{3/2}$
Peak density: $n_\uparrow(\vec{0})$	$\frac{15}{8\pi} \frac{N_\uparrow}{R_{BEC,x} R_{BEC,y} R_{BEC,z}}$	$\frac{8}{\pi^2} \frac{N_\uparrow}{R_{UFG,x} R_{UFG,y} R_{UFG,z}}$	$\frac{8}{\pi^2} \frac{N_\uparrow}{R_{BCS,x} R_{BCS,y} R_{BCS,z}}$
Normalized speed of sound (c_s/v_F)	$\frac{1}{2^{3/2}} \left(\frac{5k_F a_M}{2} \right)^{1/5}$	$\sqrt{\frac{\xi^{1/2}}{3}}$	$\frac{1}{\sqrt{3}}$
(3D-Homogeneous)			
Chemical potential	$\mu_M = \frac{4\pi\hbar^2 a_M}{M} n_\uparrow$	$\xi E_F = \xi \frac{\hbar^2}{2m} (6\pi^2 n_\uparrow)^{2/3}$	$E_F = \frac{\hbar^2}{2m} (6\pi^2 n_\uparrow)^{2/3}$
Normalized speed of sound (c_s/v_F)	$\sqrt{\frac{k_F a_M}{3\pi}}$	$\sqrt{\frac{\xi}{3}}$	$\frac{1}{\sqrt{3}}$

Table 2.1: Zero-temperature density profiles of a trapped, interacting Fermi mixture in the BEC-BCS crossover.

To estimate the speed of sound we make use the standard definition provided by:

$$c_s = \sqrt{\frac{n}{M} \frac{\partial \mu}{\partial n}} = \sqrt{\gamma \frac{\mu}{M}}. \quad (2.24)$$

To apply the polytropic approximation to different scenarios I summarize the relevant quantities in Table 2.1, together with a quick description to apply for each scenario:

- In the BEC regime: the polytropic exponent is $\gamma = 1$, and the interaction parameter is $g_{BEC} = \frac{4\pi\hbar^2 a_M}{M}$. Where $a_M \approx 0.6a_s$ is the molecular scattering length, and $M = 2m$ is the mass of the pairs.
- In the UFG regime: $\mu(n) = \xi \epsilon_F(n) \propto n^{2/3}$ hence the polytropic exponent $\gamma = 2/3$, and the interaction parameter is $g_{UFG} = \xi \frac{\hbar^2}{2m} (6\pi^2)^{2/3}$, with ξ the

Bertsch parameter, that can be temperature dependent: $\xi = \xi(T/T_F)$.

- In the deep-BCS regime: $\mu(n) = \epsilon_F(n) \propto n^{2/3}$ hence the polytropic exponent $\gamma = 2/3$, and the interaction parameter is $g_{BCS} = \frac{\hbar^2}{2m}(6\pi^2)^{2/3}$.

2.3 Superfluidity and quantum vortices

2.3.1 Superfluidity

Superfluidity is a unique property of fluids that emerges at extremely low temperatures. This phenomenon was first observed by P. Kapitza [58], and independently by J. F. Allen and D. Misener [59] in two papers published side-by-side in the January 1938. Making measurements on liquid helium flowing through a narrow opening, they found that at $T_\lambda = 2.17K$ the helium flowed with incredible ease, compelling Kapitza to make the analogy with the low resistance of superconductors, coining the term superfluid. The discovery of superfluidity and the development of theories explaining its remarkable behavior fundamentally changed our understanding of quantum mechanics. An early theoretical advance in understanding superfluidity was provided by Tisza's two fluid model [60], in which superfluids are modeled as two separate components, a normal fluid carrying all the system's entropy, and a zero entropy, zero viscosity superfluid component. The presence of a second fluid acts as a new collective degree of freedom, allowing the coherent movement without friction.

The ideas of Tisza were further developed by L.Landau to provide the first phenomenological model of superfluidity. Landau showed that for certain dispersion relations, excitations in a superfluid cannot be created by a moving obstacle if the obstacle is moving below a certain velocity. This velocity, known as the critical velocity v_c , can be derived by considering a obstacle moving through the superfluid at some velocity \mathbf{v}_i and momentum \mathbf{p} . Let us consider an excitation with energy $\hbar\omega_{\mathbf{k}}$ and momentum \mathbf{k} created by the obstacle as it moves through the fluid. Under conservation of energy and momentum, we have

$$\frac{1}{2}mv_i^2 = \frac{1}{2}Mv_f^2 + \hbar\omega_{\mathbf{k}}, \quad \mathbf{p}_i = \mathbf{p}_f + \hbar\mathbf{k}, \quad (2.25)$$

where m is the mass of the obstacle. To provide a lower limit on \mathbf{v}_i to create such an

excitation, we combine the above equations to find

$$\hbar\omega_k = \hbar\mathbf{k} \cdot \mathbf{v}_i - \frac{\hbar^2 k^2}{2M} \quad (2.26)$$

For impurities with a large mass, the second term can be assumed sufficiently small such that the minimum velocity required to create an excitation is bound by the wavevector of the excitation

$$v_i \geq \frac{\omega_k}{k}. \quad (2.27)$$

Given that the above constraint can take different values for different k , the Landau criterion is shown to be

$$v_c \geq \min \frac{\varepsilon(\mathbf{k})}{\hbar|\mathbf{k}|} \quad (2.28)$$

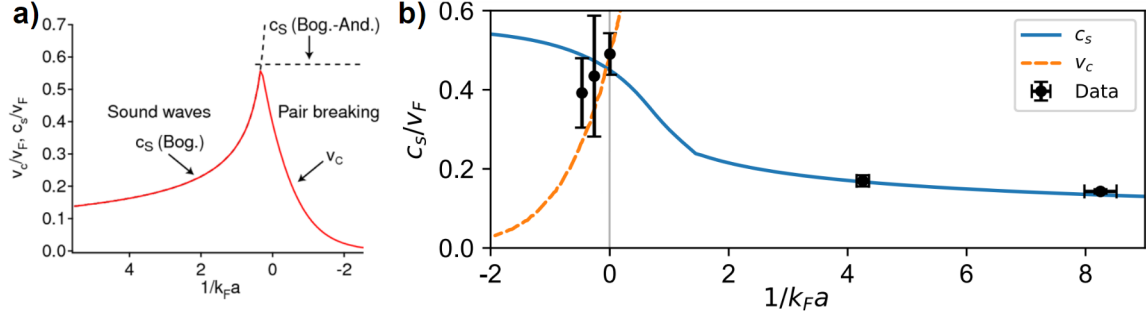


Figure 2.2: a) Critical velocity v_c in the BEC-BCS crossover. In the BEC side the critical velocity is given by the speed of sound, while in the BCS limit destruction of Cooper pairs limit the maximum velocity for the superflow. Image taken from [14] b) Experimentally measured curve of a density excitation across the crossover (see section 4.4).

where $\varepsilon(\mathbf{k})$ is the excitation spectrum. For velocities below v_c , the obstacle will move through the superfluid without resistance, creating zero excitations as it moves. This apparently simple calculation underpins the most fundamental property of superfluidity. The condition set by v_c defines whether a system's dispersion relation can lead to the system to be a superfluid, which only depends on the allowed excitations from the excitation spectrum.

For the weakly interacting Bose gas, with spectrum [16]

$$\varepsilon(\mathbf{k}) = \sqrt{\frac{\hbar^2 k^2}{2m} \left(\frac{\hbar^2 k^2}{2m} + 2gn \right)}, \quad (2.29)$$

the critical velocity equal the the speed of sound of the system, $v_c = c_s = \sqrt{gn/m}$. For Cooper pairs in a BCS gas, with spectrum [14]

$$\varepsilon(\mathbf{k}) = \sqrt{\left(\frac{\hbar^2 k^2}{2m} - \mu\right)^2 + \Delta^2}, \quad (2.30)$$

the critical velocity can be estimated from the deep-BCS side [6]:

$$v_c = \frac{\Delta}{\hbar k_F}. \quad (2.31)$$

An object that is dragged through the superfluid faster than this velocity will break the fermion pairs. Note that in both the BEC and BCS regimes, the critical velocity increases together with the interactions [61, 62], see Figure 2.2.

2.3.2 Quantum vortices

The most dramatic demonstration of superfluid behavior is the presence of quantized vortices in rotating systems [17, 18], see Figure 2.3. The same phenomenon can be observed by considering type II superconductors in the presence of a magnetic field [63], see Figure 2.3. More recently, quantum vortices have been experimentally observation in rotating quantum dipolar condensates and supersolids [64–66]. In general, superfluids are described using a complex macroscopic wavefunction that must be single-valued in real space. Using the Madelung representation of the wavefunction:

$$\psi(\mathbf{r}, t) = \sqrt{n(\mathbf{r}, t)} e^{i\phi(\mathbf{r}, t)}, \quad (2.32)$$

with $n(\mathbf{r}, t)$ represents the atomic density and $\phi(\mathbf{r}, t)$ the phase. The superfluid velocity is obtained from the quantum mechanical definition of the current, yielding:

$$\mathbf{v} = \frac{\hbar}{M} \nabla \phi. \quad (2.33)$$

where $M = 2m$ for fermionic superfluids. Since the velocity field of a superfluid is derived from the gradient of ϕ , it is curl-free ($\nabla \times \mathbf{v} = 0$), and therefore, it display irrotational flows. And under rotation, the circulation of the superfluid is set to follow:

$$\Gamma = \oint \mathbf{v}_s \cdot d\mathbf{l} = \frac{\hbar}{M} \oint \nabla \phi \cdot d\mathbf{l} = \kappa n, \quad (2.34)$$

where $\kappa = h/M$ is the quantum of circulation, and n an integer number. The quantized vortex solution must be associated with a singularity in phase, where phase wraps of a multiple of $2\pi n$ around the vortex core, while at the singularity the order parameter must vanishes.

Contrary to classical vortices, increasing the vorticity of a single quantum vortex leads instead to an energetically instability [16]. High winding number vortices carry a energy proportional to n^2 . For instance, a doubly quantized vortex with $n = 2$ will cost 2 times the energy cost of two single-quanta vortices with $n = 1$. This instability, will eventually make multi-charged vortices to decay into single-quanta vortices [16], see Figure 2.3. Recently many proposals are trying to understand the decay process, eventually leading to different decay mechanisms [16, 67].

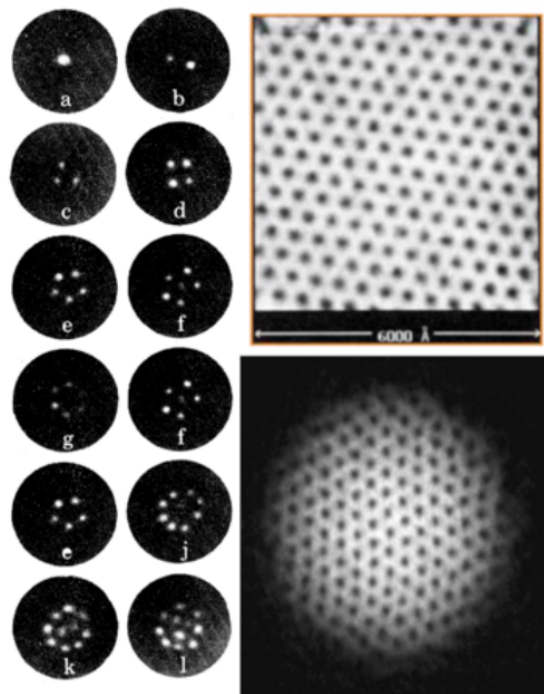


Figure 2.3: Quantized vortices in vortex lattices. The images are from liquid 4He, left [68], in a lattice of supercurrent flow, top right [69], and atomic in BECs bottom right [17]

The core size of a vortex is on the order of the coherence length ξ . In the BEC regime, this corresponds to the healing length $\xi = \sqrt{\frac{\hbar^2}{Mgn}}$, with g the interaction parameter, and n the background density. In the unitary and BCS regimes, the

vortex core size is better described in terms of the energy gap [14]:

$$\xi \sim \frac{\hbar^2 k_F}{m\pi\Delta}, \quad (2.35)$$

where $v_F = \sqrt{2E_F}/m$ is the Fermi velocity. Quantum vortices in 3D systems are typically described in terms of *line vortices*, along which the phase winds around it. Such *line vortices* can be curves bending over space. When they form a straight line, they are generally unstable against perturbations inhibiting them to remain straight. These excitations, known as a Kelvin waves, correspond to helical excitations on the vortex line path, and is among the most fundamental excitations in vortices [70]. However, Kelvin waves can be suppressed. One such scenario is the suppression induced by confinement of the system along the vortex line direction [71], the limiting case being *point vortices* in two dimensions [71, 72]. In the quasi-2D regime, where vortex bending is fully suppressed, vortices have a well-defined circulation direction, the flow rotates either clockwise or anticlockwise, and is defined by the sign of their corresponding winding number. In this regime, the description of the vortices simplifies considerably since no bending stress is to be accounted for [72].

To describe a system composed of multiple vortices it is convenient to provide a simple description of the velocity flow around single vortices. Starting from the definition of the circulation:

$$\Gamma = \oint_{\partial\Omega} \mathbf{v}_s \cdot d\mathbf{l} = \int_{\Omega} \nabla \times \mathbf{v}_s \cdot d\mathbf{S} = \int_{\Omega} \vec{\omega} \cdot d\mathbf{S} = \kappa n \quad (2.36)$$

we define the vorticity field as $\vec{\omega}(\mathbf{r}) = \nabla \times \mathbf{v}_s$. We can model the large distance flow of vortices, ignoring the specific details inside the vortex core by considering concentric trajectories $\partial\Omega$ centered on the vortex with radii larger than ξ . We motivate this approximation since the mass current around the vortex dramatically change inside the core due to the vanishing density [16]. Far from the vortex core ($|\mathbf{r} - \mathbf{r}_0| \gg \xi$), the vorticity can be modeled as:

$$\vec{\omega}(\mathbf{r}) \approx \kappa n \hat{z} \delta^2(|\mathbf{r} - \mathbf{r}_0|). \quad (2.37)$$

Assuming concentric paths located at radius r from \mathbf{r}_0 , and imposing a symmetric

solutions of the form $\mathbf{v}_s(\mathbf{r}, \theta) = \mathbf{v}_s(\mathbf{r})$, the velocity field is given by:

$$\mathbf{v}_s(\mathbf{r}) \approx \frac{\kappa n}{2\pi|\mathbf{r} - \mathbf{r}_0|} \hat{\theta}. \quad (2.38)$$

where $\hat{\theta}$ is the polar coordinate unit vector for a coordinate system centered on the vortex core. Since the vorticity and velocity profile of a quantum vortex can be mapped to point vortices, under the correct conditions quantum vortices should behave like a gas of point vortices [72]. Moreover, when the inter-vortex spacing is larger than a few ξ , at least $l_v \xi \gg 2$, and when vortex bending is suppressed, the superfluid velocity can be approximated as the addition of each vortex flow [72]:

$$\mathbf{v}_s(\mathbf{r}) \approx \frac{\kappa}{2\pi} \sum_j^{N_v} \frac{n_j}{|\mathbf{r} - \mathbf{r}_j|} \hat{\theta}_j, \quad \text{where} \quad \hat{\theta}_j = \hat{z} \times \frac{\mathbf{r} - \mathbf{r}_j}{|\mathbf{r} - \mathbf{r}_j|}. \quad (2.39)$$

For typical experimental setups employing quasi two-dimensional confinement [34, 38–40, 73], or working with highly oblate potentials, this approximation is valid. Examples where this approximation is no longer valid are the vortex-antivortex annihilation dynamics [73], or the splitting of a multi-charged vortex. In the former case, the dynamics cannot be described faithfully once the vortices get closer than 10ξ [73], the reason being that the energy in the system is concentrated in compressible energy, and no longer kinetic energy, as provided by the point vortices.

Moreover, vortex dynamics in homogeneous superfluids, can be computed from the force the superfluid exert on the vortices [16, 74, 75], namely the Magnus force:

$$\mathbf{F}_M^i = \kappa \rho_s (\mathbf{v}_s^* - \mathbf{v}_L^i) \times \hat{z} \quad (2.40)$$

where \mathbf{v}_L^i is the velocity of the i -th vortex, and \mathbf{v}_s^* , is the average superfluid velocity in the vicinity of the vortex. Note that \mathbf{v}_s^* can be expressed from the superfluid and velocity fields [75, 76], $\mathbf{v}_s^* = \mathbf{v}_s - \mathcal{V}_i$, where \mathcal{V}_i is the contribution to the velocity field of the i -th vortex given by equation (2.38). The motion of the vortex is set by the balance of forces acting on it, namely $\sum_i \mathbf{F}_i = 0$ (assuming massless vortices, in the next section I discuss the scenario also considering massive vortices where $\sum_i \mathbf{F}_i = \frac{dP}{dt}$). Since the Magnus force is the unique force exerted by the superfluid, the equality $\mathbf{F}_M = 0$ holds and fix $\mathbf{v}_L = \mathbf{v}_s^*$. The vortices are advected by the surrounding superfluid [74–76]. Additionally, since vortices are the generators of the

velocity field itself, the dynamics of the vortices can be computed only from the knowledge of the vortex positions, indeed, combining the last expressions we get:

$$\mathbf{v}_L^i = \frac{\kappa}{2\pi} \sum_{j \neq i}^{N_v} \frac{n_j \hat{\mathbf{z}} \times (\mathbf{r}_i - \mathbf{r}_j)}{|\mathbf{r}_i - \mathbf{r}_j|^2}. \quad (2.41)$$

This simple equation is known in the literature as the point vortex model (PVM), and is at the basis of many applications ranging from classical to quantum fluid dynamics in large-scale numerical simulation of turbulent systems [21, 77, 78].

2.3.3 Dynamics in a Bose-Einstein condensate

As discussed above, in the repulsive side of the Feshbach resonance, weakly bound pairs forming composite bosons can undergo Bose-Einstein condensation [54]. In the limit $1/k_F a \gg 1$, the macroscopic wavefunction can be effectively described using the Gross-Pitaevskii equation (GPE) [16]:

$$i\hbar \frac{\partial \Psi(\mathbf{r}, t)}{\partial t} = \left(-\frac{\hbar^2}{2M} \nabla^2 + V(\mathbf{r}, t) + g |\Psi(\mathbf{r}, t)|^2 \right) \Psi(\mathbf{r}, t), \quad (2.42)$$

where $M = 2m$ is the mass of the pairs, $V(\mathbf{r}, t)$ is the external potential felt by the fermion pair, and $g = 4\pi\hbar^2 a_M/M$ is the interaction parameter. Here, $a_M = 0.6a$ describes the s-wave scattering length associated to the dimer-dimer process [51]. Although the GPE is an approximation of the many-body wavefunction (neglecting thermal excited states), it captures many aspects of the condensates dynamics such as the dynamics of vortices, solitons, sound propagation, and many other collective behavior.

In particular, from the GPE, we can directly derive the hydrodynamic equations by adopting the Madelung transformation. The conservation momentum can be expressed as:

$$M \frac{\partial \mathbf{v}}{\partial t} = -\frac{M}{2} \nabla |\mathbf{v}|^2 - \nabla V - \frac{1}{n} \nabla p + \nabla \left(\frac{\hbar^2}{2M\sqrt{n}} \nabla^2 \sqrt{n} \right), \quad (2.43)$$

where $p = \frac{\partial E}{\partial V}$ is the pressure. This equation is analogous to the Euler equation from classical fluid dynamics describing an inviscid fluid flow [79, 80]:

$$m \frac{\partial \mathbf{v}}{\partial t} = m \mathbf{v} \times (\nabla \times \mathbf{v}) - \frac{m}{2} \nabla |\mathbf{v}|^2 - \nabla V - \frac{1}{n} \nabla p \quad (2.44)$$

It is important to note that for irrotational flow $\nabla \times \mathbf{v} = 0$. The last term in Eq. (2.43), known as the quantum pressure term, is often negligible for most hydrodynamic applications, as it arises from spatial variations in the wavefunction magnitude on scales comparable to the healing length. However, this term is essential for describing quantum vortices, since vortex cores are on scales of the healing length. It is in this regime that deviations from the Euler equation might become significant. Importantly, this shows that a dilute weakly interacting Bose gas obeys similar equations as a *classical* perfect inviscid fluid.

2.3.4 Two Fluid Model

Since the discovery of superfluidity in liquid helium, the theoretical framework developed by Tisza [60] and Landau [81] has been successful in modeling the observed behavior. From a broad perspective, this model considers two fluids coexisting together: a the normal fluid and superfluid, with the ratio given by the system's temperature. It is crucial to emphasize that while the GPE accurately describes a superfluid composed of a condensate of weakly interacting bosons at $T = 0$, the two-fluid model is a phenomenological framework capturing the thermodynamic and transport properties of any superfluid at finite T . The two-fluid model considers that the superfluid does not carry entropy, instead the normal fluid carrying all the entropy of the system. Then sum of the both normal and superfluid density is equal to total bulk fluid density ($\rho = \rho_s + \rho_n$), and the combined total mass currents is also given by their respective mass currents $\mathbf{j}_{total} = \rho \mathbf{v} = \mathbf{j}_s + \mathbf{j}_n$. The difference between both fluids relies in their dynamical behavior, that is encapsulate the two-fluid model equations[81]:

$$\frac{\partial \rho}{\partial t} + \nabla \cdot (\rho_n \mathbf{v}_n + \rho_s \mathbf{v}_s) = 0, \quad (2.45)$$

$$\frac{\partial}{\partial t} (\rho s) + \nabla \cdot (\rho s \mathbf{v}_n) = 0, \quad (2.46)$$

$$\frac{\partial}{\partial t} (\rho_n \mathbf{v}_n + \rho_s \mathbf{v}_s)_i + \sum_{j=x,y,z} \frac{\partial}{\partial x_j} (P \delta_{ij} + \rho_n \mathbf{v}_{ni} \mathbf{v}_{nj} + \rho_s \mathbf{v}_{si} \mathbf{v}_{sj}) = 0, \quad (2.47)$$

$$m \frac{\partial}{\partial t} \mathbf{v}_s + m (\mathbf{v}_s \nabla) \mathbf{v}_s = -\nabla \mu. \quad (2.48)$$

The first equation describes the mass transport equation using the conservation of mass. The second is the transport of entropy per particle ($s = S/N$) set by the conservation of entropy in reversible processes. The third equation corresponds to the momentum conservation or Navier-Stokes equation, where the viscous term is included in the pressure term, and the last equation setting the motion of the superfluid in terms of the chemical potential μ . The framework of the two-fluid model consists of a phenomenological macroscopic theory based on macroscopic conservation laws such as mass conservation, and the first and second law of thermodynamics. However, theoretical derivations based on the microscopic level support these equations. Further corrections and extensions [82, 83] to this model have been proposed since their first statement in 1941. An important consequence from the two-fluid model is the prediction of several new types of excitations, in particular they predict the presence of two sound modes [84–88].

The coupling between the normal fluid and the superfluid has been subject of many research since the discovery of superfluids. This coupling is not directly evident from the two-fluid model equations, however, they can be made evident by the transport properties of the fluid by sound modes. On the one hand, the symmetric behavior of the mass transport establish the origin for the propagation of (first) sound modes [89], corresponding to density modulations. On the other hand, the asymmetry behavior in entropy transport, enables new ways for temperature transport. This mode, strongly couple the density of both fluids. Indeed, temperature propagation is one of the most illustrative examples that establish the two-fluid model as a way to describe superfluid He. In this model, temperature propagation behaves differently from that of classical fluids alone. Temperature stops being diffusive, and propagates as a wave [84, 90]. This phenomenon, known as second sound propagation, can be interpreted as an exchange between the normal fluid and the superfluid, all while keeping the total density unchanged.

2.4 Dissipative Point vortex model

Another, more subtle and indirect way for coupling both normal and superfluid phases arises from the transport of vortical structures [75, 82]. As discussed previously, the relative velocity of superfluid with respect to the vortex generates a Magnus force.

For rectilinear vortices, where bending is suppressed, this force can be written as:

$$\mathbf{F}_M^i = \kappa \rho_s (\mathbf{v}_s^* - \mathbf{v}_L^i) \times \hat{\kappa}. \quad (2.49)$$

Furthermore, the presence of a secondary fluid, the normal phase, can give origin to additional forces applied to the superfluid vortices. The normal component can react to the moving vortex producing a frictional force which, in general, can be decomposed into components parallel and perpendicular to the relative velocity between the normal component, \mathbf{v}_n^i and the vortex line velocity [75, 91]:

$$\mathbf{F}_N^i = D(\mathbf{v}_n - \mathbf{v}_L^i) + D' \hat{\kappa} \times (\mathbf{v}_n - \mathbf{v}_L^i), \quad (2.50)$$

where D and D' are the corresponding coefficients quantifying their magnitude. Similar to the Magnus force, \mathbf{F}_N^i depends in the average normal component velocity field surrounding the vortex [75]. Moreover, the normal component can fill the inside of the vortex core [75], introducing now a new force, $\frac{\partial \mathcal{P}}{\partial t}$, due to the inertia of the now massive vortex. \mathcal{P} can be generally defined as $\mathcal{P} = \overleftrightarrow{M} \mathbf{v}_L$, where the mass, \overleftrightarrow{M} , can behave as a tensor with components parallel and perpendicular to the vortex velocity [75]. In general, we are going to treat M as a scalar, however, for precision measurements a distinction should be made for fermionic superfluids [75, 91]. Moreover, density inhomogeneities can exert an additional force that might be considered [16, 91] $\mathbf{F}_\rho \propto \nabla \log n$. As such, the balance equation for the vortex dynamics is

$$\mathbf{F}_M + \mathbf{F}_N + \mathbf{F}_\rho = \frac{\partial \mathcal{P}}{\partial t}. \quad (2.51)$$

Writing the force equation in terms of the vortex velocity we get:

$$(\mathbf{v}_s^* - \mathbf{v}_L) \times \hat{\kappa} + d_{||}(\mathbf{v}_n - \mathbf{v}_L) + d_{\perp} \hat{\kappa} \times (\mathbf{v}_n - \mathbf{v}_L) + \mathbf{f}_\rho = \frac{\partial \mathbf{p}}{\partial t} \quad (2.52)$$

where we defined the reduced force coefficients $d_{||} = D/\kappa \rho_s$ and $d_{\perp} = D'/\kappa \rho_s$, $\mathbf{f}_\rho = (\kappa \rho_s)^{-1} \mathbf{F}_\rho$, and $\frac{\partial \mathbf{p}}{\partial t} = (\kappa \rho_s)^{-1} \left(\overleftrightarrow{M} \dot{\mathbf{v}}_L + \dot{\overleftrightarrow{M}} \mathbf{v}_L \right)$. To calculate the vortex dynamics from the balance equation, similar to Eq. (2.41), it is convenient to calculate the cross product between $\hat{\kappa}$ and Eq. (2.52):

$$-(\mathbf{v}_s^* - \mathbf{v}_L) + d_{||}(\mathbf{v}_n - \mathbf{v}_L) \times \hat{\kappa} + d_{\perp}(\mathbf{v}_n - \mathbf{v}_L) + \mathbf{f}_\rho \times \hat{\kappa} = \frac{\partial \mathbf{p}}{\partial t} \times \hat{\kappa}. \quad (2.53)$$

From the linear combination between Eq. (2.53) and Eq. (2.52) weighted by the coefficients $(1 - d_\perp)/(d_\parallel^2 + (1 - d_\perp)^2)$, and $-d_\parallel/(d_\parallel^2 + (1 - d_\perp)^2)$ respectively, one can obtain the equation of motion of the vortex as:

$$\mathbf{v}_L + \alpha \frac{\partial \mathbf{p}}{\partial t} + (1 - \alpha') \hat{\kappa} \times \frac{\partial \mathbf{p}}{\partial t} = \mathbf{v}_s^* + \alpha' (\mathbf{v}_n - \mathbf{v}_s^*) + \alpha \hat{\kappa} \times (\mathbf{v}_n - \mathbf{v}_s^*) - \alpha \mathbf{f}_\rho - (1 - \alpha') \hat{\kappa} \times \mathbf{f}_\rho \quad (2.54)$$

where, for convenience we have introduced the new set of coefficients known as the Hall and Vinen coefficients [75, 76, 92, 93], defined as:

$$\alpha = \frac{d_\parallel}{d_\parallel^2 + (1 - d_\perp)^2}, \quad (2.55)$$

$$1 - \alpha' = \frac{1 - d_\perp}{d_\parallel^2 + (1 - d_\perp)^2}. \quad (2.56)$$

Notice that the dynamics of the vortex depends only on the relative flow between the normal and superfluid components $(\mathbf{v}_n - \mathbf{v}_s^*)$ in the vicinity of the vortex. The equation of motion for the vortex position becomes a first order differential equation whenever the inertia term can be neglected, $\frac{\partial \mathbf{p}}{\partial t} \neq 0$. The inertia term modify the dynamic equation turning it into a second order differential equation, requiring an additional initial condition.

Recent studies [94] suggest that the effect of vortex mass in finite temperature atomic gases can be neglected. However, this effect should be considered when studying binary mixtures, when one component can fill the vortex of the other component, specially for Bose-Bose superfluid mixtures [95]. For the rest of the analysis done in this thesis, we consider $\frac{\partial \mathbf{p}}{\partial t} \approx 0$. Moreover, most of the experiments performed rely on the precise preparation of an initial condition where the system remains static. The average velocity of the normal component is considered to be null, $\mathbf{v}_n = 0$. This assumptions can take us so far in the description of the quantum vortex dynamics, and eventually must be revisited if more knowledge of the behavior of the normal component is achievable.

2.4.1 Mapping to the complex plane

Under the assumptions of no vortex mass, and static background normal component, the equation of motion for the point vortices simplifies:

$$\mathbf{v}_L = (1 - \alpha')\mathbf{v}_s^* - \alpha\hat{\kappa} \times \mathbf{v}_s^*. \quad (2.57)$$

As mentioned in the previous sections, the motion of the vortices is prescribed alone from the position of the vortices, as given by Eq. (2.41):

$$\mathbf{v}_L^i = \frac{\kappa}{2\pi} \hat{z} \times \sum_{j \neq i}^{N_v} n_j \frac{\mathbf{r}_i - \mathbf{r}_j}{|\mathbf{r}_i - \mathbf{r}_j|^2}. \quad (2.58)$$

Equation (2.57) can be solved vectorially, considering the coupled equations for each of the coordinates. However, an easier approach is provided by mapping Eq. (2.57) into the complex plane [96, 97]. The two equations can be written as a function of the complex vortex positions defined as $z_j = x_j + iy_j$. Eq. (2.57) becomes:

$$\frac{d}{dt} \begin{pmatrix} x_i \\ y_i \end{pmatrix} = (1 - \alpha') \begin{pmatrix} v_{x_i}^s \\ v_{y_i}^s \end{pmatrix} - \alpha s(n_i) \begin{pmatrix} -v_{y_i}^s \\ v_{x_i}^s \end{pmatrix} = \begin{pmatrix} 1 - \alpha' & \alpha s(n_i) \\ -\alpha s(n_i) & 1 - \alpha' \end{pmatrix} \begin{pmatrix} v_{x_i}^s \\ v_{y_i}^s \end{pmatrix}, \quad (2.59)$$

where $s(x) = \text{sign}(x)$ is used to account for the cross-product sign with $\hat{\kappa}$. Adopting the expression of \mathbf{v}_s^* in terms of the rest of vortices (Eq. (2.58)), and defining $a_{ij} = a_i - a_j$:

$$\frac{d}{dt} \begin{pmatrix} x_i \\ y_i \end{pmatrix} = \frac{\kappa}{2\pi} \sum_{j \neq i} \frac{n_j}{|r_{ij}|^2} \begin{pmatrix} 1 - \alpha' & \alpha s(n_i) \\ -\alpha s(n_i) & 1 - \alpha' \end{pmatrix} \begin{pmatrix} -y_{ij} \\ x_{ij} \end{pmatrix}, \quad (2.60)$$

$$\frac{d}{dt} \begin{pmatrix} x_i \\ y_i \end{pmatrix} = \frac{\kappa}{2\pi} \sum_{j \neq i} \frac{n_j}{|r_{ij}|^2} \begin{pmatrix} -(1 - \alpha')y_{ij} + \alpha s(n_i)x_{ij} \\ \alpha s(n_i)y_{ij} + (1 - \alpha')x_{ij} \end{pmatrix}. \quad (2.61)$$

Applying the transformation $z = x + iy$, and solving for z_a^* we get:

$$\frac{d(x_a - iy_a)}{dt} = \frac{\kappa}{2\pi} \sum_{b \neq a} n_b \frac{(\alpha s(n_a) - i(1 - \alpha'))(x_{ab} - iy_{ab})}{x_{ab}^2 + y_{ab}^2}, \quad (2.62)$$

Finally:

$$\frac{dz_a^*}{dt} = \frac{(1 - \alpha' + i\alpha s(n_a))\kappa}{2\pi i} \sum_{b \neq a} \frac{n_b}{z_a - z_b}, \quad (2.63)$$

$$\frac{dz_a^*}{dt} = \frac{\kappa_a}{2\pi i} \sum_{b \neq a} \frac{n_b}{z_{ab}}, \quad (2.64)$$

where $\kappa_a = \kappa(1 - \alpha' + i\alpha s(n_a))$. Writing the complex circulation κ_a allows us to recover the functional of the dissipationless point vortex model in complex coordinates. The presence of the complex circulation κ_a , hints at dissipative vortex dynamics. Writing the dissipative point vortex model in this form allows us to compare one-to-one the behavior without dissipation.

2.4.2 Point vortex model in finite systems

Equation (2.64) is valid for infinite size systems, where the only boundary condition on the superfluid velocity is $\mathbf{v}_s \rightarrow 0$ when $|\mathbf{r}| \rightarrow \infty$. However, for finite systems boundary conditions must be taken into consideration. In this thesis, I focus on the following boundary conditions: (i) vortices inside an outer circular boundary, (ii) vortices outside an inner circular boundary, and (iii) vortices in an annular boundary.

In general, the boundary condition is that there is no superfluid outflow from the region of space where it is confined: $(\mathbf{v}_s \cdot \hat{n})|_{\partial\Omega} = 0$, where $\partial\Omega$ traces the path of the boundary, with \hat{n} is the normal vector to the boundary. This boundary condition is chosen due to the steepness of the trapping potential walls present in experimental system. This boundary condition is not necessarily true for harmonically confined gases, where collective trap modes, such as breathing or quadrupole modes, extending far from the cloud's initial radius exist [50]. For circular boundaries, we can easily use the results from the method of images commonly employed in electrostatics [98] to derive the position of *imaginary* vortices.

(i) Vortices inside a circular boundary

Let us first consider the scenario of a circular boundary with radius R , with a single vortex inside the region as shown in Figure 2.4. In this case, adding a single imaginary vortex of opposite circulation at position $\mathbf{r}' = \frac{R^2}{|\mathbf{r}|^2}\mathbf{r}$ satisfy the condition $(\mathbf{v}_s \cdot \hat{n})|_{r=R} = 0$. A full derivation of this result can be found in Ref. [97]. The equation of motion

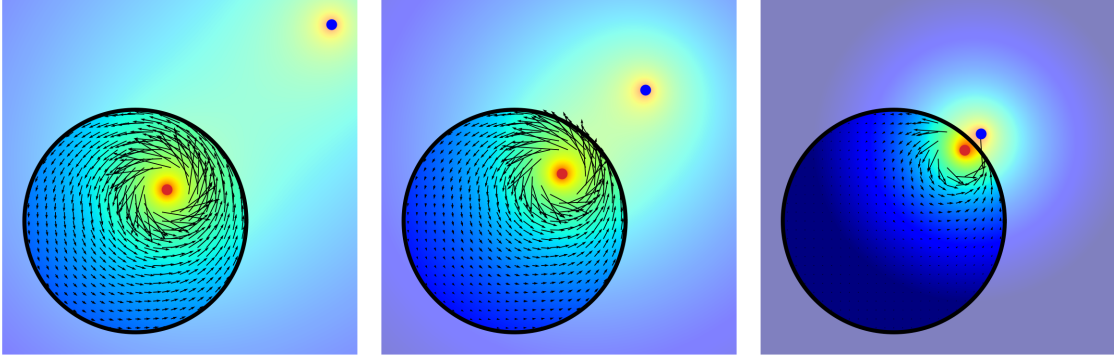


Figure 2.4: Scenarios for different vortex position inside the circular boundary. The superfluid flow is shown by the vector field with the magnitude traced by the background color. Outside the boundary, the imaginary vortex and the general magnitude of the flow created by the pair vortices is shown. Blue and red points show clockwise and anti-clockwise circulation vortices, respectively.

of point vortices under this confinement is:

$$\frac{dz_a^*}{dt} = \frac{\kappa_a}{2\pi i} \left(\sum_{b \neq a}^N \frac{n_b}{z_a - z_b} - \sum_{b=1}^N \frac{n_b}{z_a - \left(\frac{R^2}{|z_b|^2}\right) z_b} \right), \quad (2.65)$$

where the second term runs over all vortices indices accounting for the contribution of each vortex to fulfill the boundary condition.

(ii) Vortices outside a circular boundary

Now, let's consider the scenario of a vortices outside a circular boundary of radius R , with a single vortex out from the excluded region as shown in Figure 2.5. Contrary to the previous scenario, this region of space has a different topology, hence in addition to the hard wall boundary condition, the topological charge enclosed by the boundary must be set. This condition depends on the tangential velocity of the superfluid, and can be interpreted as the enclosure of a multi-quanta vortex located at the origin. Vortices located at the origin trivially fulfill the circular boundary condition $(\mathbf{v}_s \cdot \hat{n})|_{r=R} = 0$. The enclosed quanta of circulation will be denoted by Λ .

Regardless of additional Λ vortices at the origin, for real vortices in the outer region the procedure is similar to the previous case. Adding a single imaginary vortex of

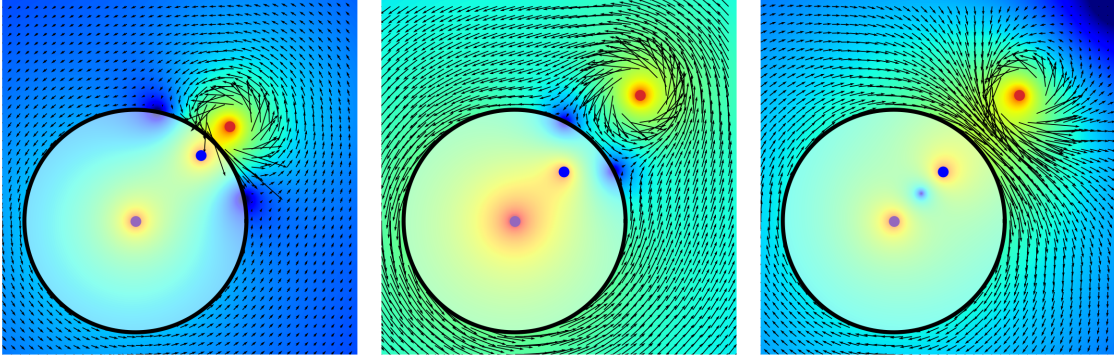


Figure 2.5: Scenarios for different vortex position outside a circular boundary, plotting conventions are the same as for Figure 2.4. Blue and red points show clockwise and anti-clockwise circulation vortices, respectively. The purple vortex at the origin accounts for the topological change enclosed: from left to right:

$$\Lambda = 0, 2, \text{ and } -2.$$

opposite circulation at the position $\mathbf{r}' = \frac{R^2}{|\mathbf{r}|^2} \mathbf{r}$ satisfy $(\mathbf{v}_s \cdot \hat{n})|_{r=R} = 0$. However, since the image vortex is located in the enclosed region, an additional vortex located at the origin with same charge of the real vortex is located in order to keep the total topological charge Λ constant. The equation of motion of point vortices under this confinement is:

$$\frac{dz_a^*}{dt} = \frac{\kappa_a}{2\pi i} \left(\sum_{b \neq a}^N \frac{n_b}{z_a - z_b} - \sum_{b=1}^N \frac{n_b}{z_a - \left(\frac{R^2}{|z_b|^2}\right) z_b} \right) + \frac{\kappa_a}{2\pi i} \frac{\Lambda + \sum_{b=1}^N n_b}{z_a}. \quad (2.66)$$

(iii) Vortices inside an annular region

Finally, let's consider the scenario of a vortices enclosed in an annular region delimited by two concentric circular boundaries with radii $R_i < R_o$. Figure 2.6 shows an example of the method of images applied to a single vortex. Contrary to the previous scenarios, two boundary conditions must be satisfied: $(\mathbf{v}_s \cdot \hat{n})|_{r=R_i} = 0$ and $(\mathbf{v}_s \cdot \hat{n})|_{r=R_o} = 0$ in addition to the degree of freedom of the topological change Λ enclosed by the inner boundary. To satisfy both boundary conditions simultaneously an infinite number of vortices is required [99]. The procedure to calculate the positions of each vortex has been worked out in Ref [97]. The construction procedure is as follows:

1. Satisfy the outer boundary condition adding the image vortex at $\mathbf{r}'_{o1} = \frac{R_o^2}{|\mathbf{r}|^2} \mathbf{r}$.

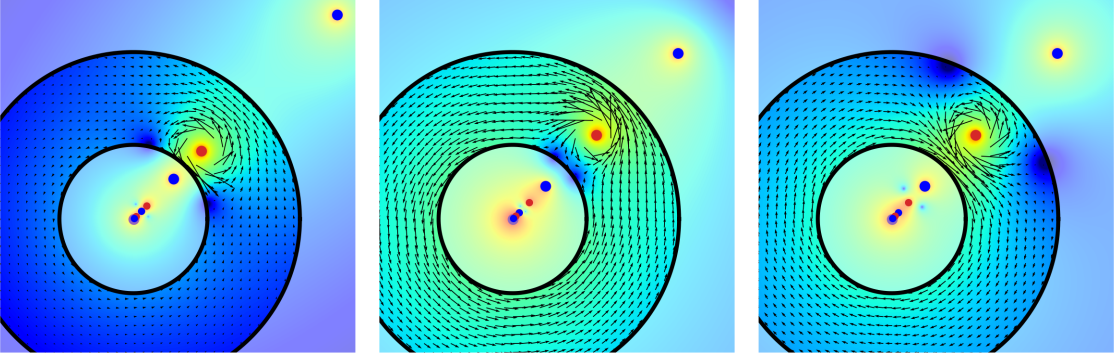


Figure 2.6: Scenarios for different vortex position inside an annular region, plotting conventions are the same as the previous figures. Similar to scenario (ii), The enclosed topological from left to right are: $\Lambda = 0, 2,$ and -2 .

2. Satisfy the inner boundary condition adding the image vortex of both vortices at \mathbf{r} and \mathbf{r}'_{o1} . This shall create 3 new imaginary vortices at positions $\mathbf{r}' = 0$, $\mathbf{r}'_{i1} = \frac{R_i^2}{|\mathbf{r}|^2} \mathbf{r}$, and $\mathbf{r}'_{i2} = \frac{R_i^2}{|\mathbf{r}'_{o1}|^2} \mathbf{r}'_{o1} = \frac{R_i^2 R_o^2}{R_o^2 |\mathbf{r}|^2} \mathbf{r}$.
3. Satisfy the outer boundary condition adding the corresponding image vortices at positions: $\mathbf{r}'_{o2} = \frac{R_o^2}{|\mathbf{r}'_{i1}|^2} \mathbf{r}'_{i1} = \frac{R_o^2 R_i^2}{R_i^2 |\mathbf{r}|^2} \mathbf{r}$, and $\mathbf{r}'_{o3} = \frac{R_o^2}{|\mathbf{r}'_{i2}|^2} \mathbf{r}'_{i2}$.
4. Repeat indefinitely.

The recursive process can be summarized in the following equation of motion of point vortices under this confinement is:

$$\begin{aligned} \frac{dz_a^*}{dt} = & \frac{\kappa_a}{2\pi i} \frac{\Lambda + \sum_{b=1}^N n_b}{z_a} + \frac{\kappa_a}{2\pi i} \left[\sum_{b \neq a}^N \frac{n_b}{z_a - z_b} - \sum_{b=1}^N \left(\frac{n_b}{z_a - \left(\frac{R_i^2}{|z_b|^2} \right) z_b} + \frac{n_b}{z_a - \left(\frac{R_o^2}{|z_b|^2} \right) z_b} \right) \right] \\ & + \frac{\kappa_a}{2\pi i} \left[\sum_{b=1}^N \sum_{n=1}^{\infty} \left(\frac{n_b}{z_a - \left(\frac{R_i}{R_o} \right)^{2n} z_b} + \frac{n_b}{z_a - \left(\frac{R_o}{R_i} \right)^{2n} z_b} \right) \right. \\ & \left. - \sum_{b=1}^N \sum_{n=1}^{\infty} \left(\frac{n_b}{z_a - \left(\frac{R_i}{R_o} \right)^{2n} \left(\frac{R_i^2}{|z_b|^2} \right) z_b} + \frac{n_b}{z_a - \left(\frac{R_o}{R_i} \right)^{2n} \left(\frac{R_o^2}{|z_b|^2} \right) z_b} \right) \right] \end{aligned}$$

Notice the first four terms, correspond to the direct contribution of the imaginary vortices presented in the (i) and (ii) scenarios. The last two terms correspond to the

recursion process described above. It is important to note that the infinite sequence converges fairly quickly, and allowing the numerical simulations to be accurate using few terms the summation. For the simulations we consider 11 vortex images.

Chapter 3

Kelvin-Helmholtz instability: from classical fluids to point vortex models

3.1 Classical Kelvin-Helmholtz instability

One of the most well known instabilities in fluid mechanics is the instability at the interface between two parallel streams having different velocities and densities (with the heavier fluid at the bottom). This instability is known as the Kelvin–Helmholtz instability, and was first described in the 19th century by Lord Kelvin and H. von Helmholtz when modeling the formation of ocean wind waves [100]. Their work laid the foundation for understanding various fluid dynamics scenarios, from atmospheric phenomena to astrophysical processes [20, 101–103], highlighting the significance of this instability in both theoretical and applied contexts.

3.1.1 Kelvin-Helmholtz model

The simplest flow demonstrating the Kelvin–Helmholtz instability is that of two unbounded two dimensional fluids [79, 80] with uniform velocities v_1 for $y < 0$, and v_2 for $y > 0$, see Figure 3.1. The interface defined as the site where the velocity jump, is assumed to have no thickness. In general, the fluids can have different densities ρ_1 and ρ_2 , and have a surface tension σ between them, however, it is not a requirement. Nonetheless, for the this thesis I exclude the scenario with surface tension.

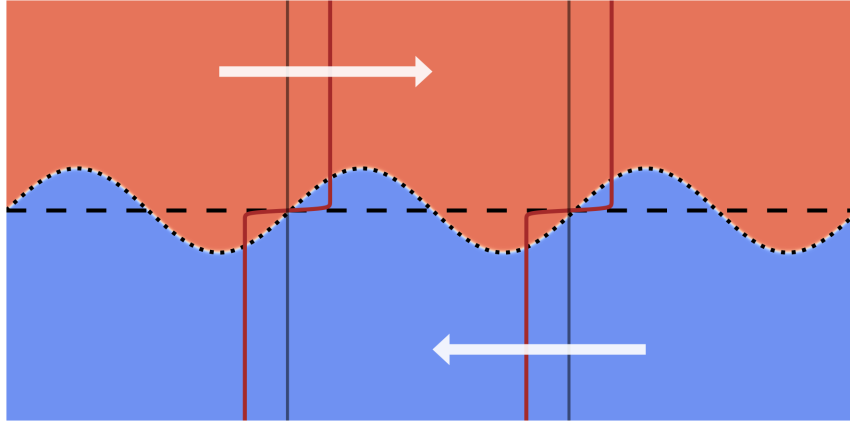


Figure 3.1: Initial perturbed state in a shear-flow configuration: the Kelvin–Helmholtz instability.

In two dimensional incompressible and irrotational fluids the velocity field can generally be described either using a stream function Ψ ($v = \nabla \times \Psi$), or using a potential function ϕ , where $v = \nabla \phi$ [79, 80]. We'll use the latter to describe both the lower, ϕ_1 , and the upper ϕ_2 , fluids. The irrotational condition for the velocity directly translate to a Laplace equation for the potential $\nabla \times v_i = \nabla^2 \phi_i = 0$, where the boundary conditions are set by:

$$\frac{\partial \phi_1}{\partial x} = v_1, \quad \frac{\partial \phi_1}{\partial y} = 0 \text{ as } y \rightarrow -\infty, \quad (3.1)$$

$$\frac{\partial \phi_2}{\partial x} = v_2, \quad \frac{\partial \phi_2}{\partial y} = 0 \text{ as } y \rightarrow \infty. \quad (3.2)$$

A perturbation occurring at the interface will deform it. Let us describe the resulting curve by the relation $y = \eta(x, t)$, or equivalently $f(x, y, t) = y - \eta(x, t) = 0$. If the interface moves with a velocity V , the transport equation of the interface can be written as [79]:

$$\frac{Df}{Dt} = \frac{\partial f}{\partial t} + V \cdot \nabla f = 0 \quad (3.3)$$

where $\frac{D}{Dt}$ is also known as the material derivative [80]. The kinematic boundary condition, which states that the interface moves up and down with a velocity equal to the vertical component of the fluid velocity can be written as [79]:

$$\frac{\partial \eta}{\partial t} + V \frac{\partial \eta}{\partial x} = v_\eta \quad \text{at } y = \eta(x, t), \quad (3.4)$$

where v_η is the vertical component of velocity of the interface. Combining the Bernoulli equation for potential flows [79]: $\frac{\partial \phi}{\partial t} + \frac{1}{2}(\nabla \phi)^2 + P/\rho + gy = C(t)$, in each fluid and considering the fluids just below (described by ϕ_1) and just above (described by ϕ_2) the interface, we arrive to the following equilibrium condition at the interface [79]:

$$\rho_1 \left(\frac{\partial \phi_1}{\partial t} + \frac{1}{2}(\nabla \phi_1)^2 - C_1 \right) = \rho_2 \left(\frac{\partial \phi_2}{\partial t} + \frac{1}{2}(\nabla \phi_2)^2 - C_2 \right), \quad (3.5)$$

where we considered the equal pressure of the fluids across the interface. In this case, the stationary solution for the flows fixing a static interface, i.e. $\eta(x, t) = 0$ is simply given by $\phi_1 = v_1 x$, and $\phi_2 = v_2 x$.

So, by perturbing the interface with a traveling wave $\eta(x, t) = \hat{\eta} e^{i(kx - \omega t)}$, and performing a linear stability analysis for the perturbed flows $\phi'_i = \phi_i - v_i x = \hat{\phi}_i(y) e^{i(kx - \omega t)}$, we arrive to the following solutions [79]:

$$\eta(x, t) = \hat{\eta} e^{i(kx - \omega t)}, \quad \phi'_1 = \hat{\phi}_1 e^{ky} e^{i(kx - \omega t)}, \quad \phi'_2 = \hat{\phi}_2 e^{-ky} e^{i(kx - \omega t)}. \quad (3.6)$$

After substitution in Eq. (3.5), we obtain the instability dispersion relation [79]:

$$\omega = \omega_r + i\sigma = \frac{\rho_1 v_1 + \rho_2 v_2}{\rho_1 + \rho_2} k \pm \sqrt{\frac{\rho_1 - \rho_2}{\rho_1 + \rho_2} g k - \rho_1 \rho_2 \left(\frac{v_1 - v_2}{\rho_1 + \rho_2} \right)^2 k^2}. \quad (3.7)$$

In particular, the interface can become unstable and grow exponentially in time when $\sigma > 0$. Assuming equally dense fluids $\rho_1 = \rho_2 = \rho$, we find the system to be always unstable regardless of the wavenumber k since the first term inside the square root vanishes. The instability grow rate becomes:

$$\sigma = \frac{1}{2} \Delta v k, \quad (3.8)$$

where $\Delta v = |v_1 - v_2|$.

Beyond the initial growth of the interface extent η , the interface deforms dramatically as shown from numerical simulations of the fluid equation in Figure 3.2. This deformations arise in the non-linear regime [79], and cannot longer be described

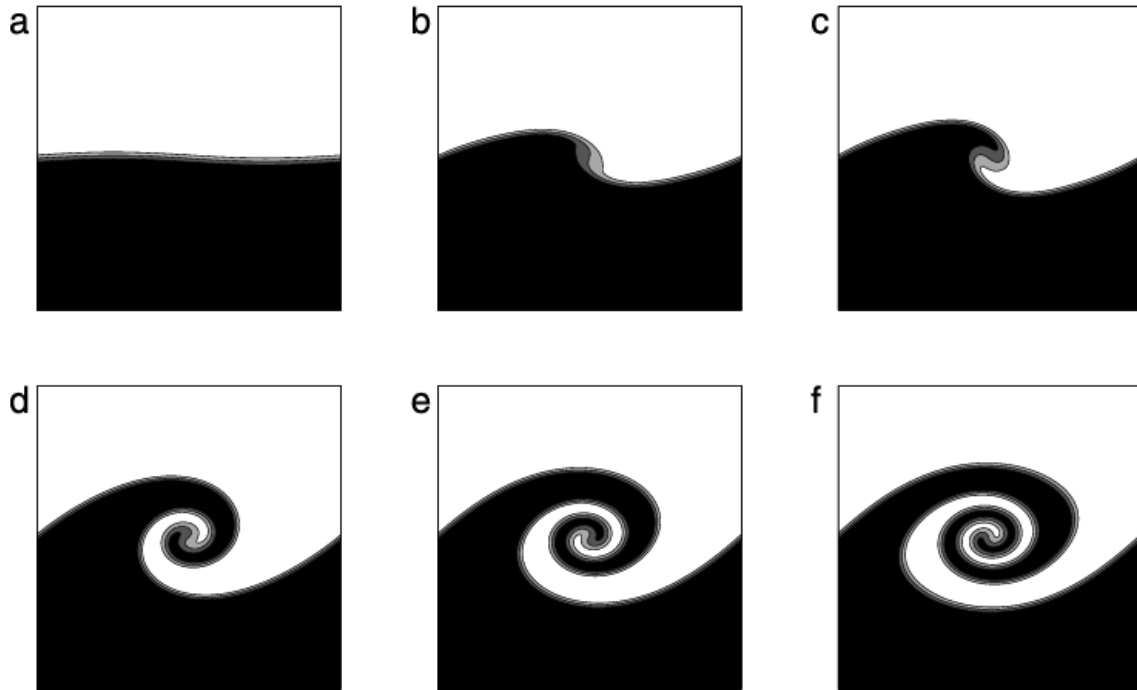


Figure 3.2: Interface temporal evolution under the Kelvin–Helmholtz instability.
Image taken from [104].

as a simple traveling wave. However, more advanced techniques can be used to study the observed roll-up dynamics, such as the integro-differential equation known as the Birkhoff-Rott equation [105].

3.1.2 Rayleigh model

In common fluids, due to viscous effects, a sharp velocity discontinuity, such as in Figure 3.1 cannot be sustained [100]. A more accurate model for the total flow requires that the shear layer continuously and smoothly connects both regions of uniform flow. Rayleigh in 1880 provided an analytical solution for this through a simple piecewise-linear profile [106]. Where the velocity profile is defined as:

$$v = v_1, \quad \text{if } y < -\delta, \quad (3.9)$$

$$v = \frac{v_1 + v_2}{2} + \left(\frac{v_2 - v_1}{2} \right) \frac{y}{\delta}, \quad \text{if } -\delta < y < \delta, \quad (3.10)$$

$$v = v_2, \quad \text{if } y > \delta. \quad (3.11)$$

An even better model of the total flow, which is more regular than the piecewise-linear flow, is that of a hyperbolic tangent flow: $v = v_0 + \Delta v \tanh(y/\delta)$, shown in Figure 3.3. Using the hyperbolic tangent velocity flow the stability conditions cannot be obtained analytically. However, numerical solving them leads to a stability curve very close to that of the piecewise-linear profile, which can be obtained analytically [79, 106].

For simplicity, let us consider the case of equal densities above and below the interface. To approach this problem it is convenient to return to the description of the velocity field through the stream function $v = \nabla \times \Psi$. As for the potential function ϕ , the stream function also solve the Laplace equation $\nabla^2 \Psi = 0$.

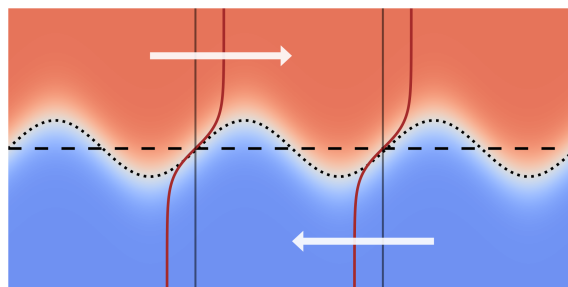


Figure 3.3: Initial perturbed state in a smoothly varying velocity profile shear-flow configuration: Rayleigh version of describing the Kelvin–Helmholtz instability.

Following a similar approach as before, the boundary conditions for both lower and upper stream functions are given by [79]:

$$\frac{\partial \Psi_1}{\partial x} = 0, \quad \frac{\partial \Psi_1}{\partial y} = v_1 \text{ as } y \rightarrow -\infty, \quad (3.12)$$

$$\frac{\partial \Psi_2}{\partial x} = 0, \quad \frac{\partial \Psi_2}{\partial y} = v_2 \text{ as } y \rightarrow \infty. \quad (3.13)$$

Near the interface located at the modulated interface at $y = \eta(x, t)$, we can consider the description of the fluids just below and just above the interface, and arrive to the interface transport equation:

$$\frac{\partial \eta}{\partial t} = v_1 \frac{\partial \eta}{\partial x} + \frac{\partial \Psi_1}{\partial x} = v_2 \frac{\partial \eta}{\partial x} + \frac{\partial \Psi_2}{\partial x} \quad (3.14)$$

By considering traveling decaying perturbation modes of the form:

$$\eta(x, t) = \hat{\eta} e^{i(kx - \omega t)}, \quad (3.15)$$

$$\Psi'_1 = \hat{\Psi}_1 e^{ky} e^{i(kx - \omega t)}, \quad \text{if } y < -\delta, \quad (3.16)$$

$$\Psi'_0 = (\hat{\Psi}_0 e^{ky} + \tilde{\Psi}_0 e^{-ky}) e^{i(kx - \omega t)}, \quad \text{if } -\delta < y < \delta, \quad (3.17)$$

$$\Psi'_2 = \hat{\Psi}_2 e^{-ky} e^{i(kx - \omega t)}, \quad \text{if } y > \delta, \quad (3.18)$$

and substituting them into the interface transport equation we obtain the Rayleigh formula for their dispersion relation [79]:

$$\omega = \omega_r + i\sigma = \frac{v_1 + v_2}{2} k \pm \left(\frac{\Delta v}{4\delta} \right) \sqrt{(2k\delta - 1)^2 - e^{-4k\delta}}. \quad (3.19)$$

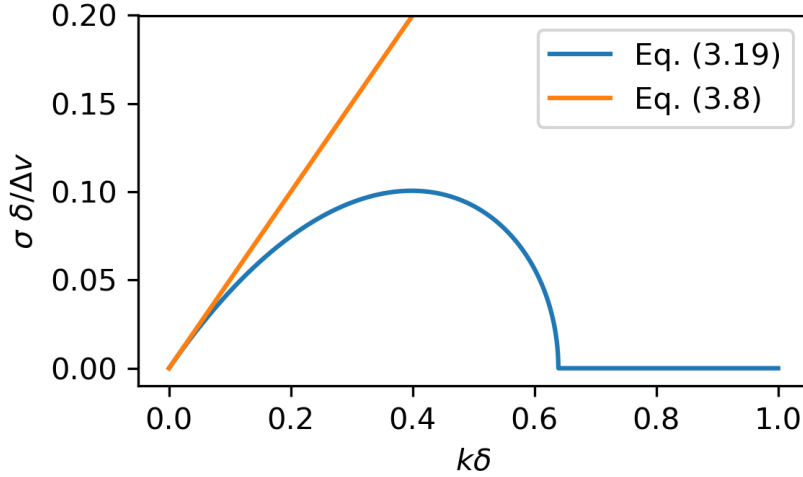


Figure 3.4: Comparison between the rate initially calculated by Kelvin and Helmholtz given by Eq. 3.20, and the one for a smooth interface given by Eq. 3.19.

In the limit $\delta \rightarrow 0$, we recover the relation we get from Eq (3.7) for equal densities:

$$\omega \rightarrow \frac{v_1 + v_2}{2} k \pm i \frac{v_1 - v_2}{2} k. \quad (3.20)$$

The behavior of the growth rate between sharp and smooth velocity transitions are strikingly different, as shown in Figure 3.4. For large wavelength perturbations, $k\delta \rightarrow 0$, we recover the limit of the sharp interface model initially proposed by Kelvin and Helmholtz given by Eq. (3.8). However, for perturbation wavelengths in the

order of the interface width, $k\delta \geq k_c\delta \approx 0.6392$, the instability is suppressed, and the perturbation is neither amplified nor attenuated. The maximum growth rate occurs for $k^*\delta \sim 0.398$ with a maximum value of $\sigma \sim 0.1006\Delta v/\delta$.

3.2 From the continuum to the discrete: Helmholtz's results

In classical hydrodynamics, incompressible fluid flow can be described in two main ways: based on the velocity and pressure, or in terms of the velocity and vorticity [80]. The velocity-vorticity description has advantages when there are no boundaries, because vorticity inside a fluid cannot be created or destroyed, as prescribed by Helmholtz theorem [80]. The vorticity field also connects directly to physical flow structures, like line or ring vortices. For instance the vorticity in fluid dynamics can be written as:

$$\frac{D\vec{\omega}}{Dt} = \frac{\partial\vec{\omega}}{\partial t} + (\mathbf{v} \cdot \nabla)\vec{\omega} = (\vec{\omega} \cdot \nabla)\mathbf{v} + \nu\nabla^2\vec{\omega}, \quad (3.21)$$

where $\vec{\omega} = \nabla \times \mathbf{v}$ is the vorticity of the velocity flow \mathbf{v} .

In two dimensions, the vorticity field has an extra benefit: it reduces to a scalar: $\vec{\omega} = \omega\hat{z}$. An alternative representation of two-dimensional flows in terms of moving point vortices was developed by Kirchhoff [107] and Von Helmholtz [108] in the mid 1800's. While the Helmholtz–Kirchhoff point vortex model captures many physical phenomena observed in two-dimensional rotational flows in classical fluids, experiments with simple vortex configurations exhibit complications beyond the point vortex predictions. Extensions of the model include viscous corrections and finite vortex core sizes [109].

Despite the deviations observed in viscous fluids, this description is suitable for describing superfluids since no viscous effects should be neglectable [76]. Finite vortex core effects can be indeed be addressed even for superfluids improving the available models [76], however, when considering low vortex density systems[73], the direct representation introduced by Kirchhoff and Helmholtz should be applicable. Following this line of thought, let us consider the Kelvin-Helmholtz instability from the perspective of point vortices.

The problem stated above, of two different fluids having different velocities across

a sharp interface, can be mapped to point vortices in the follow way. At the interface, where there is a jump in the tangential velocity, the vorticity of the fluid is given by $\omega = \frac{\partial v_x}{\partial y} = \omega_0 \delta(y)$, where ω_0 is the vorticity per unit length, and $\delta(y)$ corresponding to the Dirac delta. The continuous line of constant vorticity must then be split into multiple point vortices, each caring the same circulation κ , and which must be equally separated a distance d_v following the line of constant vorticity. For this scenario, the value of κ , and d_v are linked to the relation [96] $\Delta v = \frac{\kappa}{d_v}$. The problem of the unstable continuous interface, can therefore be mapped to the problem of the stability of a linear array of equidistant point vortices.

3.3 Instability of point vortex arrays

3.3.1 Instability of a row vortex array



Figure 3.5: Temporal evolution of the Kelvin–Helmholtz instability from point vortices. Image compiled from simulations performed in [110].

The problem of a row of vortices has been approached in various ways over the years [96]. On one hand, we may think of a row of vortices as a discretization version of a continuous vortex sheet, such as many numerical approached to study of vortex sheet roll-up [96], as seen in Figure 3.5. Considering the continuum limit, we should recover from the stability problem for the vortex row the dispersion relation for the

inviscid Kelvin-Helmholtz instability for equal densities we derived in section 3.1.1, namely $\sigma = \frac{1}{2}k\Delta v$.

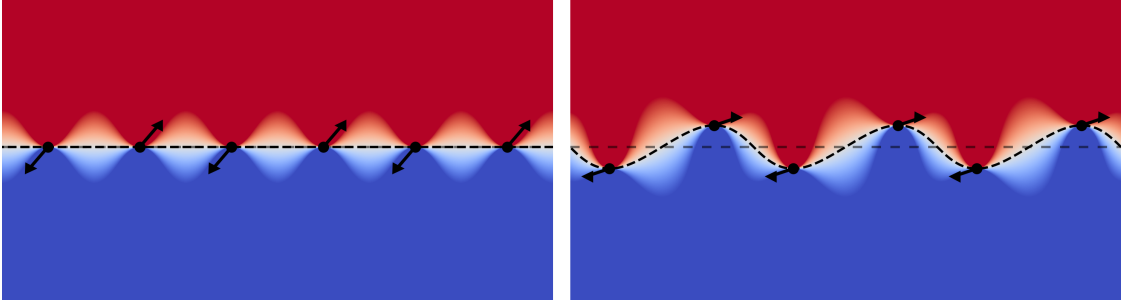


Figure 3.6: Ideal (left) and initial perturbed (right) states in a superfluid shear-flow configuration. Perspective of the the Kelvin–Helmholtz instability in superfluids.

To start the analysis of the vortex motion, let us recover the point model from Eq. (2.41), where for classical fluids the circulation κ_j can take arbitrary values.

$$\mathbf{v}^i = \frac{1}{2\pi} \sum_{j \neq i}^{N_v} \frac{\kappa_j \hat{z} \times (\mathbf{r}_i - \mathbf{r}_j)}{|\mathbf{r}_i - \mathbf{r}_j|^2}. \quad (3.22)$$

Fixing the linear array of vortices equispaced a distance d_v along the x-axis, we can write their locations as $(x_j, y_j) = (jd_v, 0)$, and by mapping the problem to the complex plane $z_a = ad_v$. Moreover, Let's consider the scenario where all vortices have the same arbitrary circulation κ around them. The equation of motion for the a-th vortex is given by:

$$\frac{dz_a^*}{dt} = \frac{\kappa}{2\pi i} \sum_{b \neq a}^N \frac{1}{z_a - z_b} = \frac{\kappa}{2\pi d_v i} \sum_{b=-\infty, \neq a}^{\infty} \frac{1}{a - b} = 0. \quad (3.23)$$

which vanishes due to symmetry arguments: the contribution of the vortices on the left cancel exactly those of the right side of each vortex. The solution, $z_a = ad_v$, is therefore a stationary equilibrium state, as it is the case of a planar interface for continuous classical fluids. Let us now perturb the system, so the positions of the vortices become $z_a = ad_v + \eta_a$. Here, the linear approximation of the equation of motion for the perturbation on the a-th vortex is:

$$\frac{d\eta_a^*}{dt} = \frac{\kappa i}{2\pi d_v^2} \sum_{b=-\infty, \neq a}^{\infty} \frac{\eta_a - \eta_b}{(a - b)^2}. \quad (3.24)$$

Considering a periodic perturbation of the form $\eta_a = \hat{\eta}(t)e^{iakd_v}$, where the wavenumber k may be chosen to satisfy $|k|d_v < \pi$, we get:

$$\frac{d\hat{\eta}^*}{dt}e^{-iakd_v} = \frac{\kappa i}{2\pi d_v^2} \sum_{b=-\infty, \neq a}^{\infty} \frac{e^{iakd_v} - e^{ibkd_v}}{(a-b)^2} = \frac{\kappa i}{2\pi d_v^2} e^{iakd_v} \sum_{b=-\infty, \neq a}^{\infty} \frac{1 - e^{i(b-a)kd_v}}{(b-b)^2}. \quad (3.25)$$

which can be further simplified by noting that the sum term does not depend on the index a, and can be rewritten as [96]:

$$\sum_{b=-\infty, \neq a}^{\infty} \frac{1 - e^{i(b-a)kd_v}}{(b-b)^2} = 2 \sum_{\beta=1}^{\infty} \frac{1 - \cos(kd_v\beta)}{\beta^2} = \pi |k|d_v \left(1 - \frac{|k|d_v}{2\pi}\right) = A_{|k|}. \quad (3.26)$$

Reducing to:

$$\frac{d\hat{\eta}^*}{dt}e^{-iakd_v} = \frac{\kappa i}{2\pi d_v^2} A_{|k|} \hat{\eta} e^{iakd_v} \quad (3.27)$$

Now, let us consider the superposition of two traveling waves, having the same wavenumber k , as $\eta_a = \hat{\eta}(t)(e^{iakd_v} + e^{-iakd_v})$. After substitution in the previous relation we obtain:

$$\frac{d\hat{\eta}^*}{dt} = \frac{\kappa i}{2\pi d_v^2} A_{|k|} \hat{\eta}, \quad (3.28)$$

which can be easily solved by considering the second temporal derivative:

$$\frac{d^2\hat{\eta}}{dt^2} = - \left(\frac{\kappa A_{|k|}}{2\pi d_v^2}\right)^2 \hat{\eta} \rightarrow \hat{\eta} = e^{\frac{\kappa A_{|k|}}{2\pi d_v^2} t} \hat{\eta}_0, \quad (3.29)$$

resulting in the dispersion relation for the vortex row:

$$\omega = \omega_r + i\sigma = i \frac{\kappa A_{|k|}}{2\pi d_v^2} = i \frac{\kappa |k|}{2d_v} \left(1 - \frac{|k|d_v}{2\pi}\right). \quad (3.30)$$

Similarly to Rayleigh's model, the growth rate of the instability has a maximum, whenever $k^* = \frac{\pi}{d_v}$, yielding the maximum instability growth rate:

$$\sigma_{max} = \frac{\kappa |k|}{4d_v} = \frac{\kappa \pi}{4d_v^2}. \quad (3.31)$$

3.3.2 Thickness of the interface layer

An interesting fact regarding the velocity field generated by the row of vortices is the smooth profile generated far for the positions of the vortices, as seen in Figure 3.7. In fact, the tangential velocity profile can be analytically obtained and is given by [49, 72]:

$$v_x(x, y) = \frac{\kappa}{2d_v} \frac{\sinh(2\pi y/d_v)}{\cosh(2\pi y/d_v) + \cos(2\pi x/d_v)}. \quad (3.32)$$

From this result, we can see that the velocity profile near the interface at $y = 0$ can be approximated by a hyperbolic tangent function $v_x = v_0 \tanh\left(\frac{y}{\delta(x)}\right)$, where the width $\delta(x)$ is position dependent, as shown in Figure 3.7 c.

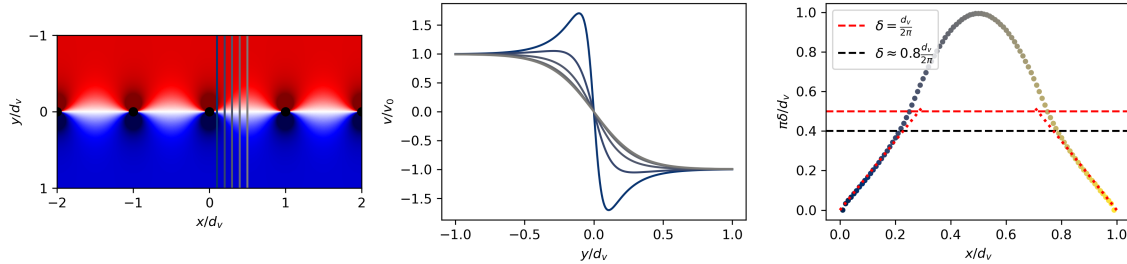


Figure 3.7: a) Tangential velocity profile generated by a row of vortices. b) Tangential velocity as a function of the distance between vortices, color denote the horizontal position in panel a. c) Width of a hyperbolic tangent fit as a function of the z-axis.

From a coarse-grained perspective, we can treat the varying widths of the tangential profiles as a single, average value. In particular, the average width can be neatly expressed as:

$$\delta = \frac{d_v}{2\pi}, \quad (3.33)$$

as it is also anticipated by Eq. (3.32). Moreover, in the limit $y/d_v \rightarrow \infty$, we recover the scenario of infinitely close vortices, where κ and d_v are no longer proper quantities, with rather $\Delta v = \kappa/d_v$ defining properly the mapping to the continuous fluids. As such, in this limit, the growth rate obtained from Eq. (3.30) is $\sigma = \frac{\kappa}{2d_v} k = \frac{1}{2} k \Delta v$, the same results as obtained by Kelvin and Helmholtz.

As shown in Figure 3.8, the behavior of the point vortex model and Rayleigh's formula follow the same trend. However, they show different maxima growth rate at different values of $k\delta$. The discrepancy between both models could be due to the coarse-grained procedure, which could be corrected on the mapping of the average

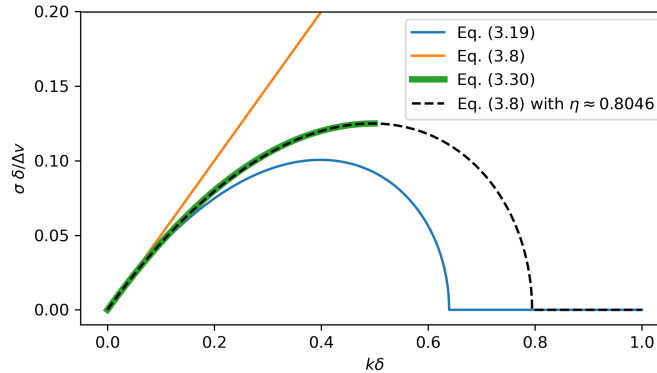


Figure 3.8: Comparison between the growth rate of all models. Orange: Sharp interface, blue: Rayleigh smooth interface, green: point vortex model, black dashed: smooth interface matching width to correspond to the point vortex model most unstable wavenumber.

interface width choosing $\tilde{\delta} \equiv \eta\delta$, where η is a constant of order 1. To get the value of η , we fix the most unstable wavenumbers between both models to be same, namely $k^*\delta = \frac{\pi}{d_v} \frac{d_v}{2\pi} = \frac{1}{2}$ for the point vortex approach, and $k^*\delta \sim 0.6392$. The relative factor between both give us $\eta \approx 0.80465$. More formally, this number can be obtained from solving the equation $\left(\sqrt{e^{-2\eta} - (\eta - 1)^2}\right) / \eta = \frac{1}{2}$. It is worth considering the comparison between the local widths $\delta(x)$, and the coarse grained values $\delta = \frac{d_v}{2\pi}$ and $\tilde{\delta} = 0.8 \frac{d_v}{2\pi}$ shown in Fig. 3.7c. Starting from the vortex positions ($x = 0, x = 1$), $\delta(x)$ increases linearly until reaching $\tilde{\delta}$, after which a sudden rise changes the curvature of $\delta(x)$. The change in behavior may act as a stricter condition for the coarse-grained effective width, rather than relying solely on the simple average width.

Evaluating Rayleigh's formula (Eq. (3.19)) using this correction, we obtain the black dashed curve in Figure 3.8, matching perfectly the behavior of the point vortex model up to the maximum valid wavenumber, $|k^*| = \frac{\pi}{d_v}$. The unexpected overlap between the models, when applying the correction factor, highlights the intriguing link between the instability of a vortex array and that of a classical fluid with a smooth velocity profile at the interface.

3.4 Kelvin-Helmholtz instability in superfluids

Theoretical investigations of the Kelvin-Helmholtz instability in quantum fluids have been mostly focused on the stability of the interface between distinct sliding fluid

components in Helium systems, concentrating in the interfaces formed by the superfluid and normal phases [111–113], or between two different superfluids phases such as the A and B phases of He3 [45]. Additionally, the Kelvin-Helmholtz instability has been studied for the free surface of a liquid including both superfluid and normal components [113]. Experimental observations in liquid Helium remain limited to the interface between the A and B phases of ^3He in a rotating cryostat [45, 114], where they measured the onset of the instability as a function of the rotation speed of the containers, rather than probing the imaginary part of the dispersion relation.

More recently, the Kelvin-Helmholtz instability has been studied in the context of binary mixtures of Bose-Einstein condensates [115–118] in different inter species interaction regimes, from immiscibility to miscible mixtures. For immiscible mixtures, the Kelvin-Helmholtz instability appears as the modulation of the interface between both superfluids, in complete analogy to classical fluids. In the non linear regime, instead of rolling up the interface, depending on the system parameters, additional effects can occur, such as the expulsion of islands of one condensate into the other, forming the so called skyrmion structures [115], which was verified experimentally by [119]. Similarly to classical fluids, the Kelvin-Helmholtz instabilities [120] in binary BECs has been linked as a precursor to turbulent behavior.

Recently, a theoretical proposal by A. Baggaley [121], showed that the Kelvin-Helmholtz instability can be observed in a single-component atomic superfluid by solving the GPE. Later, [122] showed that similar dynamics could be observed in single-component superfluids in the transition from small velocities to close to supersonic velocities at the interface by directly solving the Bogoliubov equations. Both of these results are key for the observation of shear flow dynamics in a single-component atomic superfluid. When a shear flow appears in a superfluid, the density and velocity of the superfluid must adjust accordingly. Contrary to binary mixtures [115–118], the lines of non-zero vorticity are unstable and decay into arrays of vortices. The latter being a consequence of the irrotationality of single superfluids and the quantization of the circulation. Therefore, the velocity interface between both fluid layers of a same-species superfluid is no longer smooth but rather present modulations due to the presence of the single quantum vortices. Thus, the description of the Kelvin-Helmholtz instability in a single-component atomic superfluid is well encapsulated by the instability of point vortices in the Helmholtz–Kirchhoff point vortex model.

Chapter 4

From persistent currents to vortex arrays in superfluids

In this chapter, I describe the protocol used in our experiments to produce a fermionic superfluid flowing in a ring-shaped trap with quantized circulation.

Firstly, I briefly discuss the experimental sequence used for cooling down the atomic gas and for the creation of fermionic superfluids across the BEC-BCS crossover. Secondly, I present how through the combination of a high-resolution objective and a Digital Micromirror Device (DMD) we are able to generate on-demand static and dynamical optical potentials, allowing us to precisely manipulate the potential landscape of the atoms. Next, I describe the procedure employed to excite persistent currents in ring-shaped superfluids. Moreover, their stability and robustness are discussed.

Finally, I present the creation of the prototypical scenario required for the observation of the Kelvin-Helmholtz Instability (KHI) in superfluids: two concentric ring-shaped superfluids in counter-rotating motion. By dynamically controlling their overlap through the separating optical barrier we generate the initial configuration for the observation of the KHI from the vortex array instabilities perspective.

4.1 Preparation of a superfluid gas ${}^6\text{Li}$

4.1.1 Ultra-high vacuum system

Cold atoms experiments need to be performed under vacuum. Our setup, illustrated in Figure 4.1, consists of four main sections: the oven, the differential pumping, the Zeeman slower, and the science chamber. Inside the oven, an artificially enriched ${}^6\text{Li}$ sample is heated to 400°C , generating sufficient vapor pressure to form an atomic beam, which is then collimated by the combination of a nozzle at the exit of the oven and a copper cold finger. Subsequently, the atomic beam passes through a differential pumping stage that enables the decoupling between the *high* pressure from the oven (10^{-10} - 10^{-8} Torr) and the science chamber (10^{-11} Torr). Next, the atomic beam then enters the Zeeman slower, where the atoms are decelerated to approximately 60 m/s. Finally, the slowed atoms enter the science chamber, where they are captured in a 3D magneto-optical trap (MOT). The science chamber is an octagonal stainless-steel cell, featuring two large re-entrant viewports along its vertical axis to accommodate a high-resolution imaging system. A detailed description of the ultra-high vacuum system is provided in Ref [123].

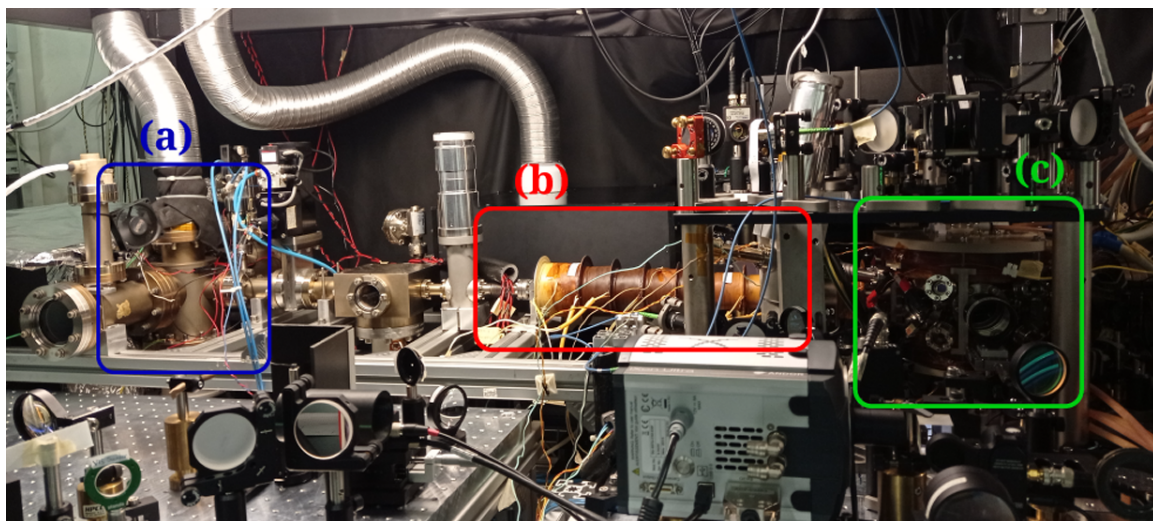


Figure 4.1: Experimental vacuum system used for the production of ultracold fermionic gases. A metallic lithium sample is placed in the oven (a), where it is heated to 400°C , generating sufficient vapor pressure to produce an atomic beam expelled through a nozzle. The atomic beam is subsequently decelerated using a Zeeman slower (b) before being captured and trapped in the science chamber (c). Image from [124].

4.1.2 Lithium in the presence of magnetic fields

The fermionic isotope of lithium has in its ground state, $2^2S_{1/2}$, a single valence electron with total angular momentum $\hat{J} = \hat{L} + \hat{S} = 0 + 1/2 = 1/2$. The first two excited states corresponds to the $2^2P_{1/2}$ and $2^2P_{3/2}$ states, with $\hat{J} = 1/2$ and $\hat{J} = 3/2$ respectively. The optical transitions between the $2^2S_{1/2}$ state to the $2^2P_{1/2}$ and $2^2P_{3/2}$ states are respectively known as D_1 and D_2 lines. Figure 4.2 sketches the fine structure of the ${}^6\text{Li}$ atom, along with the relevant optical transitions [125].

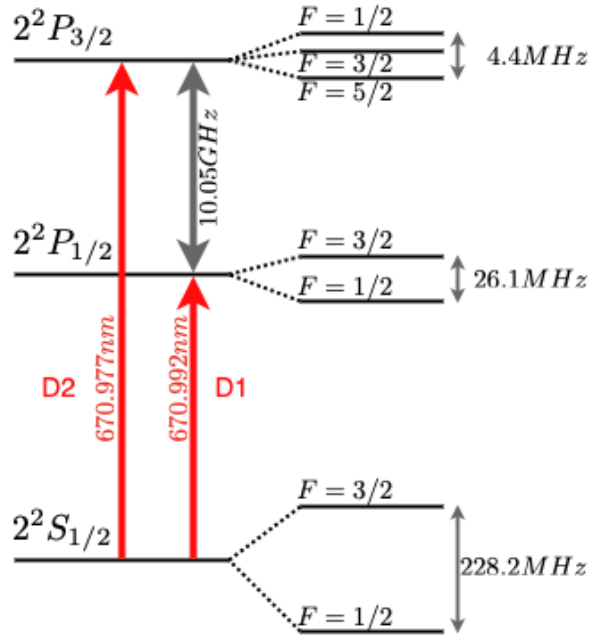


Figure 4.2: ${}^6\text{Li}$ fine and hyperfine structure at zero external magnetic field. The two relevant optical transitions used in the experiment are the D_1 and D_2 lines. Both optical transitions have similar linewidths $\Gamma = 2\pi \times 5.87$ MHz [125]. The fine splitting of the $2^2P_{3/2}$ level is not resolved.

To model the effect of both the hyperfine splitting and the external magnetic we consider the Hamiltonian [126]:

$$H = H_0 + H_{HF} + H_B = H_0 + \mathbf{A}\mathbf{I} \cdot \mathbf{J} - (\mu_B g_J \mathbf{J} + \mu_N g_I \mathbf{I}) \cdot \mathbf{B}, \quad (4.1)$$

where H_0 describe the fine structure Hamiltonian of an atom, H_{FH} the hyperfine Hamiltonian, and H_B the magnetic interaction Hamiltonian. The constants g_J and g_I are the electronic and nuclear Landé factors respectively. Table 4.1 shows the specific values of the Landé g-factors for the different electronic and nuclear states of

fermionic lithium. The hyperfine structure of the atom is describe by the total angular momentum of the outermost electron \mathbf{J} and the nuclear spin \mathbf{I} . The hyperfine shift as a function of the external magnetic field is given by [126]:

$$\frac{1}{h}\Delta E = a\mathbf{I} \cdot \mathbf{J} - \frac{1}{h}(\mu_B g_J \mathbf{J} + \mu_N g_I \mathbf{I}) \cdot \mathbf{B}, \quad (4.2)$$

where a is the hyperfine constant expressed in units of Hz. Considering a constant bias magnetic field of the form $\mathbf{B} = B_z \hat{z}$, then the energy shift is given by:

Symbol	Value	a[MHz]
g_I	-0.0004476540	
$g_J(2^2S_{1/2})$	2.0023010	152.1368407
$g_J(2^2P_{1/2})$	0.6668	17.4
$g_J(2^2P_{3/2})$	1.335	-1.1

Table 4.1: Landé factors for ${}^6\text{Li}$ [125].

$$\frac{1}{h}\Delta E = aI_z J_z + \frac{a}{2}(J_+ I_- + J_- I_+) + \left(\frac{\mu_B g_J}{h} J_z + \frac{\mu_N g_I}{h} I_z\right) B_z, \quad (4.3)$$

where J_{\pm} are the raising and lowering operators respectively. The hamiltonian contribution shown in (4.3) can be solved analytically for $J = 1/2$, known as the Breit-Rabi solution. The energy splitting is given by [126, 127]:

$$\frac{1}{h}\Delta E_{F=I\pm\frac{1}{2}} = -\frac{(I+1/2)}{2(2I+1)}a + \frac{\mu_N g_I m_F B}{h} \pm \frac{(I+1/2)}{2}a\sqrt{1 + \frac{2m_F}{I+1/2}x + x^2}, \quad (4.4)$$

where $x = \left(\frac{\mu_B g_J - \mu_N g_I}{ah(I+1/2)}\right) B$. For the $J \neq 1/2$ the solution to (4.3) must be obtained numerically. Figure 4.3 show the energy shifts of the $2^2S_{1/2}$, $2^2P_{1/2}$ and $2^2P_{3/2}$ states of ${}^6\text{Li}$ as a function of the external magnetic field.

At zero external magnetic field, the ground state $2^2S_{1/2}$ splits in two hyperfine levels: $|2^2S_{1/2}, F = 1/2\rangle$ and $|2^2S_{1/2}, F = 3/2\rangle$ separated by 228.2 MHz. The state $2^2P_{3/2}$ hyperfine splitting is unresolved, meaning the separation between the states with $F = 1/2$ and $F = 5/2$ is less than the transition natural linewidth, as shown in Figure 4.2.

For low magnetic fields ($B \lesssim 30$ G for ${}^6\text{Li}$) the Zeeman effect is a weak perturbation to the hyperfine structure, producing the expected linear Zeeman effect. In this regime, the description using the $|F, m_F\rangle$ is still valid. For higher magnetic fields,

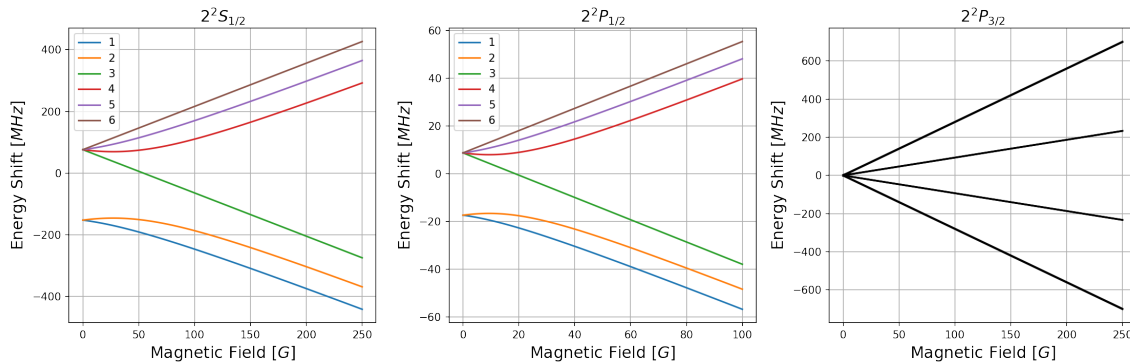


Figure 4.3: Hyperfine splitting as a function of the external magnetic field for the states $2^2S_{1/2}$, $2^2P_{1/2}$ and $2^2P_{3/2}$ of ^6Li . For the former two states, we use the Breit-Rabi formula (4.4), meanwhile for the state $2^2P_{3/2}$ we must solve numerically (4.3).

this is not the case [126]. At higher fields, the Zeeman effect dominates over the hyperfine structure, causing the electron and nuclear spin to decouple. This regime is also known as the Paschen-Back regime. In this regime, the F description is no longer valid requiring the electronic and nuclear spin projections, m_J and m_I , to describe the states correctly. In the Paschen-Back regime, the hyperfine splitting between states with the same m_J quantum number remains almost constant, as shown in Figure 4.3.

4.1.3 Laser sources

For all experiments reported in this thesis, we employed different laser sources to manipulate the atomic samples. Two red lasers near 671 nm were used for the initial cooling stages and imaging (D_1 and D_2 lines of ^6Li), two infrared lasers at 1064 nm and 1073 nm for creating a crossed optical dipole trap (cODT), and finally, a 532 nm green laser beam to engineer the final dark potential, where all the experiments are carried out.

671 nm laser sources

We use the optical transitions between $2^2S_{1/2}$ and $2^2P_{1/2}$ and $2^2P_{3/2}$ states to perform the initial stages of cooling. The $2^2P_{1/2}$ and $2^2P_{3/2}$ states are separated by 10 GHz, requiring two distinct laser sources. We employed two Toptica TA-Pro lasers: one locked to the D_1 transition using standard saturated absorption spectroscopy, the

other one is locked to the D_2 transition using a frequency modulation spectroscopy [123]. To address the ground state manifold ($2^2S_{1/2}$) sublevels, instead, we use a single laser for both cooling and repumping frequencies required for the MOT, and the D_1 cooling stage, since the hyperfine splitting is only 228 MHz. The frequency separation between cooling and repumping is achieved through a series of Acousto-Optical Modulators (AOMs). To increase the available power, we employed two TA-Boost amplifiers. For imaging, we employ the D_2 laser to drive the transition from one of the $m_j = -1/2$ ($|1\rangle$, $|2\rangle$, $|3\rangle$) states to the $m_j = -3/2$ excited manifold. To compensate the energy shift of the D_2 transition in the presence of a large magnetic field (690-900 G), that is of the order of 1 GHz, we employ a combination of AOMs, starting from the cooling and repumping frequencies at 0 field [123].

Optical dipole traps

To reach quantum degeneracy, we confine the atoms in optical dipole traps using far off-resonance laser light, which exerts a conservative force on the atoms. This force arises from the interaction between the laser's electric field and the induced atomic dipole moment [126, 127]. The electric field \mathbf{E} induces a dipole moment $\mathbf{p} = \alpha \mathbf{E}$, where α is the scalar the complex polarizability of the atomic medium [126, 127]. More generally α can be described as a tensor [10], which off-diagonal components can be used in many scenarios such as off-resonant Faraday imaging [128]. The induced dipole moment, interacts with the external electric field, and gives rise to the dipole potential:

$$U_{\text{dip}} = -\frac{1}{2} \langle \mathbf{p} \cdot \mathbf{E} \rangle = -\frac{\text{Re}(\alpha)}{2} |\mathbf{E}|^2. \quad (4.5)$$

From a semiclassical approach considering the interaction between a two-level atom with the classical radiation field the dipole potential can be written as [10, 126]:

$$U_{\text{dip}}(\mathbf{r}) \approx \frac{3\pi c^2}{2\omega_0^3} \frac{\Gamma}{\Delta} I(\mathbf{r}), \quad (4.6)$$

where ω_0 is the two-level atom resonant frequency, Γ the linewidth, and $\Delta = \omega - \omega_0$ is the detuning of the laser light from the transition. Additionally from the conservative potential Eq (4.6), the light-atom interaction considers a dissipative scattering which depends on $\text{Im}(\alpha) \sim 1/\Delta^2$, making it negligible for far-off resonant beam. The dipole potential depends on the light intensity, and it is either attractive or repulsive according to the frequency of the laser light. With red detuned laser frequencies,

the potential attracts has a minimum at the maximum of intensity, while for blue detuned light the minimum of intensity provides the minimum of the potential.

To manipulate the atoms in the experiment we make use of such optical potentials. We use two (red-detuned) high-power infrared (IR) beams: an IPG laser: 1073 nm multi-mode ytterbium fiber laser with a maximum power of 200 W, and a Mephisto laser: a 1064 nm Nd:YAG laser with a maximum output power of 50 W. The power of arriving to the atoms is stabilized using AOMs controlled via a feedback loop comprising a photodiode that measures a fraction of the light arriving to the atoms from the transmission leak of one of the mirrors in the laser path, and a commercial analog PID controller. Both IR beams are focused at the center of the science chamber, crossing at an angle of approximately 14° , see Figure 4.4, with similar waists around $40 \mu\text{m}$. To increase the trapping volume, the position of the IPG waist was rapidly varied along the x-axis by modulating the amplitude and frequency of the AOM driving signal out of phase, effectively increasing the beam waist to $80 \mu\text{m}$ [123].

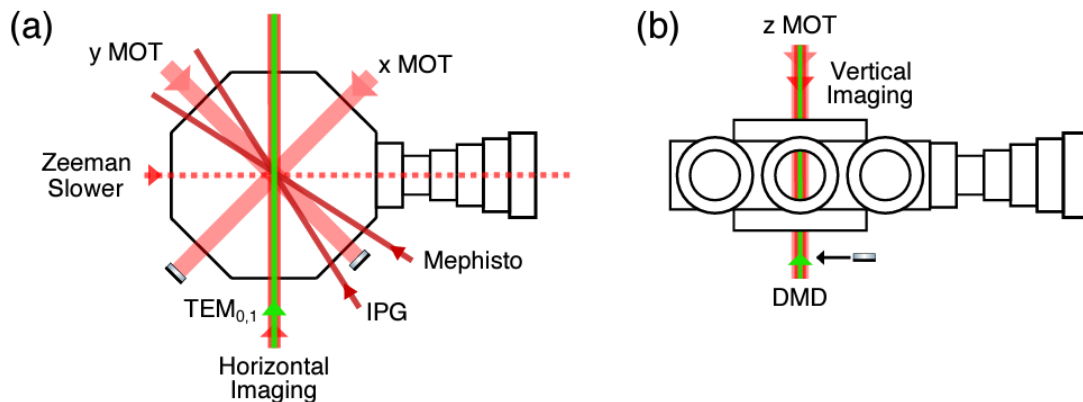


Figure 4.4: Schematic representation of the laser beams viewed a) from above and b) from the side. Image taken from [129].

The final confining trap, consist of two blue-detuned laser beams derived from a Verdi V8 laser at 532 nm. The first beam has a $\text{TEM}_{0,1}$ mode spatial profile [129], characterized by a vertical waist (along the z -axis) of $\sigma_z = 8.73 \mu\text{m}$ and a horizontal waist of $\sigma_{x,y} = 400 \mu\text{m}$. The $\text{TEM}_{0,1}$ beam intercepts the cODT at $\sim 45^\circ$ along the horizontal plane of the experiment, see Figure 4.4, compressing the atomic cloud in the z -direction, trapping them in the low-intensity region. A more detailed description of the optical path and design of the optical potential can be found in [129]. The second 532 nm beam is used to create arbitrary optical potentials using a digital micromirror

device (DMD). This beam propagates along the vertical axis of the experiment (see Figure 4.4), and allows the control over the system's geometry in the horizontal plane. Similar to the IR laser beams, both 532 nm beams are independently intensity stabilized using the combination of AOMs and photodiodes [129].

4.1.4 Reaching quantum degeneracy

To reach quantum degeneracy in the final dark-box potential, we follow the experimental sequence.

A first stage of slowing down the atomic beam originating in the oven is performed using the standard 1D cooling scheme in a Zeeman Slower [126, 127]. In this section of the experiment, the atoms are decelerated from velocities on the order of 800 m/s to approximately 60 m/s [123]. The terminal velocity of the atoms is enough for them to remain confined in a 3D Magneto-optical trap (MOT) located in the center of the science chamber. We typically load the MOT for 6 s. The temperature of the atoms in the MOT is on the order of a few mK. Next, the temperature is reduced closer to the Doppler limit ($T_D = 141\mu\text{K}$) by applying the standard D_2 optical molasses. The non-resolved excited manifold structure of the $2^2P_{3/2}$ impede the efficient cooling of the technique, eventually reaching temperatures $\sim 3 - 4T_D$. Contrary to other atomic species, processes like the Sisyphus cooling are not performed during the D_2 optical molasses for similar reasons. To further cool the atomic cloud, we employ a D_1 gray molasses stage [130, 131] to achieve sub-Doppler temperatures in the order of $40\mu\text{K}$. During the gray molasses stage, most of the atoms are optically pumped to the $F = 1/2$ state, allowing for the natural preparation of the spin mixture of states $|1\rangle$ and $|2\rangle$ in the presence of a biased magnetic field.

Following the D_1 gray molasses stage, we turn on the IR laser beams creating a conservative potential where the atoms get confined through the optical dipole force [10]. The initial trap depth of this potential is $\sim 5\text{ mK}$. After capturing the atoms in the ODT, we ramp up a bias magnetic field toward the center of the Feshbach resonance between the states $|1\rangle$ and $|2\rangle$ at 832 G [132]. We take advantage of the resonant interaction (see section 2.2.1) and fast thermalization rates [9] at unitarity to perform runaway evaporative cooling by lowering the power of both IR laser beams. During the evaporation ramps, the atomic cloud, initially dominated by the high-power IPG beam profile, slowly moves towards the crossing position between the IPG and Mephisto beams. There the atomic cloud reaches quantum degeneracy, see

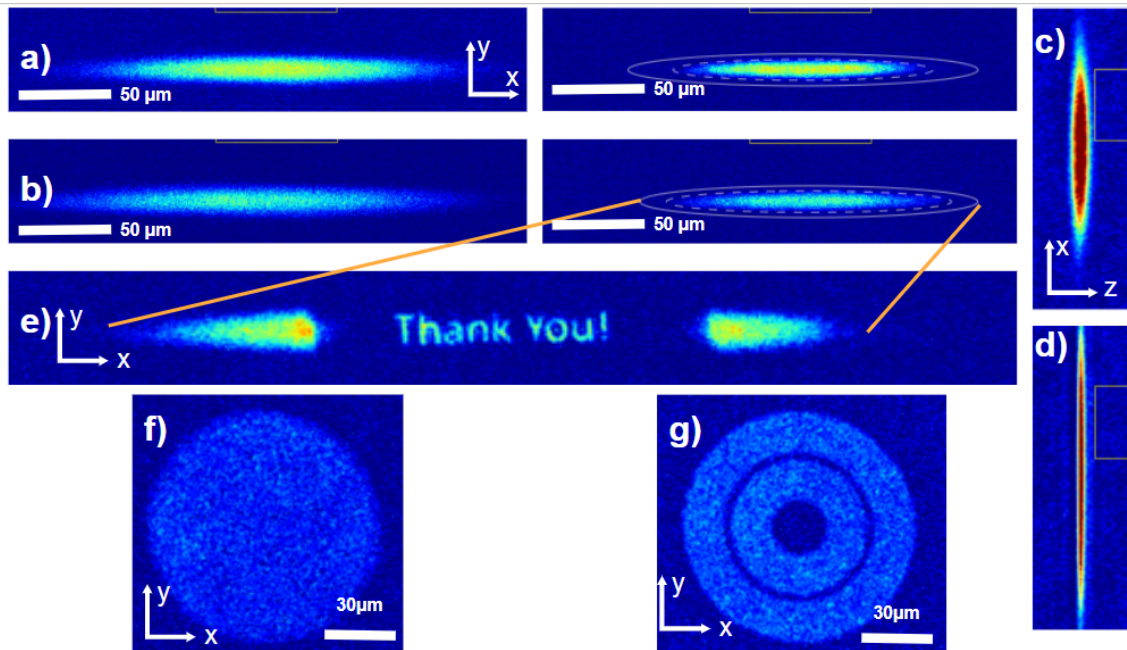


Figure 4.5: Atomic sample imaged along the vertical axis: trapped by the combination of the a) IPG and Mephisto. b) IPG, Mephisto, and $TEM_{0,1}$ laser beams (left) in the unitary regime at 832G, and (right) in the BEC regime at 702G. Atomic sample imaged along the horizontal axis: in the c) IR cigar, and in the d) $TEM_{0,1}$ alone. e) DMD and $TEM_{0,1}$ laser beams in the mBEC. Engraving "Thank You!" is employed to focus the DMD laser beam. f-g) Examples of trapping potentials in the final dark-box potential.

Figure 4.5 a). Finally, by tuning the magnetic field, we modify the atomic interaction through the Feshbach resonance, allowing us to create the molecular Bose-Einstein condensate of tightly bound atoms, a strongly interacting Fermi gas, or a Bardeen-Cooper-Schiffer gas of Cooper-pairs-like states.

After the creation of the desired superfluid regime, we transfer the atoms into the final dark-box potential. We slowly ramp up the power of the $TEM_{0,1}$ laser beam creating a combined optical potential where the vertical direction is compressed, see Figure 4.5 b-d). Due to the focus requirements of the high-NA objective, the vertical position of the $TEM_{0,1}$ must always remain in the same position to provide stability of the experiments over multiple days. Such deviations may arise from thermal or mechanical drifts that are difficult to suppress. To overcome this constraint, we employ a screw driven by a picomotor controller located on the last mirror of the optical path of the $TEM_{0,1}$ beam. This controller allows us to fine-tune the position of the $TEM_{0,1}$ potential up to the resolution provided by our imaging system along

the horizontal axis of $\sim 6 \mu\text{m}$, see Figure 4.5 d).

After turning on the $\text{TEM}_{0,1}$ laser beam, we ramp up the DMD laser beam to confine the atoms in the horizontal plane. Subsequently, we ramp down the power of the IR laser beam such that the atoms remain confined within the low-intensity region set by the 532 nm $\text{TEM}_{0,1}$ + DMD optical potential, see Figure 4.5 f-g). After realizing the atoms $\text{TEM}_{0,1}$ + DMD optical potential we align the focus position of the DMD beam to the atomic plane. For this, we evaluate the sharpness of the density profile after shining a "Thank you!" pattern onto the atoms, by adjusting the vertical position of the high-resolution objective.

In the final trapping configuration set by the $\text{TEM}_{0,1}$ + DMD optical potential we remain with approximately $N \sim 30 \cdot 10^3$ atoms per spin, for traps with maximum extension radial extension of $45 \mu\text{m}$, and vertically extended $\sim 6 \mu\text{m}$ due to the harmonic confinement, however the latter might change depending on the interacting regime.

4.2 High-resolution imaging

4.2.1 Absorption imaging

To acquire images the density distribution of the atomic sample (such as Figure 4.5), we use absorption imaging. A resonant pulse of light is directed onto the atoms, and the resulting intensity profile is captured by a CCD camera. The presence of atoms is indicated by the presence of a shadow in the acquired light pattern, caused by the absorption of light by the atoms. This behavior is encapsulated by the Lambert-Beer law stating:

$$\frac{dI}{dz}(x, y) = -n(x, y)\sigma, \quad (4.7)$$

where I is the light intensity propagating along the z direction and illuminating the atomic cloud of density n , and σ is the atom-photon interaction cross-section [126]. In general σ is a function of the intensity making the absorption profile depends on the intensity regime. In the low intensity regime, the measured absorption profile doesn't depend on the intensity [126] since $\sigma \rightarrow \sigma_0$ in this regime. The value $\sigma_0 = \frac{3\lambda^2}{2\pi}$ is known as the resonant cross-section of the transition.

When dealing with optically dense clouds, the number of transmitted photons in the low-intensity regime becomes very low, reducing the signal-to-noise ratio (SNR). To increase the SNR we require entering the limit of high-intensity imaging, where saturation effects cannot be neglected [133], modifying the cross-section in the Lambert-Beer law [126] as:

$$\frac{dI}{dz}(x, y) = -n(x, y, z) \frac{\sigma_{eff} I}{1 + I/I_{eff}}, \quad (4.8)$$

where $\sigma_{eff} = \sigma_0/\alpha$ and $I_{eff} = \beta I_{sat}$ are the effective cross-section and effective saturation intensity, respectively. The complex multilevel structure of the atomic transition and imperfections in the alignment of the imaging beam polarization with the quantization axis might affect the ideal values of cross-section σ_0 and saturation intensity I_{sat} for the two-level system. The shadow profile of the atomic cloud that we acquire with absorption imaging, provides a measurement of the local optical density OD, which can be obtained by integrating the previous equation along the z -imaging direction:

$$OD(x, y) = \sigma_{eff} n_{2d}(x, y) = -\log \frac{I_{in}}{I_{out}} - \frac{I_{out} - I_{in}}{I_{eff}}, \quad (4.9)$$

where I_{in} and I_{out} are the incident and transmitted intensity, respectively. When $I \ll I_{eff}$, the linear term can be neglected recovering the simple Lambert-Beer law that is independent of the imaging intensity. The integrated atomic density n_{2d} is thus given by:

$$n_{2d}(x, y) = -\frac{\alpha}{\sigma_0} \log \frac{I_{in}}{I_{out}} - \frac{\alpha}{\beta \sigma_0} \frac{I_{out} - I_{in}}{I_{eff}}. \quad (4.10)$$

To have a reliable measurement of the atomic density, the coefficients α and β parameters must be calibrated. The techniques employed for the calibration are explained in Refs. [53, 133]. In summary, we prepare an atomic cloud with a stable number of atoms and we measure its atom number with reliable low-intensity horizontal imaging. We then image the same cloud with the vertical setup, and calibrate the value of β such that the OD profiles acquired with different light intensities show the same profile. The value of α is instead obtained by constraining the number of atoms measured with the vertical imaging to be the same as measured with the horizontal one [133].

4.2.2 Vertical imaging setup

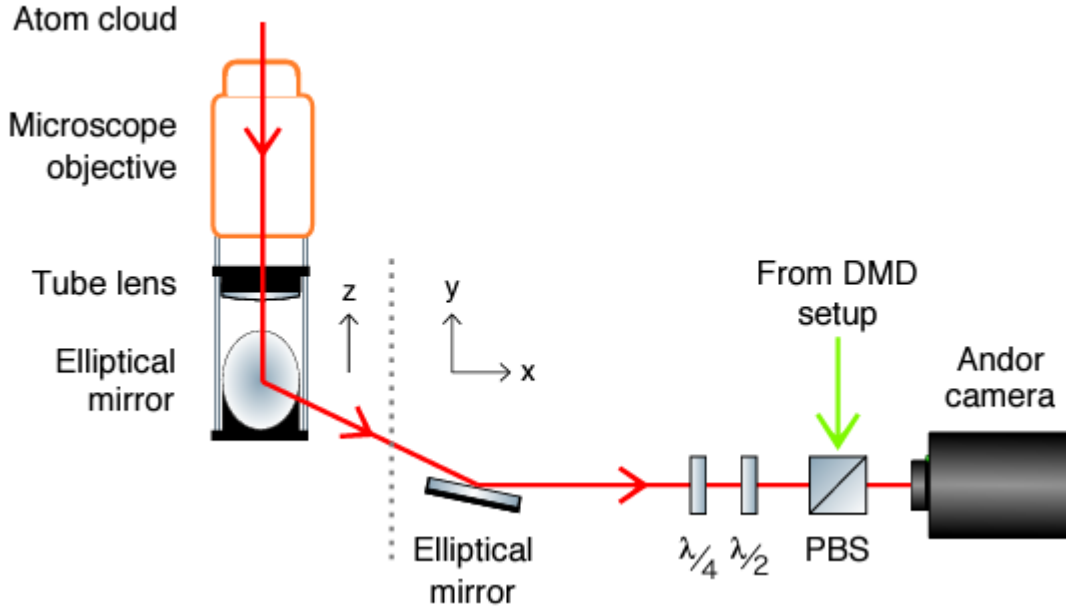


Figure 4.6: Schematic representation of optical path for the high-resolution imaging along the vertical direction. Image taken from [129].

The vertical imaging system consists of a high-resolution microscope objective designed to be achromatic for 671 nm and 532 nm. Allowing for the simultaneous imaging of the atomic cloud and the projection of arbitrary optical potentials using the DMD. The resolution of the imaging system is measured to be below $1 \mu\text{m}$ for both wavelengths [129]. The imaging light is focused using a lens with a focal length of $f = 1000 \text{ mm}$ onto an Andor iXon3 EMCCD camera with $13 \mu\text{m} \times 13 \mu\text{m}$ pixels. The total magnification of the vertical imaging system is $M = 21.8$. More detailed information on the vertical imaging setup and the high-resolution objective can be found in [129]. The Andor camera is operated on the Fast Kinetic Series (FKS) acquisition mode: we acquire the sequence of 3 images required for the absorption imaging with a short delay time of the order of $200 \mu\text{s}$, by reducing the portion of the camera chip illuminated by the light [133]. Moreover, to reach the high spatial resolution of our vertical imaging system, it is essential to minimize the atomic motion caused by the recoil from scattered photons during the imaging pulse. To this end, we use short imaging pulses of $4 \mu\text{s}$ with an intensity of $\sim 3I_{sat}$.

4.3 Arbitrary optical potentials with DMD

Ultracold atom experiments offer the remarkable possibility of shaping the potential landscape experienced by the atoms by controlling the spatial intensity profile of a far-off-resonance laser beam. Different potential landscapes can be made by the interference of two or more laser beams, creating a perfect or disordered lattice. Similar optical potentials can be created through the projection of certain phase, or intensity masks. However, recently, the integration of Spatial Light Modulators (SLMs) into atomic physics experiments have opened the way to flexible static and dynamic optical potentials with unprecedented control. In particular, in our experiment we make use of a Digital Micromirror Device (DMD) to achieve the control over the potential landscape.

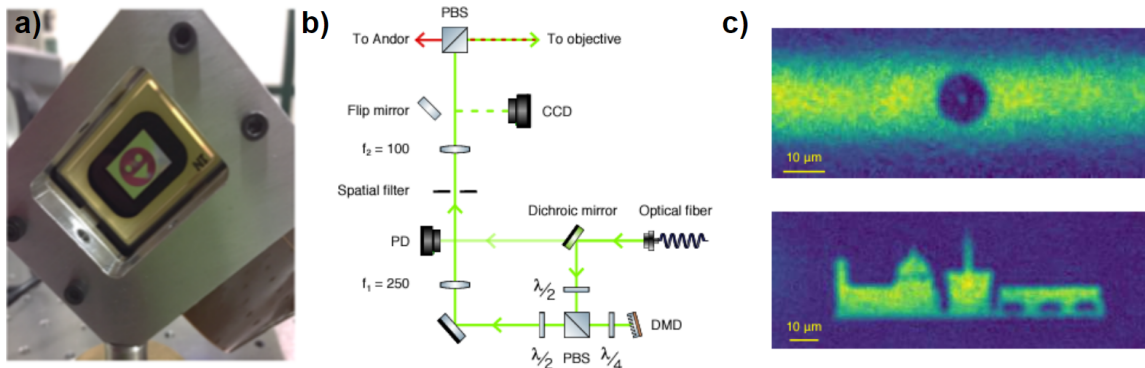


Figure 4.7: The Digital Micromirror Device (DMD). (a) Picture of the DMD mounted displaying a smile image. (b) Sketch of the states of the DMD micro-mirrors: when the DMD is off all micro-mirrors occupy the rest position tilted at 0° , when a voltage is applied to a mirror it tilts either by $+12^\circ$ or -12° , labeled as ON and OFF state. Image taken from [129].

DMDs are well-suited for such applications due to their capacity to generate high-resolution static images and offer dynamic control on timescales comparable to atomic response times. In our experimental setup, we employ a Vialux V-7000 High-Speed Module DMD, which features the Texas Instruments Discovery 4100 0.7" XGA 2xLVDS (DLP7000) chip. This chip contains an array of 1024×768 micromirrors, each with a pitch of $13.68 \mu\text{m}$. Each micromirror can tilt by $+12^\circ$ (ON) or -12° (OFF), reflecting light in different directions depending on its state. By loading a binary image onto the DMD, the micromirrors align according to their ON or OFF states, effectively acting as a programmable light mask. For example, as shown in Figure 4.7 a), a smile pattern is displayed on the DMD. The reflected light can then

be projected onto the atomic cloud. While any off-resonant light can be used to impose a desired potential, blue-detuned light allows the design of repulsive regions within the atomic potential landscape. The design of homogeneous potential regions in space is achieved with *minimal* effort, simply by not shining light into those regions. This is not the case, when trying to design optical potentials using red-detuned light, where the consideration of the smoothness/roughness and sharpness of the imprinted potential are crucial things to consider. In Fig. 4.7 c), we show examples of DMD-generated arbitrary optical potentials projected onto our quasi-2D atomic cloud.

4.3.1 DMD optical path

We project the DMD-generated optical potentials onto the atomic cloud using the high-resolution microscope objective system used for imaging, achieving sub-micron resolution at 532 nm [129]. The optical setup combines the imaging system shown in Figure 4.6 with the optical setup shown in Figure 4.7 b). At the output of a fiber, a Gaussian beam with a waist of ~ 7 mm, effectively illuminating the 1×1.5 cm DMD screen. This beam is directed to the DMD through a mirror, and the leakage is monitored by a photodiode to stabilize the beam intensity through a PID feedback loop. The PID adjusts the amplitude of an AOM before the input to the optical fiber, regulating its output intensity. The co-linear configuration with an incident angle of $\theta_i = 12^\circ$ is used, and the reflected and incident beams are recombined through a polarizing beam splitter (PBS). A telescope demagnifies the DMD pattern a factor of 2.52. An adjustable iris positioned in the focal plane of the first lens acts as a spatial filter to smooth the DMD image profile.

The DMD projection is combined with the imaging path in a 2" PBS, and then focused onto the atomic cloud by the objective system, resulting in an overall demagnification factor of 55. This reduces a single DMD mirror to $\sim 0.25 \mu\text{m}$ in the atomic plane [129]. A flip mirror after the first telescope focuses the DMD image onto a Thorlabs CMOS camera, enabling pattern checks, calibration, and running the feedback routine required for the creation of smooth intensity profiles.

4.3.2 Controlling the DMD

To control the optical potentials, i.e the images displayed in the micro-mirror array, we interface the DMD device with a control software. The control software is capable of loading, changing, and running any desired sequence of images. The software is based on the ALP4lib open-source Python module by Sebastien Popoff [134], which allows for the loading of long sequences of images onto the device, as well as setting the configuration properties of the sequence. Both the feedback program and the one used for producing dynamic optical potentials employ ALP4lib to interface with the DMD.

The algorithm employed for the feedback process is explained in detail in Ref. [129]. The idea behind this algorithm is to run a feedback process comparing the image generated by the DMD, measured by the Thorlabs CMOS camera shown in Figure 4.7, and the binary image reproduced by the mirror array. Using this procedure, we can arbitrarily create smooth intensity profiles. Examples of use consist of transforming the input gaussian beam into flat-top homogeneous profiles with different gray levels. Or equivalently, linearly varying intensity profiles, such Figure 4.12. After running the feedback profiles, the mirror ON-OFF image is stored, and can be used to generate the final optical potentials.

The dynamic potentials instead are created using a list of matrices that define the different patterns the DMD will project. After the design of the sequence of images, the dynamic program loads the matrices onto the V-7000 Vialux board. The board is configured such that every time a trigger pulse arrives to the V-7000, the mirror pattern change to next pattern. The minimum time a pattern can be shown is $44 \mu s$, allowing the device to reach its maximum frame rate of 22 kHz. However, we constrain all experimental sequences to a minimum of $60 \mu s$ to avoid any trigger skipping on the DMD board. Additionally, the process of switching images takes about $10 \mu s$, during which all mirrors return to their rest position before tilting to the new state, no light is projected onto the cloud during this $10 \mu s$ window [129]. In general, the flickering can lead to heating of the cloud. This effect can be crucial when the reaction time of the atomic system, set by the chemical potential μ , is of the same order of timescales. However, in the experiment the typical energy scale, set by the Fermi energy, are below $\mu \leq E_F \lesssim 2\pi \times 20 kHz$. Making negligible the heating mechanism.

4.4 Density excitations

As we mentioned in section 2.3.1, a fundamental property of superfluids is the existence of excitations which do not destroy the superfluid state. The maximum velocity an obstacle can go in a superfluid without perturbing it is in principle the critical velocity [61, 62]. Further corrections must be made when considering a real obstacle, such as considering the local values for the critical velocity [135]. For weakly interacting BEC's, the critical velocity coincides with the speed of sound, while in the BCS regime it corresponds to the pair breaking velocity.

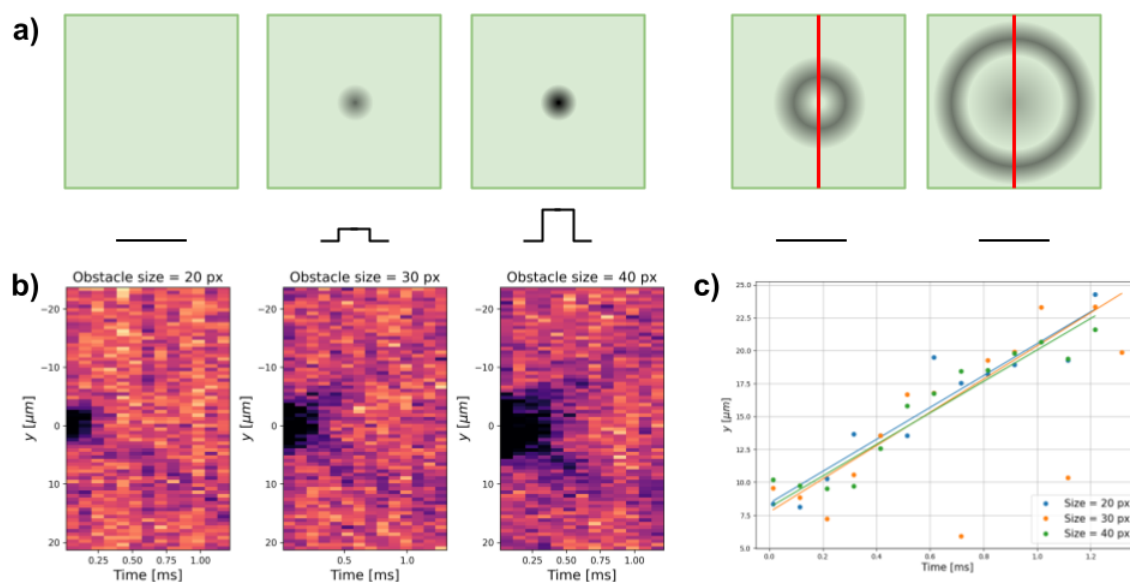


Figure 4.8: a) Protocol for the measurement of the speed of sound using the density depletion method. The height of the obstacle is shown below each panel. We measure the atomic density profile along the red line vs time. b) Experimentally obtained profiles as a function of time. From left to right: an obstacle of size 5, 7.5, and 10 μm is removed, a subtle wavefront propagates in time traveling at the speed of sound. b) Propagation trajectory of the density dip. For all obstacle sizes the wavefront propagates at the same speed seen by the linear fits.

Many experiments have measured this behavior with great accuracy [61, 62]. They achieved this by superimposing a moving lattice inside the superfluid, and measuring the effect it caused to the superfluid density. Another method performed, mainly motivated by numerical simulations, is measuring the restoring dynamics of the superfluid after removing a static obstacle. To test the capabilities of our system, we

probed the response of the mBEC to such protocol. Initially, we start by creating a homogeneous BEC in a squared shape trap designed using the DMD. Then, we slowly ramp up the height of an obstacle potential, until the obstacle potential height is well above the chemical potential of the BEC, see see Figure 4.8 a). Suddenly, we remove the obstacle, and observe the propagation of the density depletion as a function of time. In Figure 4.8 b), we observe the behavior of the average density profile (out of 5 repetitions) along the one axis (red line of panel a). We observe that the density depletion propagates at the same speed independently from the size of the obstacle, giving a clear measurement of the speed of sound.

Although we provide a possible protocol for measuring the speed of sound, the signal-to-noise ratio is low, making the measurement noisy and unreliable. Performing azimuthal averaging could improve the signal to noise. However, in addition to modifying the superfluid quantum statistics across the BEC-BCS crossover, one of the most striking differences between these regimes is the compressibility of the system [6, 136]. This behavior is a consequence of the underlying statistics governing the superfluid. Fermionic superfluids tend to be less compressible due to the Fermi pressure, while bosonic superfluids are much more compressible. Moreover, the contrast of density excitations is intrinsically related to the compressibility of the system ($\kappa = n^{-2} \frac{dn}{d\mu} \rightarrow \frac{1}{n} \frac{dn}{dx} = \kappa n \frac{d\mu}{dx}$). Hence, we can expect the signal-to-noise ratio of the subtle decompression to be further reduced in the UFG and BCS superfluids.

To increase the signal-to-noise ratio of the density excitations, we opted for the compression protocol shown in Figure 4.9 a-c). Using the walls defined by the DMD potential, we move the a boundary of the system at a constant rate for a small extension. We used a box of length $35 \mu\text{m}$. We compress one direction by an amount $\Delta x = 1.25, 2.5, \text{ and } 3.75 \mu\text{m}$ the constant rate of $\sim 2.5 \mu\text{m}/\text{ms}$. As shown in Figure 4.9 d-e-f), we observe the propagation of a density wave in all three d) BEC, e) UFG, and f) BCS superfluids with a significant larger signal-to-noise ratio.

The observed dynamics are quite interesting and deserve a detailed study on its own. A first compression wave leads the propagation, with a rarefaction pulse(s) behind it. In all interaction regimes, we observe the compression pulse to be initially compact and spreading over time. This behavior is expected due to the population of many k-modes in the initial compression. In homogeneous systems, sound propagation is expected to be damped over time. The damping coefficient Γ strongly depend on the wavenumber k , and the sound diffusivity coefficient D , as $\Gamma \approx Dk^2$. Recent

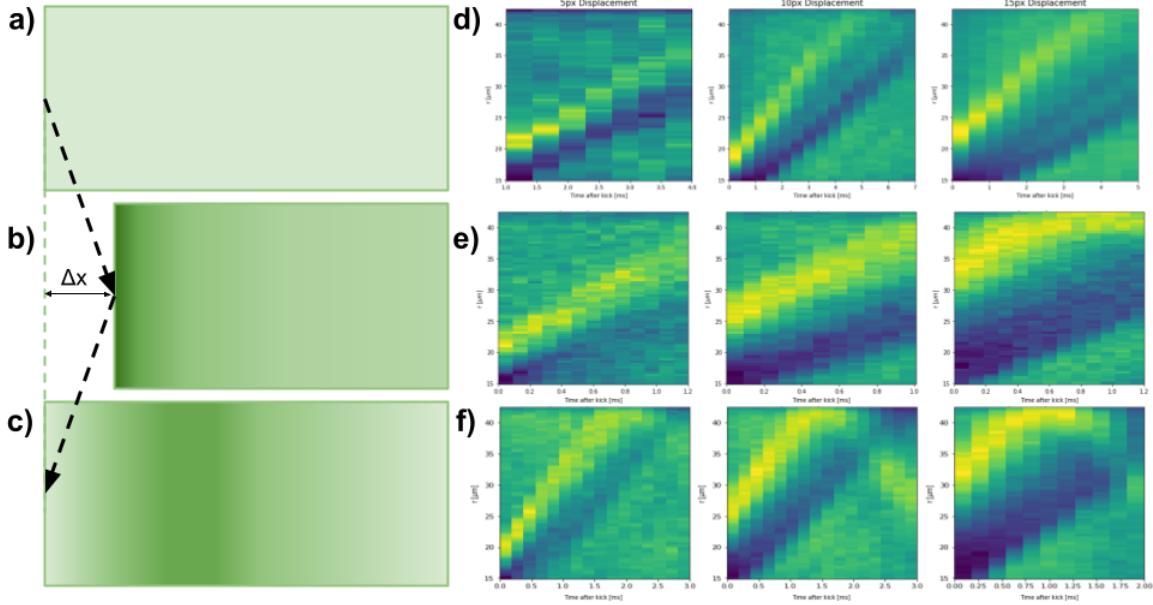


Figure 4.9: a-c) Compression protocol for exciting a density wave. The average density profile as a function of time is shown for a d) BEC, e) UFG, and f) BCS superfluids. We compress three different amounts: $\Delta x = 1.25, 2.5, \text{ and } 3.75 \mu\text{m}$.

experiments have investigated the sound diffusivity coefficients across the different superfluids [89, 137–139]. At unitarity, the diffusivity coefficient $D \approx 1.5 \frac{\hbar}{m}$ is almost independent on the temperature (for $T < T_c$) [89]. In the weakly interacting BEC regime, instead, it was measured that $D \approx 3.0 \frac{\hbar}{m}$, and was found to be independent of the interaction regime [137]. Finally, the emergence of sound in the deep BCS regime was measured, and found that for weak interactions, quasiparticle transport the excitations of the Fermi system evolve from broad particle-hole excitations to a narrow collective sound mode, yielding an almost Heisenberg limited sound attenuation [138].

Moreover, the propagation speed of the compression wave is similar for the different compression lengths, see Figure 4.10 a). Normalizing the measured velocity of the compression wave to the Fermi velocity, v_F , we obtain the plot shown in Figure 4.10 b). We also show the expected normalized speed of sound obtain from the polytropic mean field model developed in section 2.2.3. In our 2D homogeneous system with transverse harmonic confinement, the normalized speed of sound is $c_s/v_F = \left(3 \cdot 2^{-\frac{13}{2}} k_F a_M\right)^{1/3}$ in the BEC limit, while $c_s/v_F = \sqrt{\xi^{3/4}/3}$ in the crossover regime. An effective $\xi = \xi(k_F a)$ can be extracted from MonteCarlo simulations [140], allowing us to extend the behavior across the full crossover. In the deep BCS limit the speed is instead

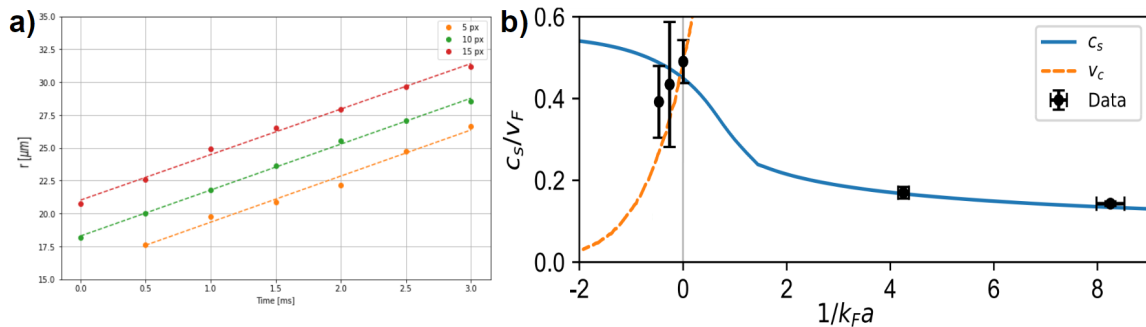


Figure 4.10: a) Trajectory of the compression pulse central position over time for different compression lengths in the BEC superfluid. b) Normalized speed of sound across the BEC-BCS crossover. Lines denote the speed of sound (blue), see Table 2.1, and the pair breaking velocity, see Figure 2.2.

fixed to $c_s/v_F = 1/\sqrt{3}$. The measured values align precisely with the expected behavior in the BEC regime. However, in the unitary and BCS regimes, they deviate slightly from the speed of sound calculations. Nonetheless, when comparing the data to the pair-breaking velocity [62], we find them to be in agreement.

The compression mode we excited not only encodes the dynamics of the critical velocity of excitations in the superfluid but also opens the way to study compression waves in the system. A noticeable feature of Figure 4.9 d-f) is the presence of a depletion region behind the compression, consisting of the rarefaction of the superfluid. Surprisingly, the behavior of the rarefaction region differs significantly between the interaction regimes and across different compression lengths. For instance, in the BEC case (Figure 4.9 d)), as we increase the compression of the condensate, the rarefaction splits into two rarefaction waves. Moreover, each wave seems to propagate at increasingly slower velocities.

The physics behind rarefaction waves in superfluids is quite interesting and well understood in the case of liquid He [141], where rarefaction waves are typically associated with heating waves. Only recently have studies been conducted on the dissipative shock waves generated by a quantum mechanical piston [142], where it was found that many aspects of the dynamics follow the predictions of classical dissipative shock theory rather than superfluid dispersive shock theory. Nonetheless, the study of the propagation of these waves in strongly interacting systems remains an active area of research [142, 143].

4.5 Excitation of persistent current states

Persistent currents in annular geometries have played an important role in revealing the quantum phase coherence of superconductors and mesoscopic electronic systems. Ultracold atomic gases in multiply connected traps also exhibit long-lived supercurrents, attracting significant interest both for fundamental studies of superfluid dynamics and as prototypes for atomtronics circuits [144, 145]. Such persistent currents in a toroidal superfluid have been observed in both bosonic [146–148] and fermionic [135, 149, 150] atomic gases.

Over the years, different techniques to excite persistent flows in ring-shaped superfluids have been successfully implemented [135, 146, 149, 150]: from two-photon transitions to transfer angular momentum, stirring an obstacle along the ring, and more recently, using a phase-imprinting protocol. In our experiment, we follow the latter approach, demonstrating the validity of this technique for fermionic superfluids across the crossover.

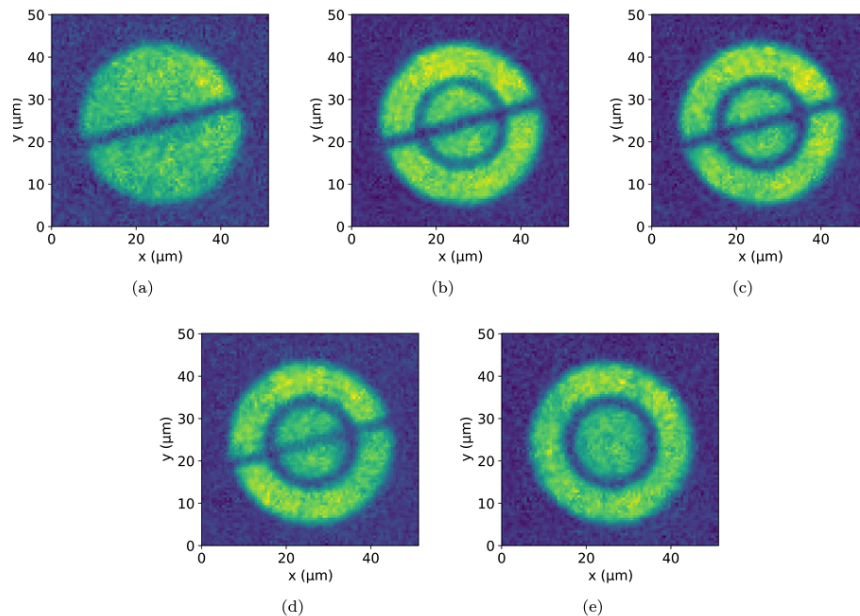


Figure 4.11: Sequence of steps employed for the creation of a static superfluid in the annular + disk configuration potential.

To excite persistent currents in our fermionic superfluids, we first need to engineer the transition from the cigar-shaped gas to the final ring-shaped trap. One of the key considerations during this transfer is the potential excitation of angular modes or the unintentional imprinting of velocity along the azimuthal direction, which can induce

spontaneous persistent flow. This is undesirable because we would lose precise control over the final state. For this reason, we designed [151, 152] the sequence of steps illustrated in Figure 4.11. We begin by transferring the gas from the cigar-shaped cloud into a circular trap, similar to Figure 4.5. To avoid azimuthal excitations, we raise a barrier that separates the trap into two semi-disks, with a height above the chemical potential. Next, a circular barrier with a radius of $10 \mu\text{m}$ is raised. Finally, the line barrier is removed by gradually decreasing the amount of light reflected by the DMD.

The final trap configuration consists of two distinct superfluids: one in a disk geometry and the other in an annulus. This particular geometry allows us to use the central superfluid as a phase reference when measuring the relative phase of the annular superfluid.

As mentioned above, we aim to excite persistent currents in the ring using a phase-imprinting protocol. This method is based on the fact that rapidly varying potentials tend to modify the local phase [135, 150]. To understand the relationship between phase and potentials, it is useful to analyze the case of a Bose-Einstein Condensate (BEC), where the Gross-Pitaevskii Equation (GPE) applies. Starting from the GPE, let us consider the wavefunction solution for a static potential V_{static} , with the solution given by $\psi(r, t)$. Then, for a short duration, we flash a potential V_{flash} , and consider the new solution as $\Psi(r, t) = \psi(r)e^{-i\phi(r, t)}$. After substitution, we obtain:

$$\hbar \frac{\partial \phi(\mathbf{r}, t)}{\partial t} = V_{flash}(\mathbf{r}, t) + \frac{\hbar}{2M} \left(\nabla^2 \phi + 2i \frac{\nabla \psi \cdot \nabla \phi}{\psi} \right), \quad (4.11)$$

In the limit of short imprinting time, such that there is no motion of the atoms, and considering a homogeneous BEC distribution, this relation reduces to the phase imprinting relation [150, 153]:

$$\hbar \frac{\partial \phi(\mathbf{r}, t)}{\partial t} \approx V_{flash}(\mathbf{r}, t) \rightarrow \phi(\mathbf{r}, t) = \frac{\Delta t}{\hbar} V_{flash}(\mathbf{r}, t), \quad (4.12)$$

where Δt is the total time the potential is flashed. Therefore, the phase imprinted to the condensate is given by the flashing potential V_{flash} . Using the off-resonant laser light out of the DMD with a intensity pattern $I(x, y)$, the atoms will experience a spatially varying light-shift potential $U(x, y) \propto I(x, y)$, hence acquiring the corresponding phase $\phi(x, y) \propto \Delta t I(x, y)$. This imprinting protocol has recently been analyzed for fermionic superfluids [154], by performing direct simulations of the Bogoliubov-

de-Gennes equations. Interestingly, they show the imprinting protocol is indeed able to set the phase of the order parameter.

Persistent current flows in ring shape superfluids can be identified with clear and distinct wavefunction states which are characterized by their flow around the enclosed region. We know the superfluid velocity is given by $\vec{v} = \frac{\hbar}{M} \nabla \phi$, and, the circulation around a closed loop is quantized: $\Gamma = w\kappa$ with w an integer number (see section 2.3.2). Hence, for our annular superfluid, the velocity flow is also *quantized*, and it must be given by $\vec{v} = \frac{\kappa}{2\pi} \frac{w}{r} \hat{\theta}$. The distinct wave functions characterizing the persistent current states are all of the form $\Psi(r, \theta) = \psi(r)e^{-iw\theta}$, with $\psi(r)$ taking care of the radial density profile of the ring potential.

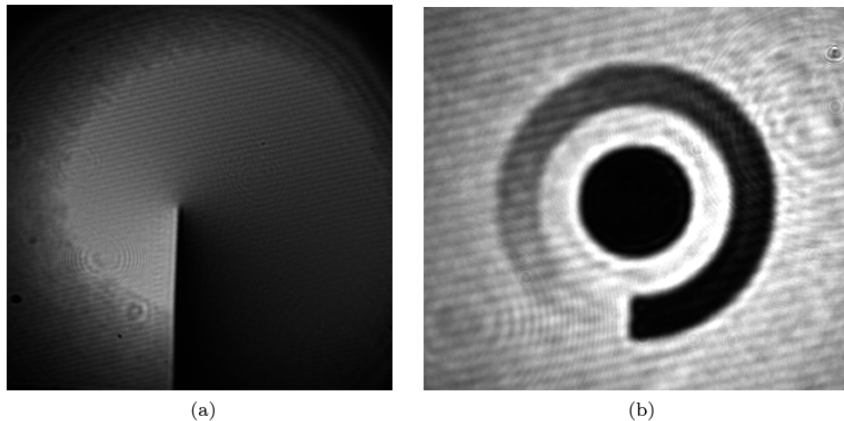


Figure 4.12: a) a) Light pattern with linearly increasing intensity along the azimuthal direction. (b) Light pattern used for the excitation of persistent current in the ring. Image taken from [151].

For accessing the persistent current states from the initially static superfluids created following the protocol of Figure 4.11, we require to imprint the corresponding phase profile $\phi = w\theta$. We achieve this by engineering an optical potential having the same functional form, as shown in Figure 4.12. We first feedback the intensity profile to match the intensity $I(r, \theta) \propto \theta$, and then we superimpose the resulting image into the ring mask as shown in Figure 4.12 b). Additional patterns with $I(r, \theta) \propto (N\theta)$ modulo 2π , with $N > 1$ were also tried and implemented in the following measurements when necessary.

The persistent current states are topological in nature, and hence are topologically protected by the system's geometry. However, their stability is not absolute since the ground state is static ($w = 0$). Indeed, the persistent currents can decay into lower

order states with the additional cost of emitting a quantum vortex into the background superfluid [135, 147, 155]. In Ref. [135], we studied in great detail the stability of such persistent states in the presence of an obstacle in the annular channel. For what concerns the experiments presented in this thesis, we only consider persistent states which are stable given our trap geometry and interaction regime.

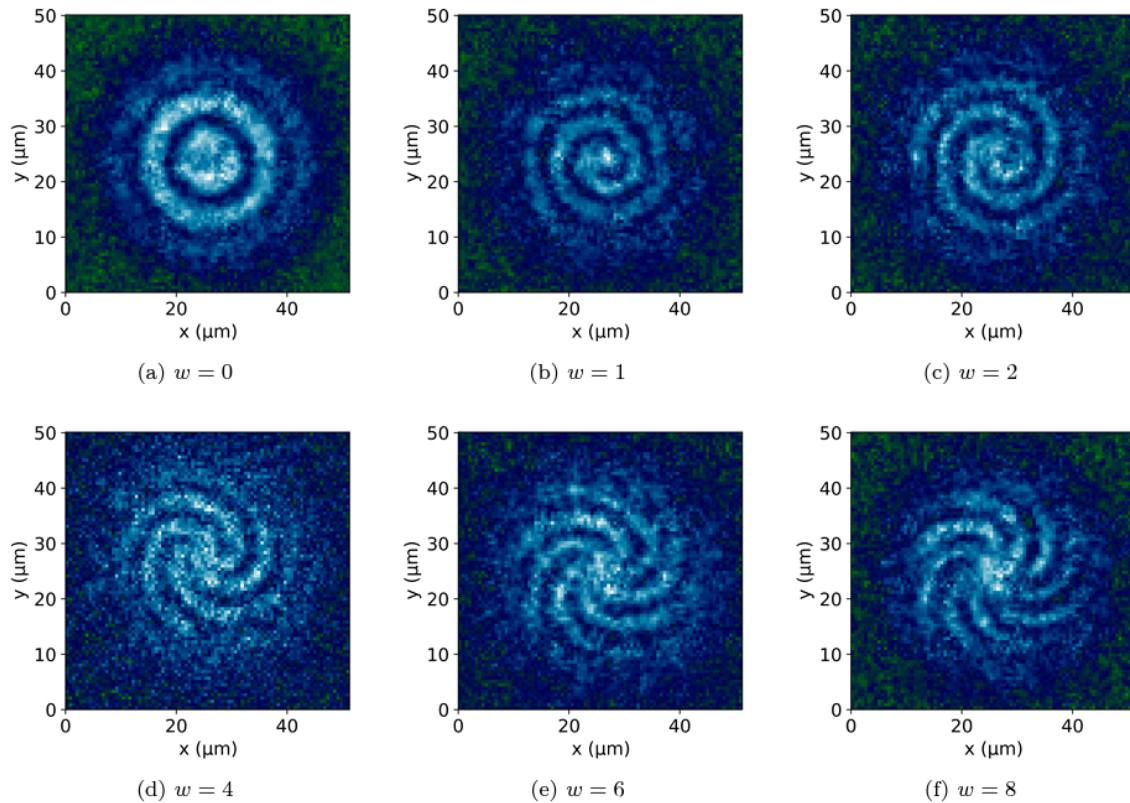


Figure 4.13: Example of interferograms for increasing winding number showcasing the spiral behavior of the interference between a persistent current state with a homogeneous phase reference. Image taken from [151].

To measure the presence of the persistent current states, i.e. a wavefunction of the form $\Psi(r, \theta) = \psi(r)e^{-iw\theta}$, we take advantage of atom interferometry [156]. By letting the system evolve in time-of-flight, we allow for the central disk superfluid interfere with the annular one. The interference signal measured after time-of-flight can be written as:

$$n(r, \theta) \approx |\Psi_{disk} + \Psi_{annular}|^2 = |\Psi_{disk}|^2 + |\Psi_{annular}|^2 + 2\text{Re}[\Psi_{disk}\Psi_{annular}^*]. \quad (4.13)$$

Assuming the disk wavefunction has a uniform phase, $\Psi_{disk}(r, \theta) = \psi_{disk}e^{i\phi_0}$, the interference term $Re[\Psi_{disk}\Psi_{annular}^*] \propto \cos(w\theta - \phi_0 + 2\pi r/\lambda)$, where λ characterizes the radial interference wavelength and depends on the initial separation between the disk and annular condensates, and the time-of-flight given for the measurement [156]. A notable feature of the interference term is its angular dependence. The resulting density profile exhibits a periodic modulation that cycles w times around the angular direction, indicating the presence of the associated persistent currents with winding number w . Examples of such interference patterns for increasing winding number are shown in Figure 4.13.

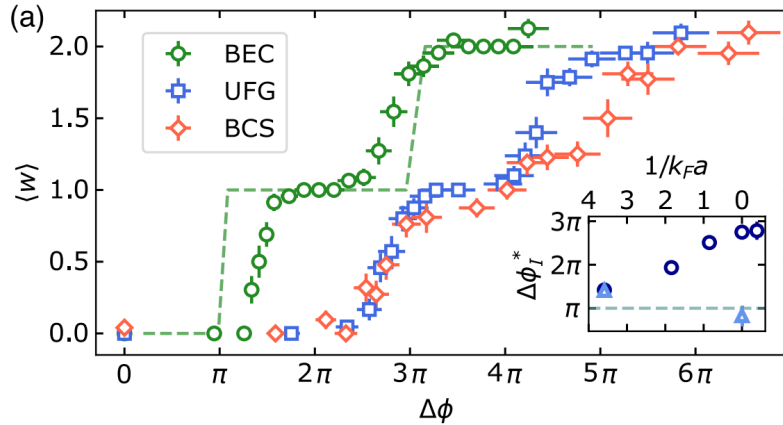


Figure 4.14: Measurement of the average winding number over 30 repetitions for different imprinted phases across the BEC-BCS crossover. Dashed line correspond to GPE simulations of the imprinting procedure. Image taken from [135].

To excite the persistent current states, we shine the intensity profile of Figure 4.12 for a short period of time Δt , and measure using the interferometric measurement we final state after 300 ms of holding time. We define the imprinted phase $\Delta\phi = \alpha\Delta I = \alpha(I^{0+} - I^{0-})$, with $I^{0\pm}$ characterizing the intensity jump at $\theta = 0$, and α a constant quantifying the height of the optical potential. We calibrate the value of α by measuring the equation of state of a partially condensed cloud in the BEC regime in a cigar shaped trap [157]. After determination of the intensity I coinciding with the chemical potential μ , we obtain the calibration constant from the equality $\mu = \alpha I$. A more detail analysis of it is given the supplementary material of Ref. [135].

As shown in Figure 4.14, the average winding number for different imprinted phases display the characteristic step-like behavior of the transition to distinct states with quantized winding number. Note that the behavior is similar in all superfluid

regimes, except of the initial shift of the transition to the $w = 1$. This behavior, is an artificial effect due to secondary excitations populated during the imprinting procedure. A more detail analysis of it is given Ref. [135, 152].

4.6 Counter-rotating superfluids: emergence of a vortex necklace

4.6.1 Concentric persistent currents

To realize a scenario where two superfluids are in counter-propagating motion and we have full control of the velocity state of each superfluid it is convenient to use persistent current states. As we have shown in the previous section, persistent states in annular superfluids offer a pristine control over the initial state of the system. The persistent states have a well define velocity profile $\vec{v} = \frac{\kappa}{2\pi} \frac{w}{r} \hat{\theta}$, that can be tuned experimentally by changing the winding number w . Moreover, the fidelity characterizing the initial preparation is well above 80%. Using the phase imprinting protocol, we are able to populate up to $w = 8$ for a the given inner radius of $10 \mu\text{m}$, and even higher numbers for larger inner radius [151]. For theses reasons we consider a system of two concentric annular superfluids, see Figure 4.15.

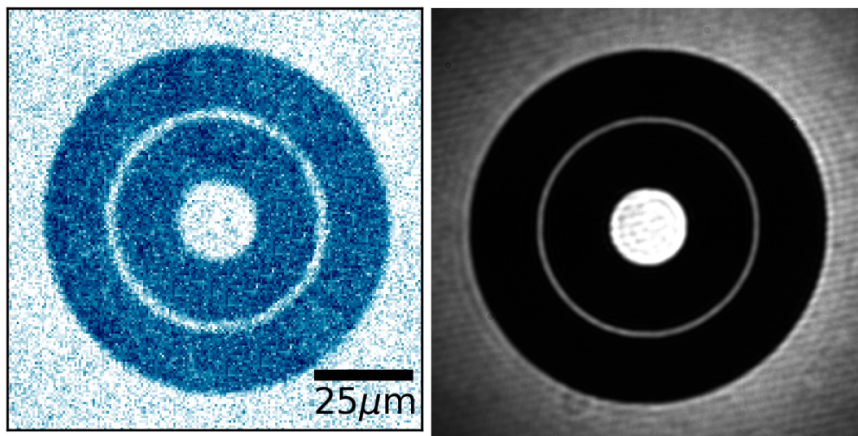


Figure 4.15: In situ image of the atomic cloud besides the optical potential designed with the DMD.

To realize the double ring potential using the DMD, we use the light pattern shown in Figure 4.15. The most internal radius has dimensions $R_{in} = 10\mu\text{m}$, the

most external $R_{out} = 45\mu m$, and the barrier is located in the middle of these two radius, $R_b = 27.5\mu m$, and is well described by a Gaussian shape with waist $\sigma = 1.1 \pm 0.1 \mu m$. We followed a similar protocol as shown in Figure 4.11 for reaching the final configuration of the potential, simply adding the additional step for creating the barrier separating the two ring regions. The separating barrier is set much higher than the chemical potential ($V_0 \approx 3\mu$), and allows for the preparation of independent persistent currents in each of the two rings superfluids, see Figure 4.15.

At this point of the procedure, we typically contain $3 \cdot 10^4$ atoms per spin component. The in-plane atomic density is $4.96(2)\mu^{-1}$ remaining constant for all the interaction regimes explored. The trapping frequency along the vertical direction have frequencies $\omega_z = 2\pi \times 400\text{Hz}$. For the BEC regime, the molecular scattering length is typically $a_M = 1010a_0$, where a_0 is Bohr radius, with the chemical potential is around $\mu/h \approx 900 \text{ Hz}$. For the fermionic superfluids, at unitarity and BCS, the corresponding energy scale is $E_F/h \approx 10 \text{ kHz}$.

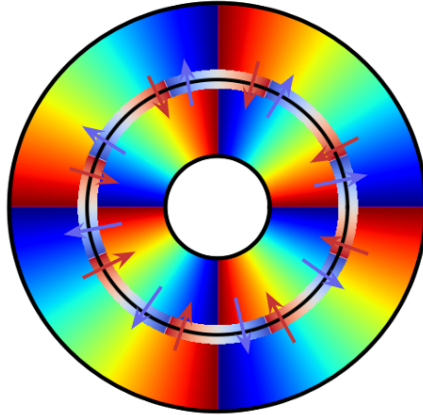


Figure 4.16: Phase profiles of the superfluids when $w_{in} = -w_{out} = 4$. The relative phase at the interface, $\Delta\phi = \phi_{in} - \phi_{out}$, is shown in blue-to-red colors. The abrupt change of sign suggest an abrupt change of flow (arrows) from inwards flow to outward flow, and vice versa.

To generate the DMD image used for the phase imprinting procedure, we selectively chose the corresponding gradient profile (see Figure 4.12) for the clockwise circulation of the inner ring and the anti-clockwise circulation of the outer ring. We projected the DMD pattern onto the atoms according to the calibration curve shown in Figure 4.14. Since we chose to project the pattern for the same duration in both ring superfluids, both will share the same absolute value of the winding number but in opposite directions, i.e., $w_{in} = -w_{out} = w$. For all the experiments performed in

the following sections, we start from a situation where $w = 0$ before the phase imprinting procedure. In this case, the time-of-flight imaging of the interference pattern between the two superfluids provides us with the relative winding number between both superfluid phases. An example of the phase profiles of the superfluids is shown in Figure 4.16 for the case where the winding number of each ring is $w = \pm 4$. The relative phase, $\Delta\phi = \phi_{\text{in}} - \phi_{\text{out}}$, changes sign $\Delta w = w_{\text{in}} - w_{\text{out}} = 8$ times along the azimuthal direction. The abrupt change of sign suggests an abrupt change of flow from inward flow to outward flow, and vice versa, at each of the $\Delta w = 8$ points.

4.6.2 Merging of concentric superfluids

While the superfluids remain independent of each other, the relative phase between them can only be accessed through interferometric measurements. However, reducing the height of the separating barrier allows the superfluids to merge. Depending on the speed at which we lower the separating barrier, different dynamics can occur.

Instantaneous merging dynamics

The merging dynamics of different superfluids is a very physics-rich problem. A clear example of these merging dynamics is the Kibble-Zurek mechanism [31, 158] that occurs when crossing the superfluid transition. During this transition, different superfluid patches form, each with a local phase. However, upon merging, the phases of the superfluid patches must be glued together in a continuous way. In most cases, this cannot be done properly, and the creation of phase singularities (vortices) is inevitable.

An even simpler system, where the merging dynamics are not straightforward, takes inspiration on the first experiments studying soliton creation [159, 160]. In cigar-shaped condensates with a separating barrier, solitons can be prepared by phase imprinting a constant phase difference between both reservoirs [161, 162]. After the imprinting, and removing the barrier, the system develops a soliton excitation. The fate of the created soliton strongly depends on the geometrical constraints imposed by the system. In 1D channels, the soliton is a stable solution and can propagate in the trap [163]. In 2D and 3D systems, the soliton is unstable and eventually decays. Depending on the geometry, the soliton can decay into 3D vortex rings [164] or into a series of vortex-antivortex pairs in 2D [165]. An interesting question that arises

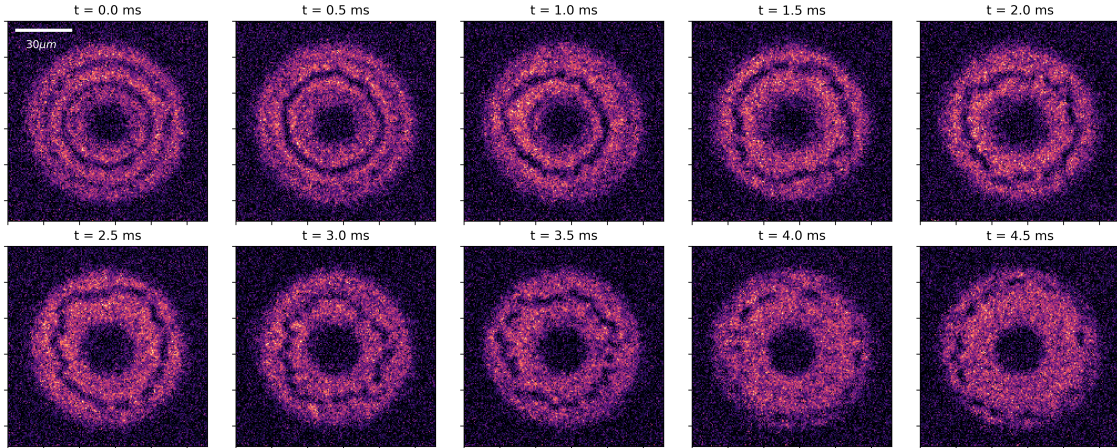


Figure 4.17: Decay of a ring soliton into quantum vortices in a BEC gas. We phase imprint a homogeneous phase $\Delta\phi = \pi$ in the outer ring, and remove the circular barrier instantaneously.

is which are the differences between the BEC, UFG, and BCS superfluids regarding the solitonic decay. In recent works [166–169], it was shown that, concerning the snake instability, the main difference lies in the most unstable wavelength at which the instability occurs.

As a starting point for studying the dynamics of merging our concentric ring superfluids, we first study the dynamics of a ring soliton in the BEC regime. We start by phase imprinting a homogeneous phase in the outer ring, $\Delta\phi = \pi$, and then removing the circular barrier instantaneously. Figure 4.17, shows the time evolution of the system after removing the barrier. Removing the barrier instantaneously, doesn't allow the phase of the global wavefunction to reach an *equilibrium* in a continuous way. At $t = 0$, we observe the interference pattern between both annular superfluids in time-of-flight. Starting with no persistent current ($w_{in} = w_{out} = 0$) the interference pattern is concentric. However, after few tens of milliseconds, the interference pattern disappears, and a higher contrast ring depletion appear. This depletion corresponds to a solitonic excitation which is not a stable configuration, and eventually decays through the well-known snake instability. The continuous soliton eventually vanishes, and a series of localized density depletion's, quantum vortices, appear. As time increase, the array of vortex-antivortex pairs get closer to the edge of the trap. The observed dynamics are well captured by numerical simulations based on the GPE, see Figure 4.18.

An even richer scenario occurs when trying to merge two persistent current states

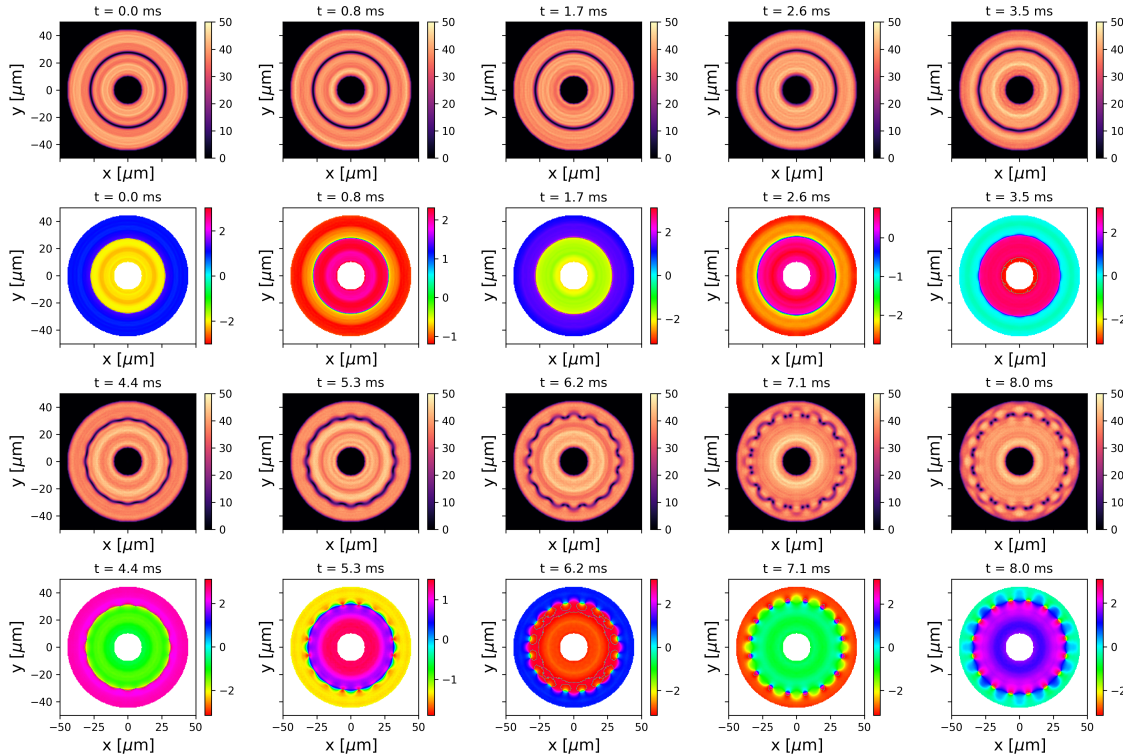


Figure 4.18: Decay of a ring soliton into quantum vortices. Density and phase profiles of the numerical solution of the GPE under similar conditions as Figure 4.17. At $t=0$, the outer ring has an homogeneous phase different $\Delta\phi = \pi$ with respect to the inner condensate. The phase profile confirm the presence of the vortex-antivortex pairs.

by instantaneous removing the barrier separating them. This kind of merging dynamics has been previously studied theoretically in BECs in the context of circular and annular geometries [159]. In this scenario, a spiral-like soliton excitation is created. The spiral soliton has a phase structure which along its extension the phase difference across the soliton varies from 0 to 2π . Following the phase analysis of Figure 4.16, we expect to have Δw of these excitations for our geometry and initial persistent states. To prove this regime, we performed numerical simulations of the GPE shown in Figure 4.19.

The behavior of the soliton is quite complex. Initially, as expected Δw spirals appear between both condensates. The spiral-soliton eventually decays when reaching the edges of the system. The complex dynamics nucleates and destroys vortices, filling the background of the condensate with sound waves and additional vortices. Interestingly, the Δw of spirals eventually lead to the formation of Δw vortices nearly

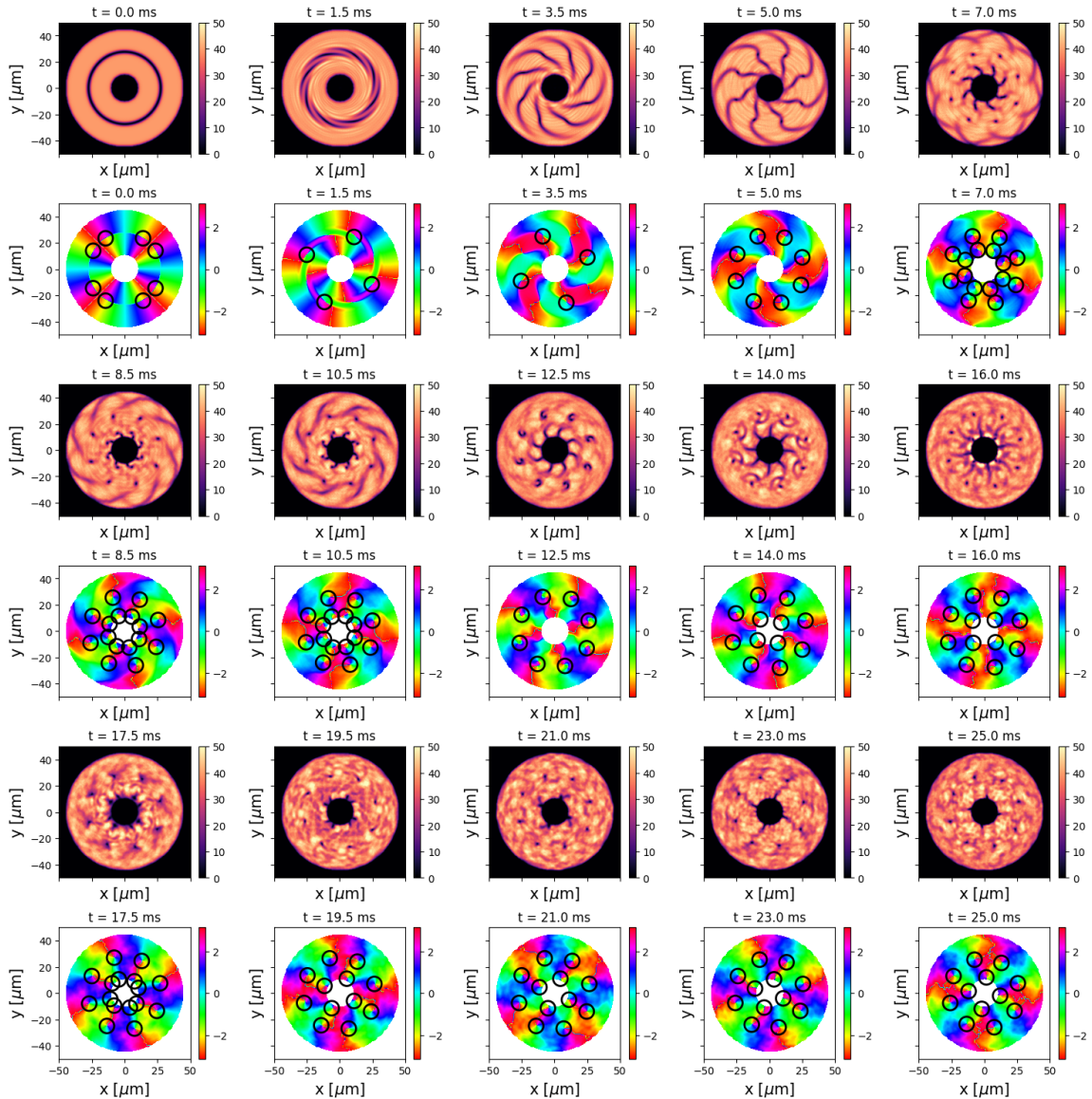


Figure 4.19: Decay of spiral solitons. Density and phase profiles of the numerical solution of the GPE under similar conditions as Figure 4.17. At $t=0$, each ring condensate is characterized by a persistent current with $w_{in} = -w_{out} = 4$.

located at the same positions where the spirals were nucleated.

Controlled merging dynamics

To minimize the uncontrolled creation of sound waves and vortices in the cloud, we consider a slower pace for the ramp down of the barrier. We consider time scales much longer than the characteristic chemical potential timescale \hbar/μ , in particular

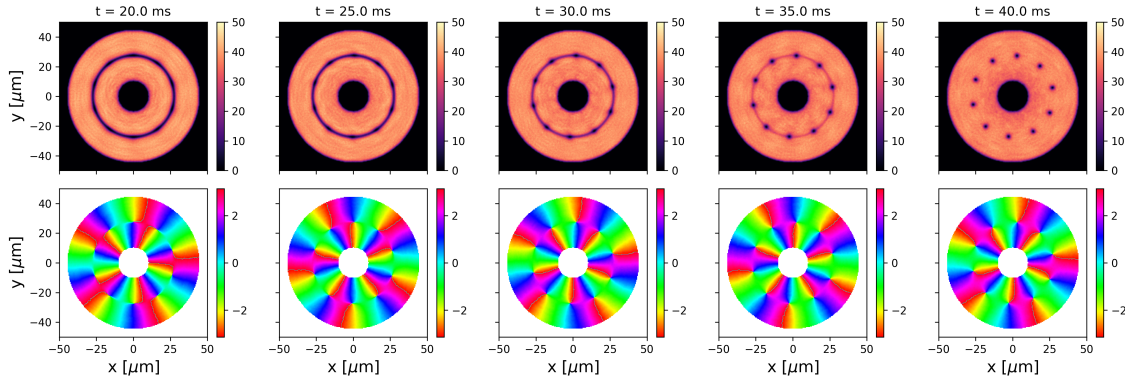


Figure 4.20: Dynamics of the density (top) and phase (bottom) over time, when the barrier is ramped down at a slow rate (28 ms).

we choose the total ramp time to be $28 \text{ ms} \gtrsim 20h/\mu$. To contrast the behavior of ramping speed, in Figure 4.19 and 4.20 I show the temporal evolution of the system. As clearly demonstrated, ramping down the barrier slowly doesn't introduce excitation such as sound waves or solitons into the system. Instead, the the system evolve smoothly between two independent annular superfluid with a barrier between them, to the scenario of a single condensate in presence of quantum vortices. The slow ramp speed allow for an adiabatic nucleation of vortices along the circular barrier. The circulation (or sign) around each vortex is the same, set by the outer superfluid rotation, forming a polygonal array of equal sign vortices [121, 122].

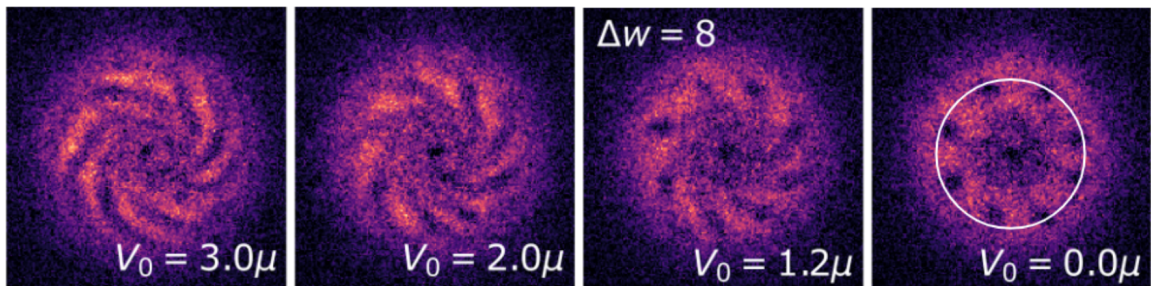


Figure 4.21: Time-of-flight images showing the interferogram between both annular superfluids during the barrier removal. When $V_0/\mu \gg 1$, we observe $\Delta w = 8$ spiral arms. When $V_0/\mu \lesssim 1$, the interference pattern disappears and rather the emergence of localized defects appear at the same radial position as the initial interface.

We probe this behavior in the experiment by performing a time-of-flight measurement during the barrier removal, see Figure 4.21. As long as the barrier is larger than the chemical potential ($V_0/\mu \gg 1$), the time-of-flight reveal the interference fringes

characteristic of two fully independent superfluids with persistent currents, see Figure 4.13. However, as the barrier height becomes comparable with the chemical potential, $V_0/\mu \sim 1$, we appreciate the superposition of the spiral behavior with the presence of point-like depletions in the density profile, signaling the formation of the quantum vortices. Finally, as the barrier is completely removed, we observe the time-of-flight density profile of a single superfluid together with the polygonal array of vortices.

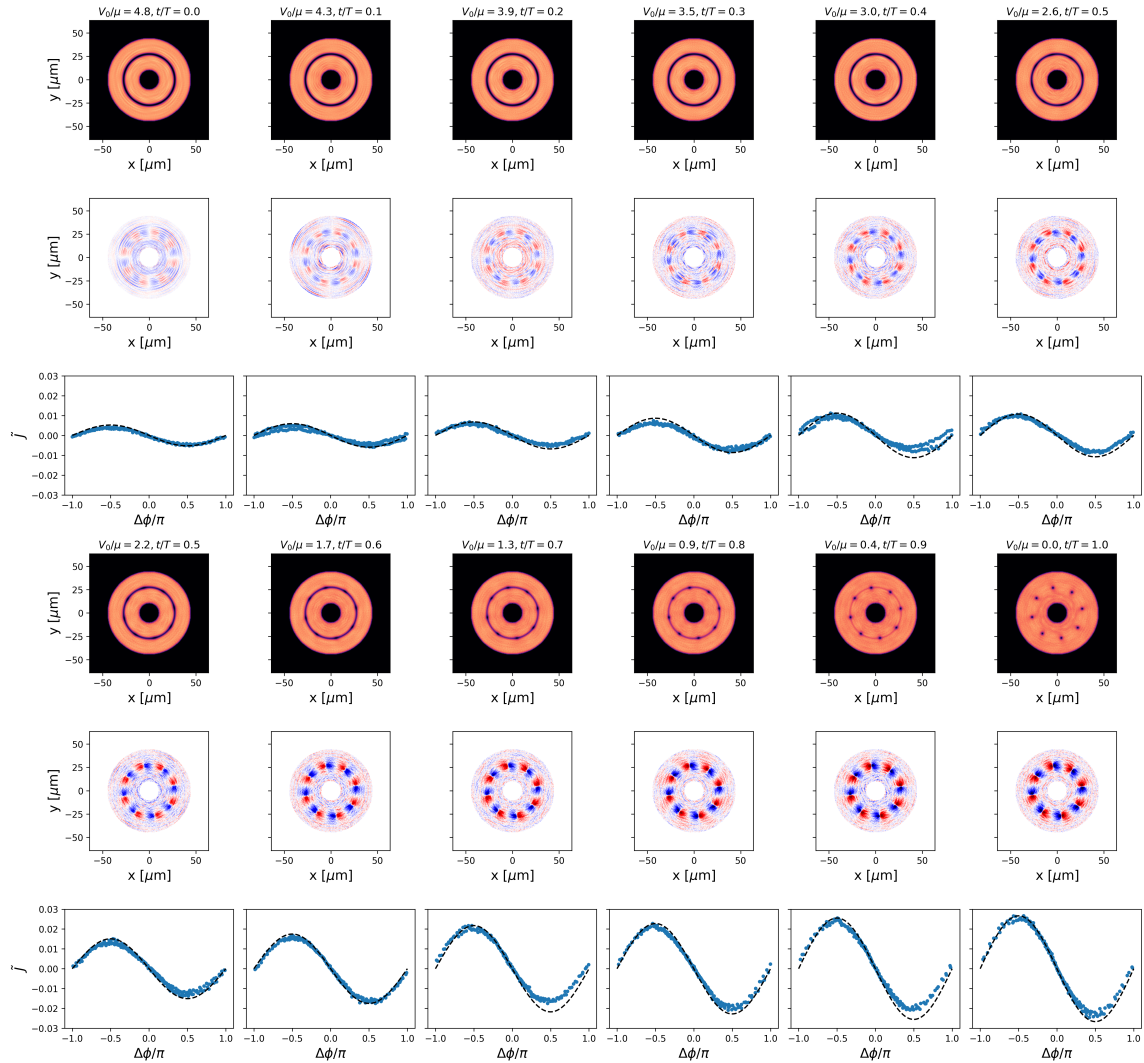


Figure 4.22: Dynamics of the density (top), radial mass current (middle), and current-phase relation (bottom) over time when the barrier is ramped down at a slow rate ($T = 28$ ms). In the current-phase relation plot, a sinusoidal fit describes the observed behavior. The color in the radial mass current indicate the direction of the flow: red is outwards, blue as inwards.

To understand the process of vortex formation, let turn to the behavior of the

currents in the system. In Figure 4.22, we show the behavior of the density, and the radial mass current. For convenience, we defined the normalized current as $\tilde{J} = |\mathbf{J}|/(n_0\kappa) = n|\mathbf{v}|/(n_0\kappa)$. It is interesting that even when the barrier is above the chemical potential, there exist a minuscule current passing through the barrier. The reason behind this can be understood in terms of atomic Josephson currents where the circular barrier acts as the Josephson junction. Instead of the junction being driven by a difference of chemical potential between the reservoirs, the current is driven by the difference of phase across the barrier. From the phase profile, Figure 4.16, we can have the intuitive direction of the Josephson currents that is corroborated in the middle panels of Figure 4.22, where the color indicates the direction of the flow. The symmetry of the observed currents suggests that no chemical potential built up is going to occur over time, contrary to linear Josephson Junctions [170–172]. Furthermore, as the barrier is lowered down the overlap between both reservoirs increases, hence the maximum current able to pass through the junction. To further highlight the analogy with atomic Josephson junctions, the current-phase relation of the junction is also shown in Figure 4.22. The maximum current of the Josephson junction clearly follows a sinusoidal relation of the form: $I = -I_{max} \sin \varphi$, where $\varphi(r) = \langle \phi(r) \rangle_{out} - \langle \phi(r) \rangle_{in}$, and the minus sign accounts for the direction of the flow.

The system composed of two concentric annular superfluids, offer then the possibility to study models such as the linear long Josephson junction with periodic boundary conditions. Here, the azimuthal direction, plays the role of periodic coordinate. From this perspective, the dynamics of the phase difference across the barrier can be described using a sine Gordon equation for the relative phase [170]. The sine-Gordon equation appears in a variety of physical systems and models, particularly where the nonlinear dynamics and phase transitions or topological defects are present. From topological defects in field theory, nonlinear optics, particle physics to the dynamics in long Josephson junctions [170]. In the sine Gordon equation, there exists well-known stable phase-profile solutions known as kink and anti-kink solitons. The phase profile they follow is given by:

$$\varphi(\theta) = 4 \arctan [\exp (\delta + \gamma m(x - vt))], \quad (4.14)$$

$$\frac{\partial^2 \varphi}{\partial t^2} - \frac{\partial^2 \varphi}{\partial x^2} + m^2 \sin \varphi = 0. \quad (4.15)$$

where m determines the nonlinear coupling, v the velocity of the kink solution

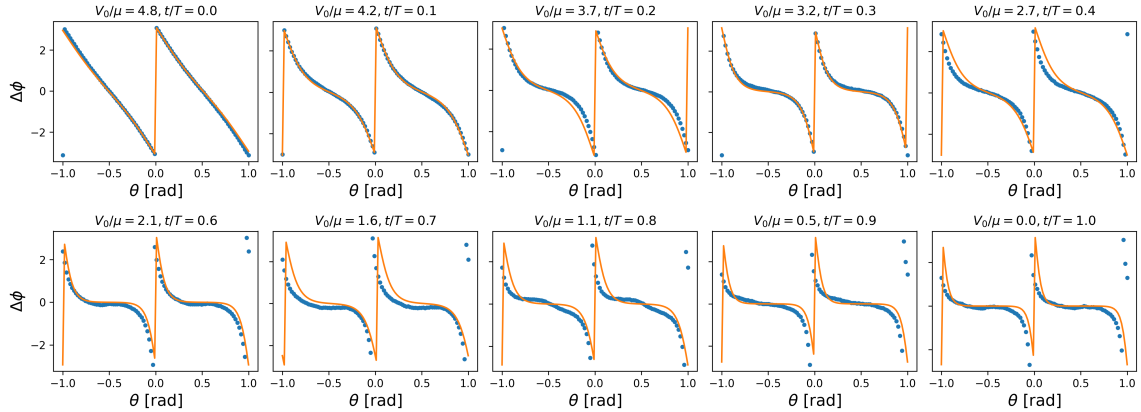


Figure 4.23: Phase difference across the barrier as a function of the angular direction, for the case with $\Delta w = 2$. Orange curve is the 2 kink-solitons solution of the sine-Gordon equation.

together with the associated Lorentz factor $\gamma = \frac{1}{\sqrt{1-v^2}}$. Interestingly, the phase difference profiles and the solution of the sine-Gordon equation resemble each other, see in Figure 4.23. In particular, in the regime where $V_0 > \mu$, the mapping to the Josephson junction is valid. In the context of superconducting linear Josephson junctions, the kink solution is typically associated to Josephson vortices [173], which are an active area of research especially for quantum computing. While in this thesis we don't study the particular mapping to the long Josephson junction in presence of Josephson vortices (since we remove the barrier completely), we make emphasis on the general application of ultra cold atoms as a platform for quantum simulation.

Controlling the vortex polygon array

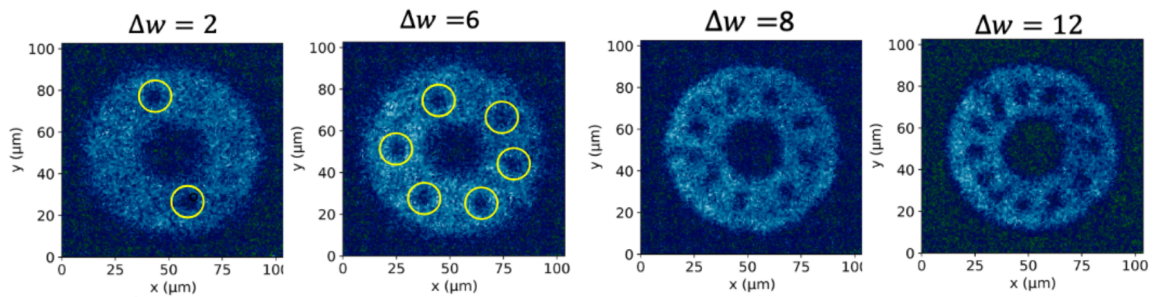


Figure 4.24: By engineering the persistent current states before the merging, we control the number of vortices in the vortex array. Examples of $\Delta w = 2, 6, 8,$ and 12 are provided.

The number of vortices appearing in the vortex polygon depends exclusively on the difference of winding number between both persistent currents, see Figure 4.24. The equality $N = \Delta w$ ideal holds. The final number of vortices can be therefore controlled meaning we can tune the difference of velocity at which the superfluids merge. The velocity difference at the interface is simply given by:

$$\Delta v = \frac{\hbar}{M} \frac{\Delta w}{R_0} = \frac{\hbar}{M} \frac{N}{R_0}. \quad (4.16)$$

However, imperfections in the phase imprinting protocol leading to the excitation of unwanted vortices in the system can occur [135]. Additionally, when the persistent currents decay, they do so by the emission of vortices out of the central region [135]. Moreover, as seen in Figure 4.19, speeding up the dynamics of the ramping down and generate more undesirable vortices, making the equality $N = \Delta w$ not to be experimentally trivial to achieve. In Ref. [135, 151], we found that letting the system relaxes for 100-300ms before removing the circular barrier reduces the amount of perturbations, and let off-barrier vortices leave the system leaving the superfluid background more uniform. Unfortunately, some spurious vortex can remain in the system even after such a long relaxation times. These, appear as density depletion out of the barrier region when stating the vortex dynamics as shown in Figure 4.25.

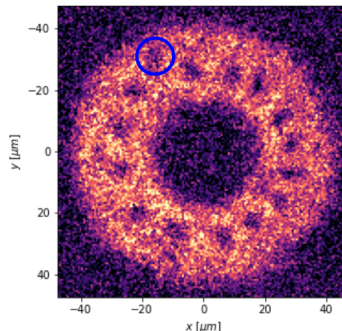


Figure 4.25: Image of a spurious vortex created as a consequence of an imperfect phase imprinting. The vortex lies away from the ideal vortex polygon.

We characterized the fidelity of the initial state preparation by repeating over 100 times the preparation of the states with $w_{in} = -w_{out} = w = 3$ and $w = 6$, as shown in Figure 4.26. The first panel characterizes the probability of observing the desired persistent states, before removing the barrier. We performed this measurement by looking at the interference pattern between the two rings superfluids, and counting the number of observed spirals. We clearly see that we are able to prepare the initial

circulation states $\Delta w_T = 2w$ with an error of ± 1 for 95% of the realizations.

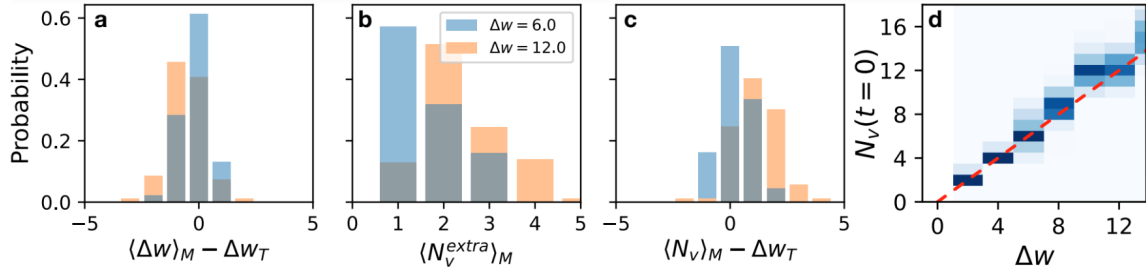


Figure 4.26: a) Infidelity in creating the target circulation state state, $\langle \Delta w \rangle_M - \Delta w_T$. b) Number of spurious vortices observed before removing the optical barrier, and c), Deviation of the total number of vortices from the target state, $\langle N_v \rangle_M - \Delta w_T$. d), Total number of vortices detected after removing the barrier, $t = 0$ of vortex dynamics, as a function of the imprinted winding number difference Δw_T .

In the second panel, we show the number of spurious vortices introduced by the phase-imprinting protocol, as measured from the time-of-flight (TOF) expansion of the two rings prior to the removal of the barrier. The third panel shows the distribution of the total number of vortices in the superfluid, detected in the TOF expansion following the barrier's removal. Although our method demonstrates a high reliability in producing the desired circulation states in the two rings, we observe that the total vortex distribution detected after barrier removal is both augmented and broadened due to the presence of spurious vortices. This phenomenon results in residual fluctuations in the initial configurations of the vortex polygon, which contributes to the experimental uncertainty in the initial relative velocity, denoted as Δv .

Chapter 5

Kelvin-Helmholtz Instability in atomic superfluids

In this chapter, I investigate the onset and evolution of the Kelvin-Helmholtz instability in fermionic superfluids across the BEC-BCS crossover. Starting from the ordered polygonal array of quantized vortices formed after the merging of two counter-rotating annular superfluids, I first describe the observed behavior following the formation of the vortex polygon, where the system can be characterized as a single superfluid. I discuss the method for tracking vortex positions and the reproducibility of these measurements.

Next, I address the linear stability analysis of the vortex polygon using the dissipative point-vortex model in the various geometrical arrangements outlined in Chapter 2. This analysis allows us to compute the growth rate of the instability's dispersion relation for vortex polygons. By numerically solving the dissipative point-vortex model, we gain insight into the instability, including factors contributing to the irreproducibility of measurements.

Finally, following the point-vortex modeling discussion, I examine the experimentally measured growth rates and their comparison to theoretical models.

5.1 Vortex array temporal evolution

5.1.1 Breaking of the vortex array

In the previous section, I discussed the possibility of deterministically create a perfect polygonal array for vortices as a result of the controlled merging between two counter-rotating superfluids. As we discussed in section 3.3.1, a linear array of vortices is always unstable with the characteristic wavevector $k^* = \pi/d_v$ being the most unstable mode in the system. The characteristic wavelength correspond to the one associated to the motion of nearby vortices moving towards each other with opposite orthogonal velocities. We expect the subsequent dynamics of the linear array will show pairing between nearby vortices [121, 122].

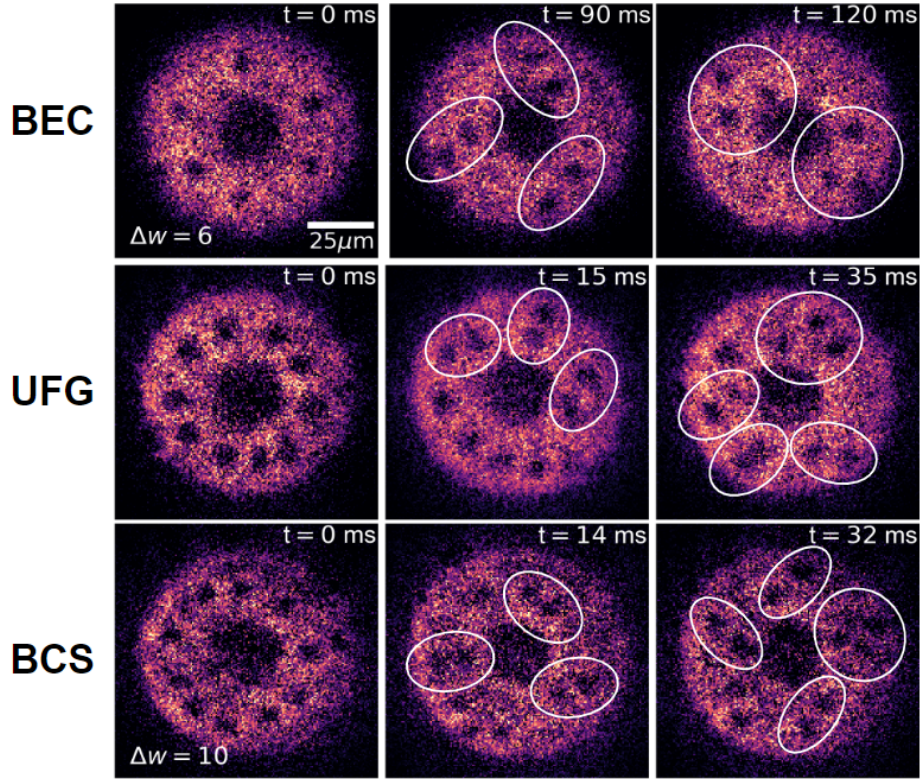


Figure 5.1: Temporal evolution of the vortex polygon for the BEC at $1/k_F a = 4.1$ with $N = 6$ vortices, UFG at $1/k_F a = 0$, and BCS at $1/k_F a = 0.3$ with $N = 10$ vortices.

As seen in Figure 5.1, the vortex polygon configuration is not stable. We observed the polygonal array breaking itself after a few tens of ms, depending in the interaction regime and number of vortices. Similarly to the linear vortex array, the

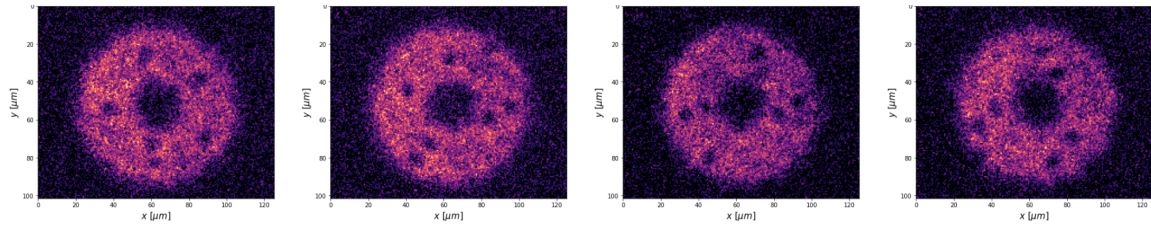


Figure 5.2: Temporal evolution of the vortex polygon for the BEC at $1/k_F a = 4.1$ with $N = 6$ vortices. We show different vortex configuration showing different forms of the breaking to occur.

polygonal array also tend to break with nearby vortices pairing together. Ideally, the paring should occur simultaneously in all the chain, corresponding to the process of spontaneous symmetry breaking. For small number of vortices, as we show in Figure 5.2, some experimental images show different ways the vortices can pair over all the polygon. However, for longer vortex chains the simultaneous breaking is less likely. Instead, the vortex array breaks locally, pairing nearby vortices in a small section of the polygon and spreading the pairing in the chain over time, as seen for $N = 10$ in the UFG and BCS regimes, and for $N = 6$ in in Figure 5.2. As we let the system evolve in time, we observe a clustering of vortices with increasing size. For $N = 6$, we see the presence of two large clusters with three vortices each, while for large number of vortices, clusters of different sizes appear, see Figure 5.1 and 5.3.

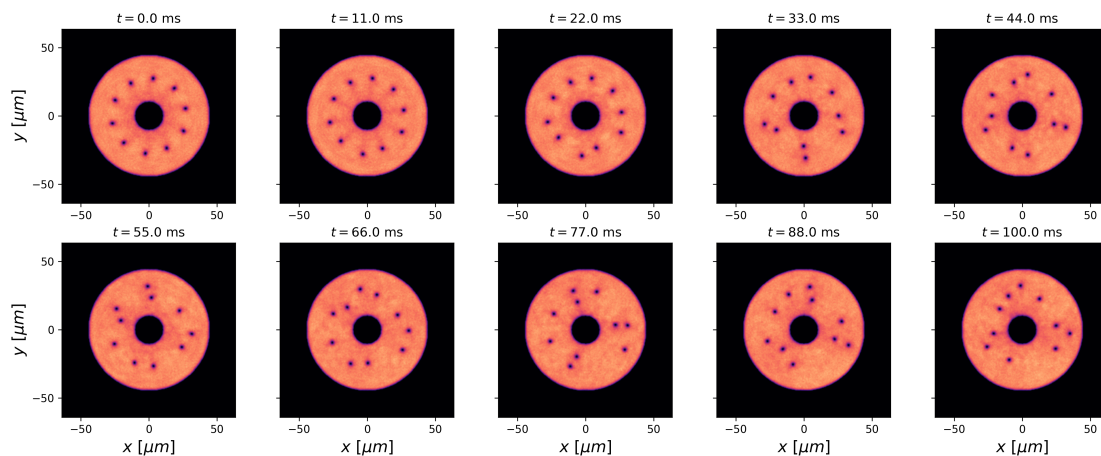


Figure 5.3: Temporal evolution from the GPE simulations for a system of $N = 10$ vortices.

To further corroborate the observed vortex dynamics agree qualitatively with theoretical models, I solve the GPE beyond the vortex polygon creation, as shown in

Figure 5.3. From the numerical results, we recover the local breaking of the vortex array due to small fluctuations in the system as pairing of nearby vortices starts in the lower section of the polygon.

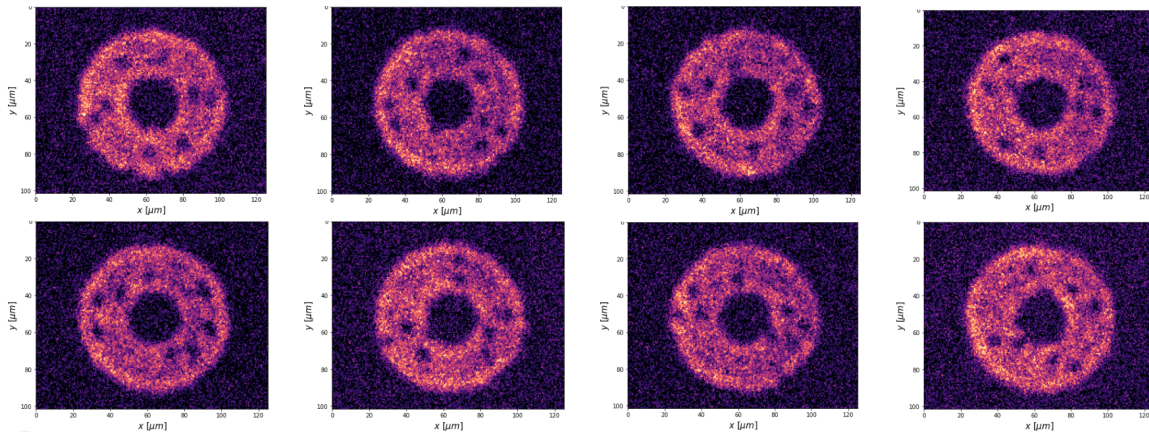


Figure 5.4: Temporal evolution of the vortex polygon for the BEC at $1/k_F a = 4.1$ with $N = 8$ vortices. We show different vortex configuration showing different forms of the breaking to occur.

In Figures 5.2 and 5.4, we can appreciate different realizations showing the different breaking configurations, where two nearby vortices can pair together. The different vortex configurations are originated from slightly different initial positions of the vortices when the barrier is completely removed. Which arise from small fluctuations in the system, either from imperfections of the phase imprinting protocol, reminiscent density waves in background, imperfections occurring during the removal of the optical barrier, etc... Due to the spontaneous symmetry breaking of the system, we should fine the correct tools for reconstructing the dynamics of the vortices from the extraction of single shot images as done in the experiment.

5.2 Linear Stability analysis of a vortex necklace

To understand the stability of the vortex polygon array and the subsequent expected growth rate, we need to perform a linear stability analysis around the array equilibrium position, similarly as was performed in section 3.3.1. We start by stating which is the stationary configuration, and which conditions must be fulfilled in order for the polygonal configuration to be unstable. The polygonal vortex array can be described by the following position in the complex mapping (see section 2.4.1):

$$z_a^0 = R_0 e^{2\pi i a/N} \quad (5.1)$$

with R_0 the radial positions of the vortices.

5.2.1 Stability of the vortices polygon inside a circular boundary

As a first example, let us recover let known results from Havelock [97] about the stability of the polygonal array inside a circular boundary. Let us start from the point vortex model equation with the correct boundary conditions:

$$\frac{dz_a^*}{dt} = \frac{\kappa_d}{2\pi i} \left(\sum_{b \neq a}^N \frac{1}{z_a - z_b} - \sum_{b=1}^N \frac{1}{z_a - \left(\frac{R^2}{|z_b|^2}\right) z_b} \right). \quad (5.2)$$

where $\kappa_d = \kappa(1 - \alpha' + i\alpha)$ is the complex circulation. Substituting the polygon starting solution of the form $z_a^0(t) = R_0 e^{i\omega t} e^{2\pi i a/N}$, with ω the given the temporal evolution of the solution. Substituting we get:

$$\frac{2\pi\omega^* R_0^2}{\kappa_d} = \sum_{b \neq a}^N \frac{1}{1 - e^{2\pi i(b-a)/N}} - \sum_{b=1}^N \frac{1}{1 - \left(\frac{R^2}{R_0^2}\right) e^{2\pi i(b-a)/N}}. \quad (5.3)$$

Both terms in the right hand side should be independent of the index a , therefore we can re-index the expression:

$$\frac{2\pi\omega^* R_0^2}{\kappa_d} = \sum_{\mu=1}^N \frac{1}{1 - e^{2\pi i\mu/N}} - \sum_{\mu=1}^N \frac{1}{1 - \left(\frac{R^2}{R_0^2}\right) e^{2\pi i\mu/N}}. \quad (5.4)$$

We can simplify the expression by considering the following equalities:

$$\sum_{\mu=1}^N \frac{1}{1 - e^{2\pi i\mu/N}} = \frac{N-1}{2}, \quad \text{and} \quad \sum_{\mu=1}^N \frac{1}{1 - A e^{2\pi i\mu/N}} = \frac{N}{1 - A^N}. \quad (5.5)$$

Therefore:

$$\omega = \frac{\kappa_d^*}{2\pi R_0^2} \left(\frac{N-1}{2} - \frac{N}{1 - \left(\frac{R^2}{R_0^2}\right)^N} \right) = (1 - \alpha' + i\alpha)\omega_0 = \Omega + i\gamma \quad (5.6)$$

In addition to an angular rotation Ω of the vortex polygon (which preserve the symmetry of the problem), when $\alpha \neq 0$ the polygon decrease size with a rate γ given by:

$$\Omega = \text{Im}[i\omega] = (1 - \alpha')\omega_0, \quad \gamma = -\text{Re}[i\omega] = \alpha\omega_0. \quad (5.7)$$

To study the stability around this trajectories, let us perturb the initial condition with a term of the form $z_a(t) = z_a^0(t)(1 + \eta_a(t))$, and let's define $\rho = (R/R_0)^2$. The equations for $\eta_a(t)$ are:

$$\left(\frac{d\eta_a^*}{dt} - i\omega^*\eta_a^* \right) z_a^{0*} = \frac{i\kappa_d}{2\pi} \left(\sum_{b \neq a}^N \frac{z_a^0 \eta_a - z_b^0 \eta_b}{(z_a^0 - z_b^0)^2} - \sum_{b=1}^N \frac{z_a^0 \eta_a - \rho z_b^0 \eta_b}{(z_a^0 - \rho z_b^0)^2} \right) \quad (5.8)$$

$$\frac{d\eta_a^*}{dt} - i\omega^*\eta_a^* = \frac{i\kappa_d}{2\pi R_0^2} z_a^0 \left(\sum_{b \neq a}^N \frac{z_a^0 \eta_a - z_b^0 \eta_b}{(z_a^0 - z_b^0)^2} - \sum_{b=1}^N \frac{z_a^0 \eta_a - \rho z_b^0 \eta_b}{(z_a^0 - \rho z_b^0)^2} \right) \quad (5.9)$$

$$\frac{d\eta_a^*}{dt} - i\omega^*\eta_a^* = \frac{i\kappa_d}{2\pi R_0^2} \left(\sum_{b \neq a}^N \frac{\eta_a - \frac{z_b^0}{z_a^0} \eta_b}{\left(1 - \frac{z_b^0}{z_a^0}\right)^2} - \sum_{b=1}^N \frac{\eta_a - \rho \frac{z_b^0}{z_a^0} \eta_b}{\left(1 - \rho \frac{z_b^0}{z_a^0}\right)^2} \right) \quad (5.10)$$

Defining $\tilde{t} = \frac{\kappa_d}{8\pi R_0^2} t$, $\tilde{\omega}^* = \frac{8\pi R_0^2}{\kappa_d} \omega^*$, and expressing the ratio $\frac{z_b^0}{z_a^0} = e^{2\pi i(b-a)/N}$ we get:

$$\frac{d\eta_a^*}{d\tilde{t}} - i\tilde{\omega}^*\eta_a^* = 4i \left(\sum_{b \neq a}^N \frac{\eta_a - e^{2\pi i(b-a)/N} \eta_b}{(1 - e^{2\pi i(b-a)/N})^2} - \sum_{b=1}^N \frac{\eta_a - \rho e^{2\pi i(b-a)/N} \eta_b}{(1 - \rho e^{2\pi i(b-a)/N})^2} \right) \quad (5.11)$$

This expression can the be written as

$$\frac{d\vec{\eta}^*}{d\tilde{t}} - i\tilde{\omega}^*\vec{\eta}^* = -i\mathbf{A}\vec{\eta} \quad (5.12)$$

where the vector $\vec{\eta}$ is an N-dimensional vector with entries $\vec{\eta} = (\vec{\eta}_a)$, and the matrix \mathbf{A} entries are defined as:

$$A_{ab} = -4\delta_{ab} \left[\sum_{\mu=1}^{N-1} (1 - e^{2\pi i \mu/N})^{-2} - (1 - \rho e^{2\pi i \mu/N})^{-2} \right] \\ + 4(1 - \delta_{ab}) \left(\frac{e^{2\pi i (b-a)/N}}{(1 - e^{2\pi i (b-a)/N})^2} \right) - 4 \frac{\rho e^{2\pi i (b-a)/N}}{(1 - \rho e^{2\pi i (b-a)/N})^2}$$

where δ_{ab} is the Kronecker delta. Considering $\vec{\eta} = \vec{\nu} + i\vec{\lambda}$, and $\tilde{\omega} = \tilde{\omega}_R + i\tilde{\omega}_I$, we obtain:

$$\frac{d}{d\tilde{t}} \begin{pmatrix} \vec{\nu} \\ \vec{\lambda} \end{pmatrix} = \begin{pmatrix} \tilde{\omega}_I \mathbf{1} - \text{Im}\mathbf{A} & \tilde{\omega}_R \mathbf{1} - \text{Re}\mathbf{A} \\ -\tilde{\omega}_R \mathbf{1} - \text{Im}\mathbf{A} & \tilde{\omega}_I \mathbf{1} + \text{Im}\mathbf{A} \end{pmatrix} \begin{pmatrix} \vec{\nu} \\ \vec{\lambda} \end{pmatrix} \quad (5.13)$$

Taking the second time derivative:

$$\frac{d^2}{d\tilde{t}^2} \begin{pmatrix} \vec{\nu} \\ \vec{\lambda} \end{pmatrix} = \begin{pmatrix} (\text{Re}\mathbf{A})^2 + (\tilde{\omega}_I \mathbf{1} - \text{Im}\mathbf{A})^2 - \tilde{\omega}_R^2 \mathbf{1} & 2\tilde{\omega}_I(\tilde{\omega}_R \mathbf{1} - \text{Re}\mathbf{A}) \\ -2\tilde{\omega}_I(\tilde{\omega}_R \mathbf{1} + \text{Re}\mathbf{A}) & (\text{Re}\mathbf{A})^2 + (\tilde{\omega}_I \mathbf{1} + \text{Im}\mathbf{A})^2 - \tilde{\omega}_R^2 \mathbf{1} \end{pmatrix} \begin{pmatrix} \vec{\nu} \\ \vec{\lambda} \end{pmatrix} \quad (5.14)$$

To solve for the different stability conditions for the different modes of the polygon, we write explicitly the temporal and spatial dependency of $\vec{\eta}$ as: $(\vec{\eta}_a) \sim e^{\tilde{\sigma}_m \tilde{t}} (e^{2\pi i \frac{ma}{N}})$, and we obtain:

$$\tilde{\sigma}_m^2 \begin{pmatrix} \vec{\nu} \\ \vec{\lambda} \end{pmatrix}_m = \begin{pmatrix} (\text{Re}\mathbf{A})^2 + (\tilde{\omega}_I \mathbf{1} - \text{Im}\mathbf{A})^2 - \tilde{\omega}_R^2 \mathbf{1} & 2\tilde{\omega}_I(\tilde{\omega}_R \mathbf{1} - \text{Re}\mathbf{A}) \\ -2\tilde{\omega}_I(\tilde{\omega}_R \mathbf{1} + \text{Re}\mathbf{A}) & (\text{Re}\mathbf{A})^2 + (\tilde{\omega}_I \mathbf{1} + \text{Im}\mathbf{A})^2 - \tilde{\omega}_R^2 \mathbf{1} \end{pmatrix} \begin{pmatrix} \vec{\nu} \\ \vec{\lambda} \end{pmatrix}_m \quad (5.15)$$

$$\tilde{\sigma}_m^2 = \left[|\mathbf{A}|^2 + (\tilde{\omega}_I^2 - \tilde{\omega}_R^2) \mathbf{1} \pm 2\tilde{\omega}_I \sqrt{|\mathbf{A}|^2 - \tilde{\omega}_R^2} \mathbf{1} \right]_m \quad (5.16)$$

where the subscript m denotes the evaluation the matrix A applied to the vector $(\vec{\eta}_a) \sim (e^{2\pi i \frac{ma}{N}})$, following the operation:

$$[\hat{O}]_m = (e^{-2\pi i \frac{ma}{N}})^T \hat{O} (e^{2\pi i \frac{ma}{N}}) \quad (5.17)$$

The previous derivation allows us to get the growth rate of the (un)stable modes with angular wavenumber m . Fortunately, for dissipationless dynamics where $\alpha = 0$ this results simplifies dramatically:

$$\tilde{\omega} = \frac{8\pi R_0^2 \omega_0}{\kappa} = 4 \left(\frac{N-1}{2} - \frac{N}{1-\rho^N} \right) \quad (5.18)$$

$$\tilde{\sigma}_m^2 = [|\mathbf{A}|^2]_m - \tilde{\omega}^2 \quad (5.19)$$

To obtain the growth rate $\sigma_m = \frac{\kappa(1-\alpha')}{8\pi R_0^2} \tilde{\sigma}_m$ of each angular mode, we require to solve numerically the above equation. As shown in Figure 5.5, in the limit $N \rightarrow \infty$, or equivalently $d_v \rightarrow 0$, the curvature of the polygonal array locally vanishes, and we recover the result of the linear array of vortices studied in section 3.3.1, which is given by Eq. (3.30).

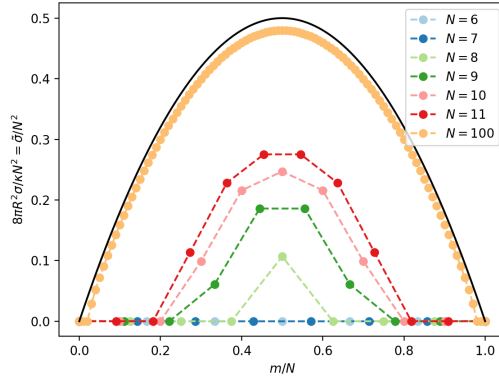


Figure 5.5: Growth rate of the unstable modes with periodicity m for different number of vortices. The black curve correspond to the linear array result Eq. (3.30).

5.2.2 Stability of the vortices polygon outside a circular boundary

Following the ideas presented so far, let us continue the analysis with the scenario of the vortices polygon outside an inner circular boundary. The equation of motion of the vortices is given by:

$$\frac{dz_a^*}{dt} = \frac{\kappa_d}{2\pi i} \left(\sum_{b \neq a}^N \frac{1}{z_a - z_b} - \sum_{b=1}^N \frac{1}{z_a - \left(\frac{R^2}{|z_b|^2} \right) z_b} \right) + \frac{\kappa_d}{2\pi i} \frac{\Lambda + N}{z_a}. \quad (5.20)$$

where we recall Λ is circulation of the internal ring superfluid, or equivalently the number of vortices located at the origin. Substituting the polygon solution of the form $z_a^0(t) = R_0 e^{i\omega t} e^{2\pi i a/N}$, we get temporal factor:

$$\omega = \frac{\kappa_d^*}{2\pi R_0^2} \left(\frac{N-1}{2} - \frac{N}{1 - \left(\frac{R^2}{R_0^2}\right)^N} + (\Lambda + N) \right) = (1 - \alpha' + i\alpha)\omega_0 = \Omega + i\gamma \quad (5.21)$$

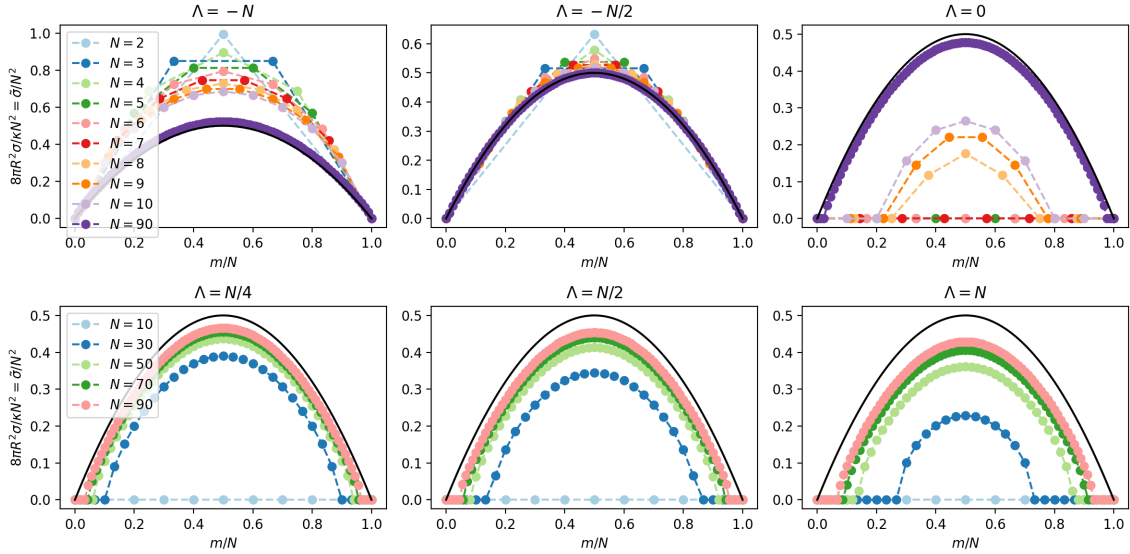


Figure 5.6: Growth rate of the unstable modes with periodicity m for different number of vortices, different topological charges enclosed in the inner region. The black curve correspond to the linear array result Eq. (3.30).

The growth rate remains defined in the same manner:

$$\tilde{\sigma}_m^2 = \left[|\mathbf{A}|^2 + (\tilde{\omega}_I^2 - \tilde{\omega}_R^2)\mathbf{1} \pm 2\tilde{\omega}_I \sqrt{|\mathbf{A}|^2 - \tilde{\omega}_R^2\mathbf{1}} \right]_m \quad (5.22)$$

where we set $\rho = (R/R_0)^2$, the matrix \mathbf{A} is defined as:

$$A_{ab} = -4\delta_{ab} \left[\Lambda + N + \sum_{\mu=1}^{N-1} \left((1 - e^{2\pi i \mu/N})^{-2} - (1 - \rho e^{2\pi i \mu/N})^{-2} \right) \right] \\ + 4(1 - \delta_{ab}) \left(\frac{e^{2\pi i(b-a)/N}}{(1 - e^{2\pi i(b-a)/N})^2} \right) - 4 \frac{\rho e^{2\pi i(b-a)/N}}{(1 - \rho e^{2\pi i(b-a)/N})^2}$$

Similarly to the previous scenario, Figure 5.6 shows the growth rate $\sigma_m = \frac{\kappa(1-\alpha')}{8\pi R_0^2} \tilde{\sigma}_m$ obtained from the numerical solution setting $\alpha = 0$, and for different values of Λ .

As shown in Figure 5.6, increasing values of Λ stabilize the vortex polygons, requiring higher number of vortices for the system to be unstable. On the contrary, when $\Lambda < 0$ we appreciate the system becoming unstable for any number of vortices $N > 2$. Moreover, regardless of the specific value of Λ , in the limit $N \rightarrow \infty$, we recover the result of the linear array of vortices given by Eq. (3.30).

5.2.3 Vortices inside an annular boundary

Taking the previous examples for vortices in either an outer or inner boundary, we can tackle the problem of the vortices in the annular geometry we have in the experiment. To start, let us consider the scenario with Λ arbitrary, and then we'll replace and analyze the behavior for the experimental configuration with where we set $\Lambda = -N/2$.

We start by recalling the point vortex model equation considering this set of boundary conditions:

$$\frac{dz_a^*}{dt} = \frac{\kappa_d}{2\pi i} \frac{\Lambda + N}{z_a} + \frac{\kappa_d}{2\pi i} \left[\sum_{b \neq a}^N \frac{1}{z_a - z_b} \right. \\ \left. - \sum_{b=1}^N \left(\frac{1}{z_a - \left(\frac{R_i^2}{|z_b|^2} \right) z_b} + \frac{1}{z_a - \left(\frac{R_o^2}{|z_b|^2} \right) z_b} \right) \right] \\ + \frac{\kappa_d}{2\pi i} \left[\sum_{b=1}^N \sum_{n=1}^{\infty} \left(\frac{1}{z_a - \left(\frac{R_i}{R_o} \right)^{2n} z_b} + \frac{1}{z_a - \left(\frac{R_o}{R_i} \right)^{2n} z_b} \right) \right. \\ \left. - \sum_{b=1}^N \sum_{n=1}^{\infty} \left(\frac{1}{z_a - \left(\frac{R_i}{R_o} \right)^{2n} \left(\frac{R_i^2}{|z_b|^2} \right) z_b} + \frac{1}{z_a - \left(\frac{R_o}{R_i} \right)^{2n} \left(\frac{R_o^2}{|z_b|^2} \right) z_b} \right) \right]$$

Substituting the polygon solution of the form $z_a^0(t) = R_0 e^{i\omega t} e^{2\pi i a/N}$, and defining $\rho = (R_i/R_o)^2$, $\rho_i = R_i^2/R_o^2$, and $\rho_o = R_o^2/R_o^2$, we get temporal factor:

$$\omega = \frac{\kappa_d^*}{2\pi R_0^2} \left[\frac{N-1}{2} - \frac{N}{1-\rho_i^N} - \frac{N}{1-\rho_o^N} + (\Lambda + N) \right] \quad (5.23)$$

$$+ N \sum_{n=1}^{\infty} \left(\frac{1}{1-\rho^{nN}} - \frac{1}{1-\rho_i^N \rho^{nN}} + \frac{1}{1-\rho^{-nN}} - \frac{1}{1-\rho_o^N \rho^{-nN}} \right) \quad (5.24)$$

Where we recognize the terms of the first two scenarios, and the contribution of the infinite number of vortices. The convergence of the infinite sum is exponentially fast with increasing number of terms, see Figure 5.7 for the comparison between the first 16 terms. For the experimental values of the inner and outer radii we see that taking 0 terms in the expansion approximates the real value with 10^{-14} precision. Since the imaginary vortices are already very far from the polygon radii. On the contrary when considering very thin rings, the addition of 16 terms from the imaginary vortices are necessary to reach the same level of convergence.

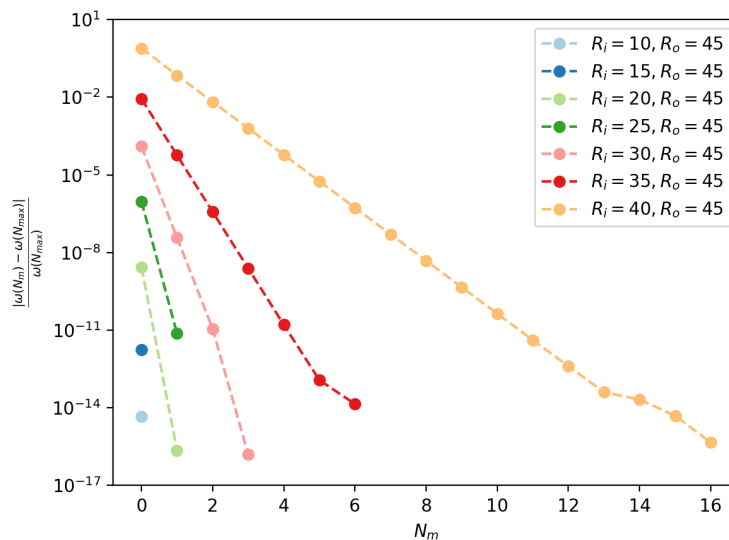


Figure 5.7: Calculation of the angular frequency of Eq. (5.23), using $R_0 = (R_i + R_o)/2$, as would be for the experimental ratios, and where $\alpha = \alpha' = 0$ for simplicity.

In this case, the matrix \mathbf{A} can be decomposed as:

$$\mathbf{A} = \mathbf{A}_0 + \sum_{n=1}^{\infty} \mathbf{B}_n, \quad (5.25)$$

with

$$\begin{aligned} \mathbf{A}_{0ab} &= -4(S_1 + (\Lambda + N) - S_2 - S_3) \delta_{ab} + 4(1 - \delta_{ab}) \frac{e^{2\pi i(b-a)/N}}{(1 - e^{2\pi i(b-a)/N})^2} \\ &\quad - 4 \frac{\rho_o e^{2\pi i(b-a)/N}}{(1 - \rho_o e^{2\pi i(b-a)/N})^2} - 4 \frac{\rho_i e^{2\pi i(b-a)/N}}{(1 - \rho_i e^{2\pi i(b-a)/N})^2}, \\ B_{nab} &= 4 \left(\frac{\rho^n e^{2\pi i(b-a)/N}}{(1 - \rho^n e^{2\pi i(b-a)/N})^2} + \frac{\rho^{-n} e^{2\pi i(b-a)/N}}{(1 - \rho^{-n} e^{2\pi i(b-a)/N})^2} \right. \\ &\quad \left. - \frac{\rho_i \rho^n e^{2\pi i(b-a)/N}}{(1 - \rho_i \rho^n e^{2\pi i(b-a)/N})^2} - \frac{\rho_o \rho^{-n} e^{2\pi i(b-a)/N}}{(1 - \rho_o \rho^{-n} e^{2\pi i(b-a)/N})^2} \right) \end{aligned}$$

where we defined for convenience the sums:

$$S_1 = \sum_{\gamma=1}^{N-1} \frac{1}{(1 - e^{2\pi i\gamma/N})^2}, \quad S_2 = \sum_{\gamma=1}^N \frac{1}{(1 - \rho_i e^{2\pi i\gamma/N})^2}, \quad S_3 = \sum_{\gamma=1}^N \frac{1}{(1 - \rho_o e^{2\pi i\gamma/N})^2}$$

The growth rate remains defined in the same manner:

$$\tilde{\sigma}_m^2 = \left[|\mathbf{A}|^2 + (\tilde{\omega}_I^2 - \tilde{\omega}_R^2) \mathbf{1} \pm 2\tilde{\omega}_I \sqrt{|\mathbf{A}|^2 - \tilde{\omega}_R^2 \mathbf{1}} \right]_m \quad (5.26)$$

Similarly to the previous scenarios, Figure 5.8 shows the growth rate $\sigma_m = \frac{\kappa(1-\alpha')}{8\pi R_0^2} \tilde{\sigma}_m$ obtained from the numerical solution setting $\alpha = 0$, and for different values of Λ .

5.2.4 Finite α correction

As we obtained from the previous sections, when no dissipation is present, that is when $\alpha = 0$, the growth rates can be easily computed by:

$$\sigma_m = \frac{\kappa(1-\alpha')}{8\pi R_0^2} \sqrt{[|\mathbf{A}|^2]_m - \tilde{\omega}^2} \quad (5.27)$$

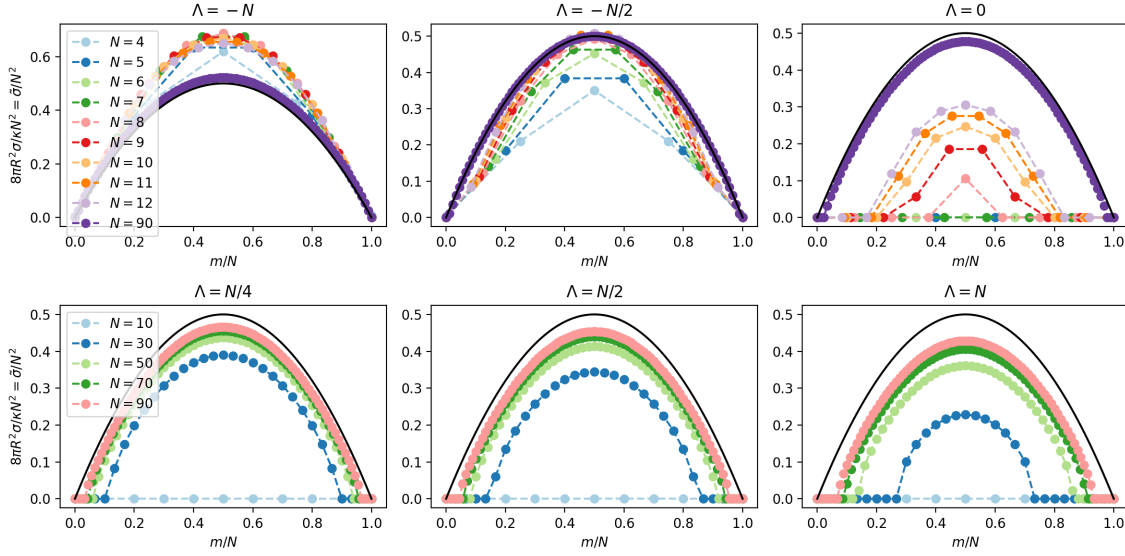


Figure 5.8: Growth rate of the unstable modes with periodicity m for different number of vortices, different topological charges enclosed in the inner region. The black curve correspond to the linear array result Eq. (3.30).

However, when $\alpha \neq 0$ we can still obtain an approximate solution. For these, let us consider the limit, when $N \rightarrow \infty$. In this case, we know we always return to the linear array limit discussed in section 3.3.1. The growth rate, with $\alpha = \alpha' = 0$, is given by:

$$\sigma = \frac{\kappa|k|}{2d_v} \left(1 - \frac{|k|d_v}{2\pi} \right). \quad (5.28)$$

We can extend the analysis conducted in Section 3.3.1 to the case where $\alpha, \alpha' \neq 0$. By substituting κ with κ_d , we achieve the same result, with $|\kappa_d|$ replacing κ :

$$\sigma_d = \frac{|\kappa_d||k|}{2d_v} \left(1 - \frac{|k|d_v}{2\pi} \right) = \sqrt{(1 - \alpha')^2 + \alpha^2} \sigma_0. \quad (5.29)$$

Due to the small second order correction of α to the growth rate, we find

$$\sigma_m = \frac{\kappa \sqrt{(1 - \alpha')^2 + \alpha^2}}{8\pi R_0^2} \sqrt{[|\mathbf{A}|^2]_m - \tilde{\omega}^2} = \sqrt{(1 - \alpha')^2 + \alpha^2} \sigma_m^0 \quad (5.30)$$

represents a good approximation to the real result for values of $\alpha \ll 1$, which is the limit we typically encounter in the experiments.

5.3 Vortex ensemble trajectories

5.3.1 Deterministic of trajectories

Although the equation of motion of the vortices is deterministic, in the sense that an equation of motion describing their dynamics can be properly defined, the temporal evolution of these vortices may still exhibit highly sensitive dependence on the initial conditions. This sensitivity is one of the hallmarks of chaotic systems, where even infinitesimal differences in starting points can lead to exponentially diverging trajectories over time, see Figure 5.9a. One way to characterize the rate of divergence of the trajectories is through the concept of Lyapunov exponent [174]. This exponent describes the average rate at which nearby trajectories in phase space diverge over time. Quantitatively, if $\mathbf{Z}(t)$ represents an ensemble of trajectories in phase space, the Lyapunov exponent λ is therefore defined as:

$$|\delta\mathbf{Z}(t)| = e^{\lambda t} |\delta\mathbf{Z}_0|. \quad (5.31)$$

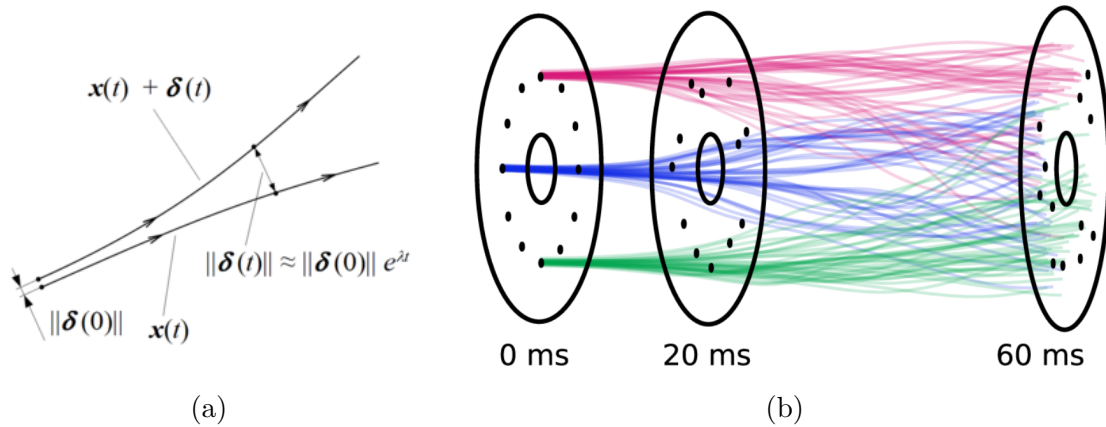


Figure 5.9: a) Method for determining the divergence exponent of a given ensemble of trajectories starting from similar initial conditions. b) Ensemble of trajectories obtained from 40 different simulations using the point vortex model.

A positive Lyapunov exponent indicates that trajectories initially close together will separate exponentially, illustrating why predicting long-term behavior in these systems becomes practically impossible after an initial period. On the contrary, a negative or zero exponent suggests stable or periodic dynamics where trajectories converge or remain at a constant distance. Depending on the phase space explored by

\mathbf{Z}_0 , different Lyapunov exponents can exist [174]. In fact, for our vortex system there are $2N$ degrees of freedom (two for each vortex), and hence $2N$ different Lyapunov exponents, with the largest one is known as the maximal Lyapunov exponent. It is worth noting that having a positive maximal Lyapunov exponent is usually an indication that the system is chaotic, however, other requirements must be fulfilled to assert the system displays chaotic behavior. Although, we'll see that the dynamics we probe seem to be chaotic, I don't provide the sufficient evidence for it.

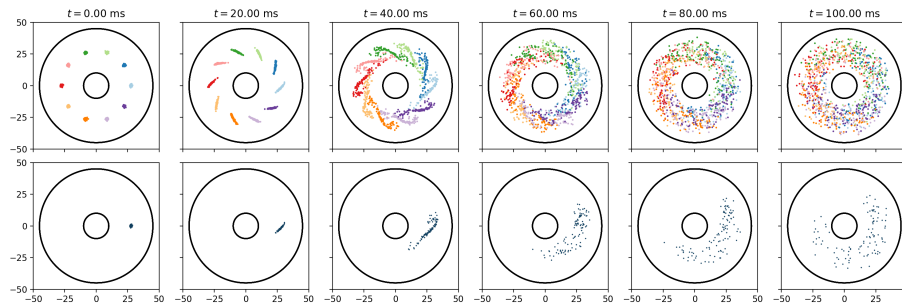


Figure 5.10: Temporal evolution of a system with 10 vortices, 100 simulations under slightly different initial conditions. First and second row: each vortex ensemble is colored differently. Third and Fourth rows: We focus on the dynamics of a vortex single ensemble. The area corresponds to the best concave area describing the ensemble.

Due to the symmetry of our system, we can provide three contrastingly different, but illustrative examples of ensembles $\mathbf{Z}(t)$ which produce a Lyapunov exponents either positive or null. To show the richness of ensemble of trajectories we solved numerically the point vortex model using a Runge-Kutta of 4th order for different ensembles $\mathbf{Z}(t)$ in the different degrees of freedom in the system.

The first case I consider is the one, most probable to be representative of the experimental protocol. Here, I took the position of the vortices to be close to the ideal ones $z_j = R_0 e^{2\pi i j/N} + \eta$ where $\eta = \xi + i\zeta$ are two gaussian random numbers with standard deviation given by the healing length of the vortices in the BEC regime, that is $\Delta\xi = \Delta\zeta = 0.5\mu m$. I considered an ensemble of 100 random initial positions which are then evolved numerically in time. The results are shown in the first two rows of Figure 5.10. On the first row, single vortex ensembles are colored differently so we can track their dynamics over time. On the first row, I isolate the dynamics of a single vortex ensemble. We can appreciate for short timescales, the vortices spread in a line and very fast, after 60 ms, the shape of the ensemble no longer keep a defined

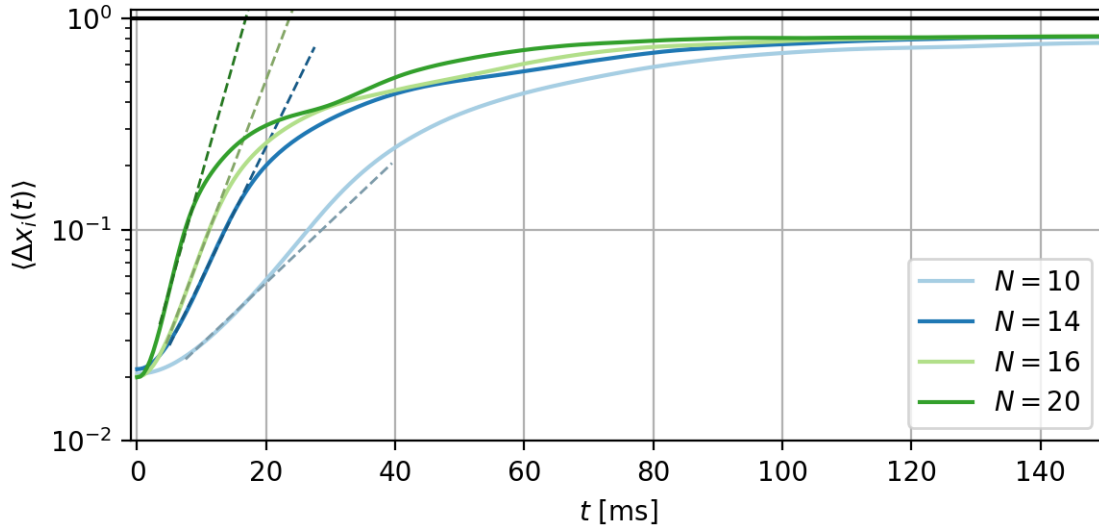


Figure 5.11: Measurement of the average distance between the point vortices in the ensemble for different number of vortices in the system.

shape.

Simulating this type of ensembles and changing the number of vortices we can estimate the rate of divergence of the single-vortex ensemble computing $|\delta\mathbf{Z}(t)|$. In Figure 5.11, we compare the results for different number of vortices from $N=10$ to $N=20$. As shown, the behavior of $|\delta\mathbf{Z}(t)|$ grows exponentially in time at the beginning of the dynamics, saturating for longer timescales to the average distance between two points in the annulus. It is important to note, that by probing using gaussian noise in all the vortices, we are effectively probing all the phase space nearby the ideal stationary point where $z_j = R_0 e^{2\pi i j/N}$. Therefore, the rate λ provides us information about the maximal Lyapunov exponent, which in each case corresponds to the one expected from the analysis performed in the previous section, which is given by Eq. (5.26). Moreover, depending on the number of vortices in the system, the final phase space explored by the system is different. The dynamics for $N = 2$ (Figure 5.12) and $N = 4$ (Figure 5.13) vortices.

A second example of ensemble where the Lyapunov exponent is null is shown in Figure 5.14. The simulation parameters are identical to those of Figure 5.10, with the only difference being the phase space explored by the different realizations. As we show in the previous section, the polygon is a stable configuration which rotate in time. Therefore selecting the axis in phase-space along which the polygon appears

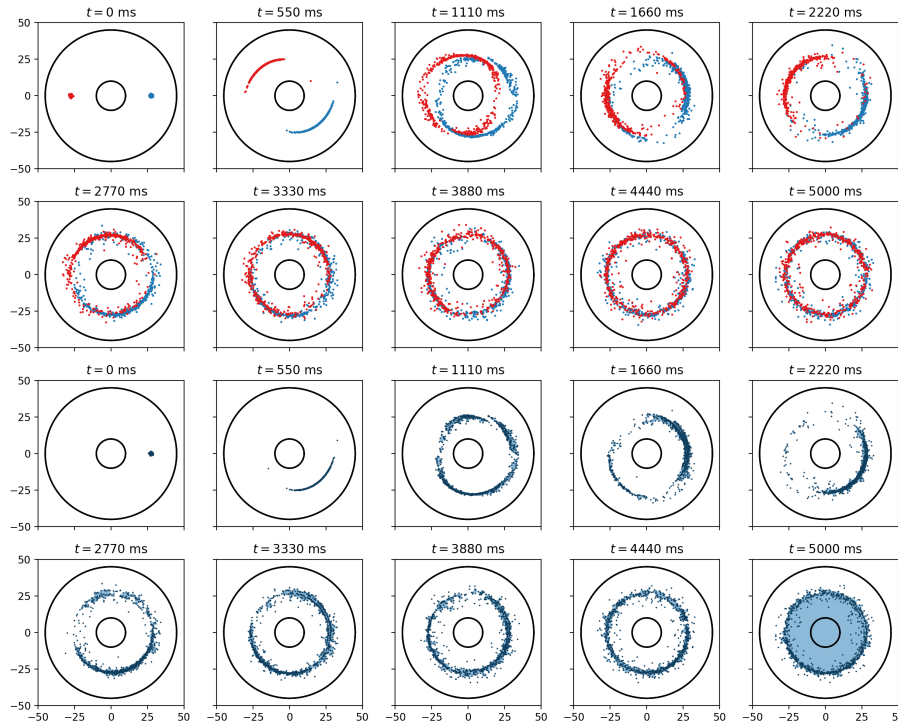


Figure 5.12: Temporal evolution of a system with 2 vortices, 500 simulations under slightly different initial conditions. First and second row: each vortex ensemble is colored differently. Third and Fourth rows: We focus on the dynamics of a vortex single ensemble. The area corresponds to the best concave area describing the ensemble.

slightly rotated, that is $z_j = R_0 e^{2\pi i j/N} \times \hat{\eta}$, with $\hat{\eta} = e^{i\xi}$ with a single gaussian random number with standard deviation given by the angular extent of the healing length, $\Delta\xi = 2\pi \times 0.5/27.5$ rad. As seen in Figure 5.14, the initial spread of the ensemble $|\delta\mathbf{Z}_0|$ is kept constant in time, the trajectories rotate lock in phase between them.

A third example of ensemble where the Lyapunov exponent is positive but the dynamics can be clearly distinguished is shown in Figure 5.15. In this scenario we considered a region of phase space where vortices preserve their relative angle $\Delta\theta_{j,j+1} = \frac{2\pi}{N}$, but they alternate radial positions, of the form: $z_j = R_0 e^{2\pi i j/N} \times \hat{\eta}_j$, with $\hat{\eta}_j = 1 + (-1)^j \xi$ with a single gaussian random number in each numerical experiment, where the standard deviation is given by $\Delta\xi = \sqrt{2} \times 0.5 \mu m$. In this scenario, the trajectories seem to follow a clear star shape around the central region, for a long period of time without spreading to much. However, after a close look at the dynamics nearby the ideal position reveal a deeper structure, as shown in Figure 5.16. For initial

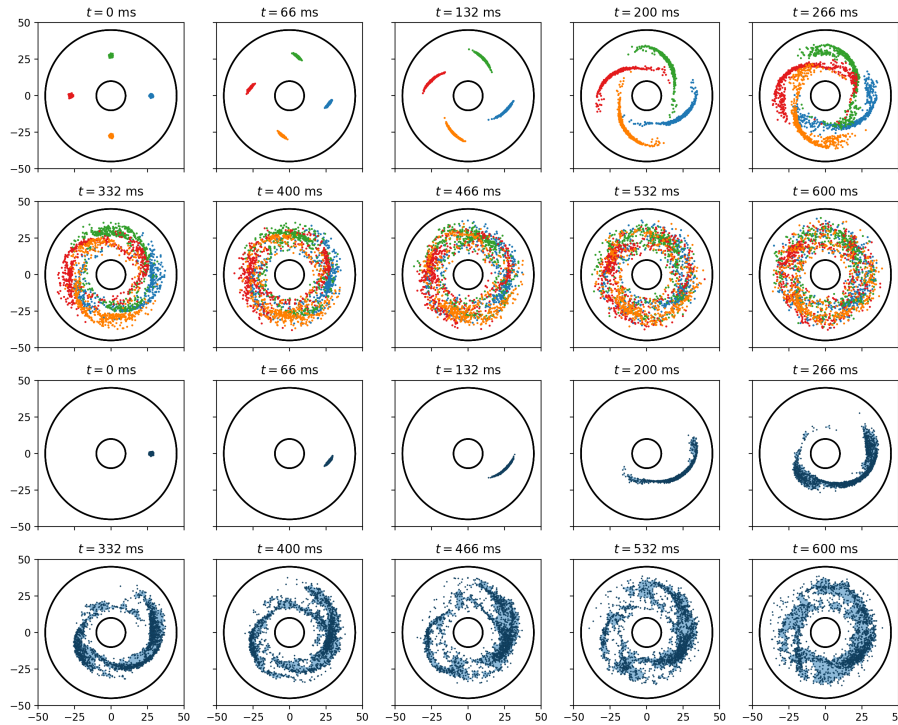


Figure 5.13: Temporal evolution of a system with 4 vortices, 500 simulations under slightly different initial conditions. First and second row: each vortex ensemble is colored differently. Third and Fourth rows: We focus on the dynamics of a vortex single ensemble. The area corresponds to the best concave area describing the ensemble.

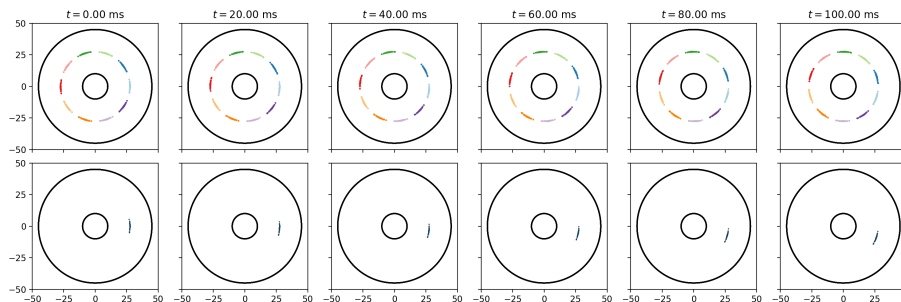


Figure 5.14: Temporal evolution of a system with 10 vortices, 50 simulations under slightly different initial conditions. First and second row: each vortex ensemble is colored differently. Third and Fourth rows: We focus on the dynamics of a vortex single ensemble. The area corresponds to the best concave area describing the ensemble.

positions with radii below R_0 (colored in blue tones), the trajectories seem to follow each other, the same happens for positions with radii above R_0 (colored in red tones).

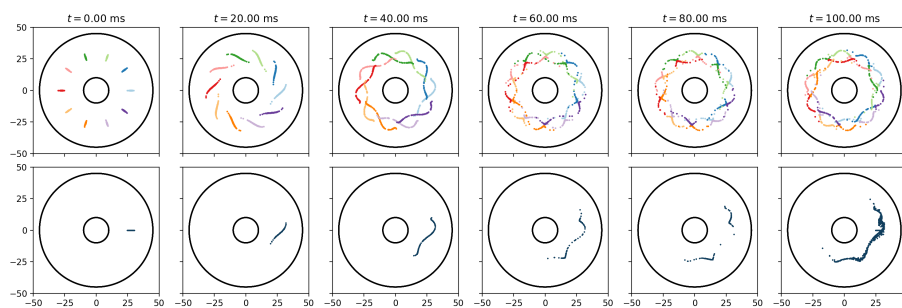


Figure 5.15: Temporal evolution of a system with 10 vortices, 100 simulations under slightly different initial conditions. First and second row: each vortex ensemble is colored differently. Third and Fourth rows: We focus on the dynamics of a vortex single ensemble. The area corresponds to the best concave area describing the ensemble.

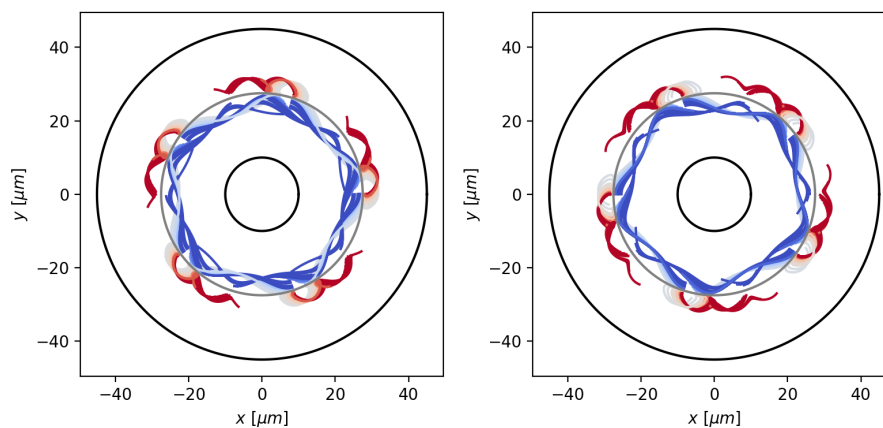


Figure 5.16: Temporal evolution of a system with 10 vortices, 100 simulations under slightly different initial conditions. For clarity, we set even position vortices on the left panel, and odd positions on the right.

However, between them the trajectories clearly diverges.

5.3.2 Effect of vortex dissipation

To quantify the effects of vortex dissipation, namely by the introduction of the mutual friction coefficient α , we repeated the simulations of Figure 5.13 setting $\alpha = 0.1$. The effect of dissipation is clear, the trajectories differ significantly from those without dissipation. Vortices tend to leave the system, either by collapsing into the inner region, removing part of the enclosed topological charge, or by leaving through the outer boundary. The phase space covered becomes a spiral whose shape depends on

the value of α . The inclusion of dissipation into the system suppressed the chaotic behavior observed in the previous section for dissipation-less dynamics. In fact, we can intuitively recover the spiral behavior due to the real and imaginary components of the angular frequency obtained from Eq. (5.23).

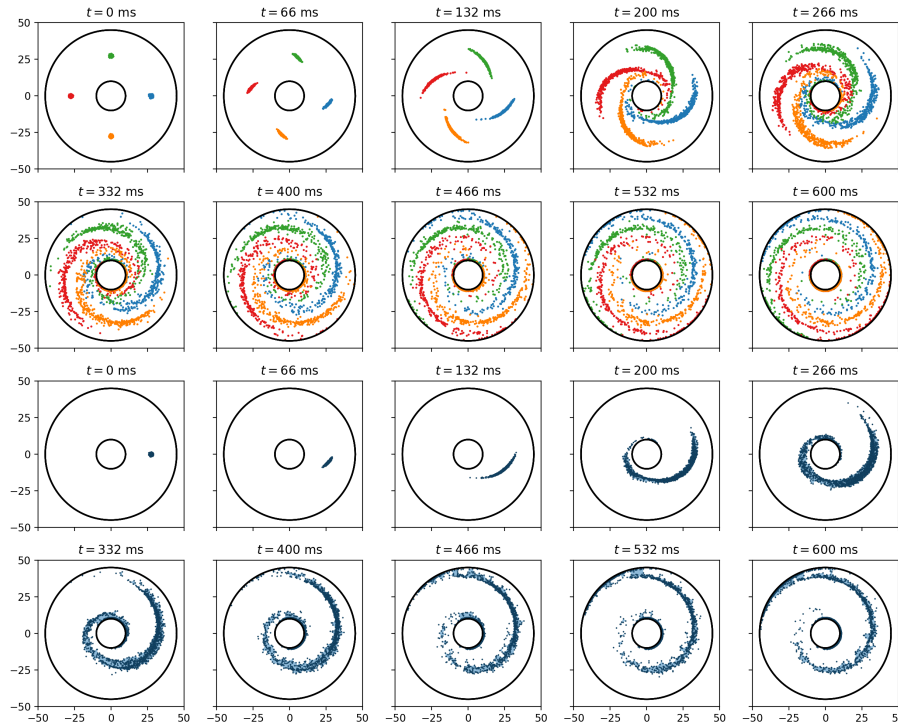


Figure 5.17: Temporal evolution of a system with 4 vortices, 400 simulations under slightly different initial conditions, introducing the dissipation coefficient $\alpha = 0.1$. First and second row: each vortex ensemble is colored differently. Third and Fourth rows: We focus on the dynamics of a vortex single ensemble. The area corresponds to the best concave area describing the ensemble.

5.4 Growth rate and dispersion relation

5.4.1 Vortex structure factor

Although by looking at the trajectories of individual vortices we can reconstruct the maximal growth rate of the vortex array instability, we cannot follow the same protocol from the experimental images. As mentioned, we perform absorption imaging, meaning we destroy the sample in every shot we take, both because we perform a

short time of flight to enhance the contrast of vortices, and because of the destructive resonant imaging. Moreover, as we explored in the previous section considering small fluctuations in the initial position of the vortices can lead to full different temporal evolutions. As we learn from the point vortex simulations, the instability growth rate associated to the Kelvin-Helmholtz instability can be obtained from the very first temporal evolution, where the vortex polygon breaks. The only tools we have available to study the ensemble dynamics of our system is looking to the correlations between vortices as a function of time.

One way to study the correlations in our vortex polygon is by thinking of it as a linear array of vortices in a periodic direction, namely the angular one. To study the small deviations from the perfect polygon array, we take advantage of the structure factor of the vortex array [46, 49, 175] defined as:

$$S(m, t) = \frac{1}{N_v} \sum_{j,l}^{N_v} e^{im(\theta_j(t) - \theta_l(t))} \quad (5.32)$$

where θ_j corresponds to the angular coordinate of the j -th vortex, and m is an integer corresponding to the angular mode associated to a perturbation with wavenumber k such that $m = kR_0$. The structure factor encodes the positions of the vortices which, at $t = 0$, should provide a spectral peak at $m = \Delta w = N_v$.

In order to compute the structure factor $S(m, t)$ we need to retrieve from the experimental images the positions of the vortices in each realization. To pin point the vortices, I developed a program which allows the user to click in the position of the vortices, saving their coordinates in a txt file. Initially, this program did not had any built-in protocol to locate the positions of the vortices. Since, we care about the precise positions of the vortices, we had to manually go through the 200000 images of the full experimental dataset locating the positions of each vortex. On a newer version, the inclusion of machine learning approach to detect the vortices was implemented, which acts as an initial guess of the positions. In either case, a manual inspection of the data is required.

From the data collected as a function of time we can compute $S(m, t)$ for different number of vortices. Figure 5.19 shows an example for $N = 14$ for a BEC and UFG superfluids. At $t = 0$ we notice the spectral peak at $m = \Delta w = N_v$, which for latter times, tend to move towards lower angular modes. Moreover, if we look at the temporal evolution of the $S(m, t)$ fixing the angular mode m , lower panels of Figure

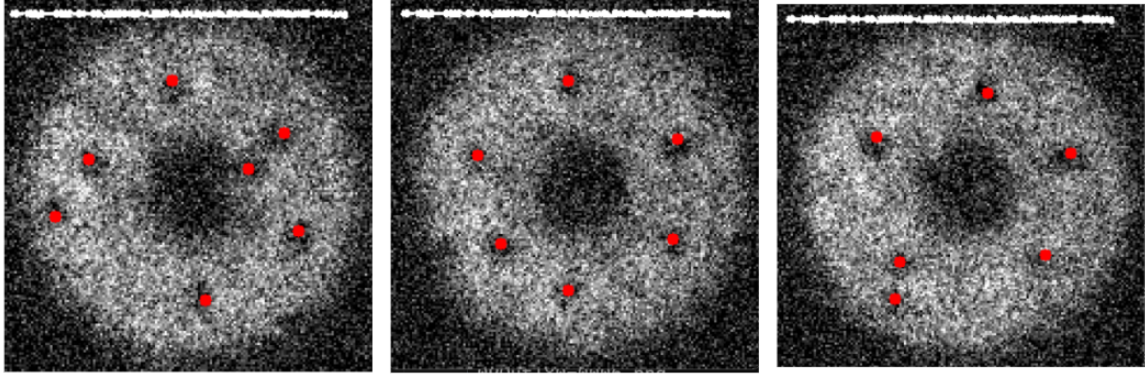


Figure 5.18: Example of images and positions of the vortices pin pointed by the software.

5.19, we observe this quantity grows exponentially with different rates depending on m .

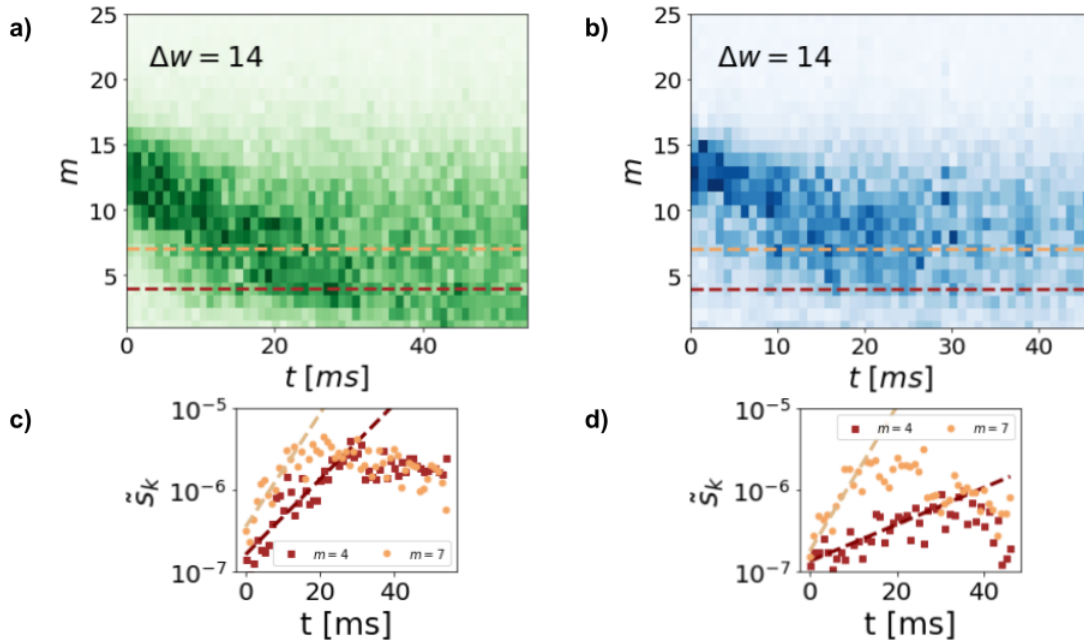


Figure 5.19: Measured structure factor for all modes m in a) BEC, and b) UFG superfluids. Examples of the exponential growth dependence in time for different modes for the c) BEC, and d) UFG cases. The data points correspond to the dashed horizontal lines of panels a) and b) respectively.

As the instability starts to grow, the vortices start to move from their original positions $\theta_j^0 = 2\pi j/N$. Considering infinitesimal movements of the vortices, such that $\theta_j = \theta_j^0 + \delta\theta$. In crystals, small fluctuations ($\delta\theta \ll 2\pi/N_v$) are considered as

a disorder of the first kind [175], and they modify the structure factor as $S(m, t) \approx S^d(m) - m^2 \langle \delta\theta^2 \rangle(t) S^d(m)$, where $S^d(m)$ correspond to the structure factor of a given realization, and in general $S^d(m) \neq 0$, for different m . In the limit case, taking the average over many realizations, $S^d(m) \rightarrow S^0(m)$. Here, the temporal dependence of $S(m, t)$ is entirely provided by the term $\langle \delta\theta^2 \rangle(t)$.

Mapping the problem from the point vortex model [96, 97], the deviation from their initial position grows as $\delta\theta \sim e^{\sigma_m t}$, where σ_m is given by Eq. (5.26). Therefore, the temporal evolution of the structure factor to be $S(m, t) \sim e^{2\sigma_m t}$. Fitting the exponential behavior of $S(m, t)$ for the different modes m will therefore allow us to reconstruct the imaginary part of the dispersion relation governing the vortex instability.

5.4.2 Measured instability growth rate

In this last section, I discuss the main result of this thesis: the measured dispersion relation of the Kelvin-Helmholtz instability in single-component superfluids.

Figure 5.20 shows the results we get for the imaginary part of the dispersion relation for different interaction regimes: BEC, UFG, and BCS superfluids, together with the comparison with all the different models: the low-wavenumber limit, $\frac{1}{2}k\Delta v$ normalized to σ_{PVM}^* , while solid lines show the rates predicted by the point vortex model in Eq. (3.30) and by Rayleigh's Eq. (3.19) using $\delta = 0.8\hbar/M\Delta v$ for the thickness of the interface layer.

To obtain the maximum growth rate σ^* experimentally, we fitted the dispersion relation of the measured rates, Fig. 5.20 c-e, using the following function $f(x, \sigma^*) = \sigma^* \frac{\sqrt{e^{-4\eta x} - (2\eta x - 1)^2}}{A}$, with $x = m/\Delta w$, and $A = \max \left[\sqrt{e^{-4\eta x} - (2\eta x - 1)^2} \right] = (W(e^{-1}) + 1)/(2\eta) \approx 0.639/\eta$, where $W(x)$ is the Lambert W-function and $\eta = 0.8$. The function $f(x, 1)$ corresponds to Eq. (3.19) normalized to the maximum value shown as the magenta line in Fig. 5.20a-c. We perform the fit of the dispersion relation letting σ^* as the only free parameter. It is worth noting that for the behavior of σ_m/σ^* appears to be independent on the number of vortices in the vortex polygon, as shown by the different symbols in Fig. 5.20a-c. Highlighting the origin of a common behavior for all differential velocities Δv at the interface between the superfluids.

In Fig. 5.20 d, the extracted σ^* for different superfluid regimes is plotted as a function of the relative velocity, displaying a quadratic behavior which is compatible

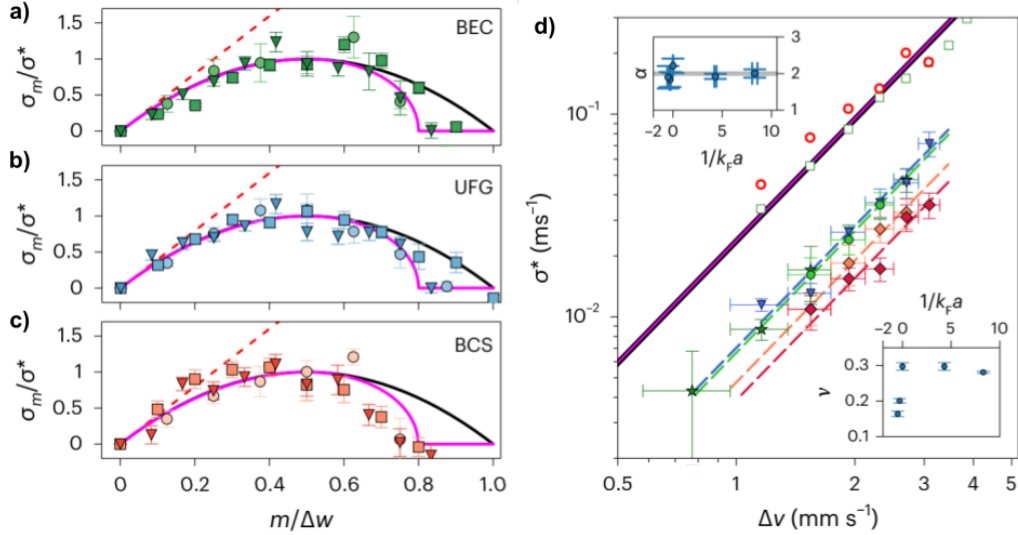


Figure 5.20: a-c) Normalized dispersion relations for the a) BEC at $1/k_F a = 4.1$, b) UFG at $1/k_F a = 0$, c) BCS at $1/k_F a = 0.3$. We show the comparison we all the different models. d) Scaling of σ^* against Δv in different interaction regimes. Filled symbols correspond to BCS ($1/k_F a = -0.5(1)$, red diamonds), ($1/k_F a = -0.3(1)$, orange diamonds); UFG ($1/k_F a = 0.0(1)$, blue triangles); and BEC ($1/k_F a = 4.3(1)$, dark green stars), ($1/k_F a = 8.3(3)$, light green circles). Open symbols refer to GP simulations at $T = 0$ (open green squares) and cZNG simulations at $T/T_c = 0.4$ (open red circles) for $1/k_F a = 4.3(1)$. Solid lines refer to Rayleigh's (magenta) and the point vortex model (black) predictions. Dashed lines denote fits with $\sigma^* = A\Delta v^\alpha$. As insets, as a function of $1/k_F a$: (top) fitted scaling exponents α ; (bottom) adimensional factor ν defined as $\sigma^* = \nu \sigma_{\text{PVM}}^*$. Image adapted from [49].

with the calculations of the point vortex model maximum growth rate:

$$\sigma^* = \frac{\kappa\pi}{4d_v^2} = \frac{\kappa\pi}{4(2\pi R_0/N)^2} = \frac{2\pi\hbar}{M}\pi(\Delta v)^2 = \frac{M}{8\hbar}(\Delta v)^2. \quad (5.33)$$

These scaling properties, together with the normalized dispersion relations in Fig. 5.20a-c provide clear evidence of the Kelvin-Helmholtz instability dynamics in superfluids and of its *universality* across the BEC-BCS crossover.

The data in Fig. 5.20 d are compared with Eqs. (3.30) and (3.19), and with numerical simulations obtained from GPE and the collisionless Zaremba-Nikuni-Griffin (cZNG) model [49, 176]. The latter model simulations where performed by K. Khani using a self-consistent finite-temperature kinetic model coupling the evolution of a condensate (following a GPE equation), with the evolution of a Boltzmann equa-

tion given by a thermal cloud on non-condensed atoms [177]. The latter term, can account for different couplings between the condensate and thermal cloud from the collision terms of the Boltzmann equation. The cZNG considers the scenario where the condensate and thermal cloud only interact via a mean-field energy shift, without allowing the exchange of particles from the condensate to the thermal cloud. To directly compare the numerical simulations with the experimental data we performed the same extrapolation of the growth rate using the structure factor definition. All theoretically obtained rates – analytical and numerical – agree quantitatively with each other, while the measured ones show systematically lower values. In particular, since we observe that the experimental data follows the same scaling law with the differential velocity Δv , namely $(\Delta v)^2$ as the theoretical models, we can quantify the mismatch by the ratio $\nu = \sigma^*/\sigma_{\text{PVM}}^*$, presented as an inset of Figure 5.20.

In classical fluids, dissipation effects typically stabilize the system, leading to lower growth rates [79, 80]. In our system, we expect a finite temperature to introduce dissipation effects in the form of scattering processes between normal excitations and vortices, through the presence of the mutual friction coefficients. These are ubiquitous sources of dissipation in any superfluid and strongly depend on the vortex core structure [75, 76].

The growth rate in the presence of mutual friction coefficients can be adjusted through the correction factor mentioned in the previous section, namely:

$$\sigma_m = \sqrt{(1 - \alpha')^2 + \alpha^2} \sigma_m^0 \approx (1 - \alpha' + \frac{1}{2}\alpha^2) \sigma_m^0, \quad (5.34)$$

where it is clear there exist the possibility of the dynamics to be slower than the idealized superfluids by considering an $\alpha' > 0$. Moreover, the effect of the dissipative coefficient α is quadratic in nature and can be neglected to first order. The most plausible reason we observe slower rates as the ones expected from non-dissipative theories could be due to mutual friction.

It is important to note that mutual friction strongly depends on the nature of the superfluids [75, 91]. For bosonic ^4He , the dissipative coefficient α' is considered almost 0 ($\alpha' \approx \alpha^2 \sim 10^{-4}$) for temperatures below $0.8T_c$. On the other hand, fermionic superfluid ^3He displays values of α' above 0.2 for temperatures above $0.3T_c$, eventually reaching 1 for close to T_c , ultimately dominating over α in a large range of temperatures. From these known results, we could speculate the role of mutual friction across the BEC-BCS crossover to be more similar to the one observed in fermionic superfluid

^3He due to the structure of the vortex core [75]. Hence, one would expect models such as ZNG to fail in the description of mutual friction for strongly interacting BEC's near the crossover regime. Providing a measurement of these coefficients requires to precisely compare the theoretical models with the experimental data to provide quantitative comparison.

5.4.3 Geometrical instability suppression

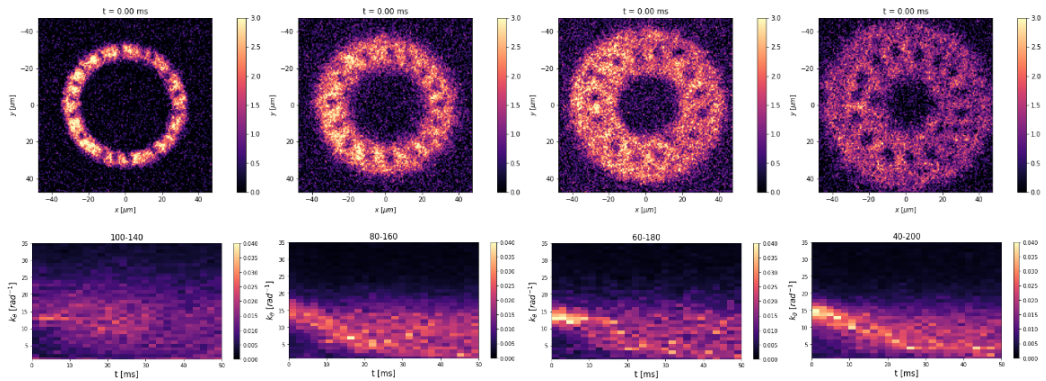


Figure 5.21: Geometrical suppression of the instability, simply by modifying the width of the system, leaving the radii of the vortex polygon constant.

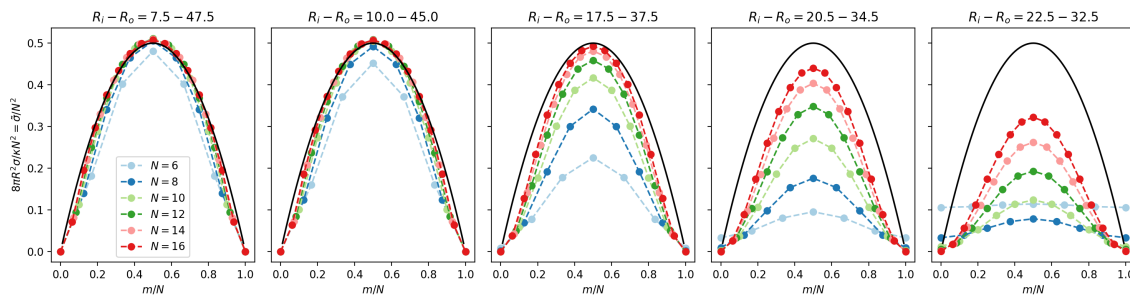


Figure 5.22: Geometrical suppression of the instability, simply by modifying the width of the system, leaving the radii of the vortex polygon constant.

Mutual friction is not the only effect that can help suppress the instability growth rates. Indeed, we can modify the geometric arrangement of the system by considering the dynamics of vortices in thinner annular superfluids [94], as shown in Figure 5.21. On the lower panels I show the structure factor associated to the dynamics of the vortices in the annular traps shown in the panels above. We considered the case for $N = 16$, and we keep constant the radius of the vortex polygon. In Figure 5.22,

we confirm this behavior by computing the theoretical values of the growth rate for different geometries, where in general, we observe a suppression of the instability rate.

However, we note that geometrical restrictions are not the reason of the mismatch between the observed growth rate shown in Figure 5.20 since these are taken into account in the theoretical models already.

Chapter 6

Conclusions and Outlook

In this thesis I investigated the onset and evolution of the Kelvin-Helmholtz instability in fermionic superfluids across the BEC-BCS crossover [49]. The system involved two counter-rotating annular superflows separated by a thin potential barrier. I presented the protocol employed for the generation of the persistent currents necessary in each annular superfluid. I characterized the creation of the initial condition of the counter-rotating persistent currents, each with the same number of circulation quanta. By tuning the barrier height, we controlled the merging dynamics of the superfluid. I explored the regime of fast and slow removal dynamics showing the two distinct behaviors from spiral soliton behavior to the ordered array of quantized vortices. I analyzed the dynamics behind the transition from a barrier interface into an ordered array of quantized vortices. Moreover, to provide more insights about this, I solved the Gross-Pitaevskii equation, and proposed that the formation dynamics can be mapped to the one of linear atomic Josephson junction, explaining the emergence of the vortices as a natural solution to the phase-induced tunneling dynamics. A possible extension for future work could be to perform a more in-depth study of the linear atomic Josephson junction dynamics, working in the presence of the tunneling barrier, specially in the limit of thin annular superfluids in both the bosonic and fermionic sides of the Feshbach resonance.

I observed how the polygonal array loses stability and rolls up into vortex clusters. The Kelvin-Helmholtz Instability in this scenario appears as the instability breaking the regular array of vortices. Extracting the instability growth rates from the experimental data, we find that they obey the same scaling relations across the different superfluid regimes, although vortex dynamics appears to be consistently slower than

predicted by theoretical models. I developed the theoretical framework describing the instability using the dissipative point-vortex model. This model describes the motion of superfluid vortices in the presence of a mutual friction with the normal component of the system, and offers a mechanism through which vortex dynamics can be generally slower. A natural extension of this work is to analyze the behavior of the mutual friction as a function of the temperature of the system and the interaction regime. The mechanisms behind the origin of the mutual friction rely on the microscopic nature and structure of the vortices [75, 76, 91]. Across the BEC-BCS crossover the vortex structure changes dramatically [178], and altering dramatically the propagation of vortices.

These new results offer new perspectives of the behavior of vortex turbulence in fermionic superfluids, with the KHI being a precursor of a possible first observation of such dynamics in strongly correlated superfluids. Our work opens new ways to study non-equilibrium phenomena in strongly correlated quantum matter, whose implication can be extended from rapidly rotating quantum gases [179] to pulsar glitches [180] and neutron star mergers [181]. An exciting direction for future experiments consist of studying the cascade of secondary instabilities, in longer timescales, towards the spontaneous onset of quantum vortex turbulence [114, 120, 121], exploring a different route which is complementary to external forcing [24, 182] to probe its underlying microscopic mechanisms from the few- to the many-vortex perspective.

Bibliography

- [1] Tilman Esslinger. “Fermi-Hubbard Physics with Atoms in an Optical Lattice”. In: *Annual Review of Condensed Matter Physics* 1.1 (Aug. 2010), 129–152. ISSN: 1947-5462. DOI: 10.1146/annurev-conmatphys-070909-104059. URL: <http://dx.doi.org/10.1146/annurev-conmatphys-070909-104059>.
- [2] Immanuel Bloch, Jean Dalibard, and Wilhelm Zwerger. “Many-body physics with ultracold gases”. In: *Rev. Mod. Phys.* 80 (3 2008), pp. 885–964. DOI: 10.1103/RevModPhys.80.885. URL: <https://link.aps.org/doi/10.1103/RevModPhys.80.885>.
- [3] Christian Gross and Immanuel Bloch. “Quantum simulations with ultracold atoms in optical lattices”. In: *Science* 357.6355 (Sept. 2017), 995–1001. ISSN: 1095-9203. DOI: 10.1126/science.aal3837. URL: <http://dx.doi.org/10.1126/science.aal3837>.
- [4] H. P. Büchler et al. “Atomic Quantum Simulator for Lattice Gauge Theories and Ring Exchange Models”. In: *Physical Review Letters* 95.4 (July 2005). ISSN: 1079-7114. DOI: 10.1103/physrevlett.95.040402. URL: <http://dx.doi.org/10.1103/PhysRevLett.95.040402>.
- [5] S. Giovanazzi. “Hawking Radiation in Sonic Black Holes”. In: *Physical Review Letters* 94.6 (Feb. 2005). ISSN: 1079-7114. DOI: 10.1103/physrevlett.94.061302. URL: <http://dx.doi.org/10.1103/PhysRevLett.94.061302>.
- [6] Wilhelm Zwerger, ed. *The BCS-BEC Crossover and the Unitary Fermi Gas*. Springer Berlin Heidelberg, 2012. DOI: 10.1007/978-3-642-21978-8. URL: <https://doi.org/10.1007/978-3-642-21978-8>.
- [7] Matthias Troyer and Uwe-Jens Wiese. “Computational Complexity and Fundamental Limitations to Fermionic Quantum Monte Carlo Simulations”. In: *Physical Review Letters* 94.17 (May 2005). ISSN: 1079-7114. DOI: 10.1103/

- physrevlett.94.170201. URL: <http://dx.doi.org/10.1103/PhysRevLett.94.170201>.
- [8] Richard P. Feynman. “Simulating physics with computers”. In: *International Journal of Theoretical Physics* 21.6–7 (June 1982), 467–488. ISSN: 1572-9575. DOI: 10.1007/bf02650179. URL: <http://dx.doi.org/10.1007/BF02650179>.
- [9] Cheng Chin et al. “Feshbach resonances in ultracold gases”. In: *Reviews of Modern Physics* 82.2 (Apr. 2010), pp. 1225–1286. DOI: 10.1103/revmodphys.82.1225. URL: <https://doi.org/10.1103/revmodphys.82.1225>.
- [10] Rudolf Grimm, Matthias Weidemüller, and Yurii B. Ovchinnikov. “Optical Dipole Traps for Neutral Atoms”. In: *Advances in Atomic Molecular and Optical Physics* 42 (Jan. 2000), pp. 95–170. DOI: 10.1016/S1049-250X(08)60186-X. arXiv: physics/9902072 [physics.atom-ph].
- [11] A. J. Leggett. “Diatomic molecules and cooper pairs”. In: *Modern Trends in the Theory of Condensed Matter*. Springer Berlin Heidelberg, 13–27. ISBN: 9783540386285. DOI: 10.1007/bfb0120125. URL: <http://dx.doi.org/10.1007/BFb0120125>.
- [12] Markus Greiner et al. “Quantum phase transition from a superfluid to a Mott insulator in a gas of ultracold atoms”. In: *Nature* 415.6867 (Jan. 2002), 39–44. ISSN: 1476-4687. DOI: 10.1038/415039a. URL: <http://dx.doi.org/10.1038/415039a>.
- [13] Robert Jördens et al. “A Mott insulator of fermionic atoms in an optical lattice”. In: *Nature* 455.7210 (Sept. 2008), 204–207. ISSN: 1476-4687. DOI: 10.1038/nature07244. URL: <http://dx.doi.org/10.1038/nature07244>.
- [14] W. Ketterle and M. W. Zwierlein. “Making, probing and understanding ultracold Fermi gases”. In: *Nuovo Cimento Rivista Serie* 31.5-6 (May 2008), pp. 247–422. DOI: 10.1393/ncr/i2008-10033-1. arXiv: 0801.2500 [cond-mat.other].
- [15] Mark J. H. Ku et al. “Revealing the Superfluid Lambda Transition in the Universal Thermodynamics of a Unitary Fermi Gas”. In: *Science* 335.6068 (Feb. 2012), 563–567. ISSN: 1095-9203. DOI: 10.1126/science.1214987. URL: <http://dx.doi.org/10.1126/science.1214987>.
- [16] C. J. Pethick and H. Smith. *Bose–Einstein Condensation in Dilute Gases*. Cambridge University Press, Sept. 2008. ISBN: 9780511802850. DOI: 10.1017/cbo9780511802850. URL: <http://dx.doi.org/10.1017/CB09780511802850>.

- [17] J. R. Abo-Shaeer et al. “Observation of Vortex Lattices in Bose-Einstein Condensates”. In: *Science* 292.5516 (Apr. 2001), 476–479. ISSN: 1095-9203. DOI: 10.1126/science.1060182. URL: <http://dx.doi.org/10.1126/science.1060182>.
- [18] M. W. Zwierlein et al. “Vortices and superfluidity in a strongly interacting Fermi gas”. In: *Nature* 435.7045 (June 2005), 1047–1051. ISSN: 1476-4687. DOI: 10.1038/nature03858. URL: <http://dx.doi.org/10.1038/nature03858>.
- [19] Juan Ignacio Polanco, Nicolás P. Müller, and Giorgio Krstulovic. “Vortex clustering, polarisation and circulation intermittency in classical and quantum turbulence”. In: *Nature Comm.* 12.1 (2021), p. 7090. ISSN: 2041-1723. DOI: 10.1038/s41467-021-27382-6. URL: <https://doi.org/10.1038/s41467-021-27382-6>.
- [20] G. P. Klaassen and W. R. Peltier. “The onset of turbulence in finite-amplitude Kelvin–Helmholtz billows”. In: *J. Fluid Mech.* 155 (June 1985), p. 1. DOI: 10.1017/s0022112085001690. URL: <https://doi.org/10.1017/s0022112085001690>.
- [21] W. F. Vinen and J. J. Niemela. “Quantum Turbulence”. In: *Journal of Low Temperature Physics* 128.5/6 (2002), 167–231. ISSN: 0022-2291. DOI: 10.1023/a:1019695418590. URL: <http://dx.doi.org/10.1023/A:1019695418590>.
- [22] Carlo F. Barenghi, Ladislav Skrbek, and Katepalli R. Sreenivasan. “Introduction to quantum turbulence”. In: *Proceedings of the National Academy of Sciences* 111.supplement₁ (Mar. 2014), 4647–4652. ISSN: 1091-6490. DOI: 10.1073/pnas.1400033111. URL: <http://dx.doi.org/10.1073/pnas.1400033111>.
- [23] Davide Proment, Sergey Nazarenko, and Miguel Onorato. “Quantum turbulence cascades in the Gross-Pitaevskii model”. In: *Physical Review A* 80.5 (Nov. 2009). ISSN: 1094-1622. DOI: 10.1103/physreva.80.051603. URL: <http://dx.doi.org/10.1103/PhysRevA.80.051603>.
- [24] Nir Navon et al. “Emergence of a turbulent cascade in a quantum gas”. In: 539.7627 (Nov. 2016), pp. 72–75. DOI: 10.1038/nature20114. URL: <https://doi.org/10.1038/nature20114>.

- [25] Simone Babuin et al. “Effective viscosity in quantum turbulence: A steady-state approach”. In: *EPL (Europhysics Letters)* 106.2 (Apr. 2014), p. 24006. ISSN: 1286-4854. DOI: 10.1209/0295-5075/106/24006. URL: <http://dx.doi.org/10.1209/0295-5075/106/24006>.
- [26] G.W. Stagg, N.G. Parker, and C.F. Barenghi. “Superfluid Boundary Layer”. In: *Physical Review Letters* 118.13 (Mar. 2017). ISSN: 1079-7114. DOI: 10.1103/physrevlett.118.135301. URL: <http://dx.doi.org/10.1103/PhysRevLett.118.135301>.
- [27] Chen-Lung Hung et al. “Observation of scale invariance and universality in two-dimensional Bose gases”. In: *Nature* 470.7333 (Jan. 2011), 236–239. ISSN: 1476-4687. DOI: 10.1038/nature09722. URL: <http://dx.doi.org/10.1038/nature09722>.
- [28] Rémi Desbuquois et al. “Superfluid behaviour of a two-dimensional Bose gas”. In: *Nature Physics* 8.9 (July 2012), 645–648. ISSN: 1745-2481. DOI: 10.1038/nphys2378. URL: <http://dx.doi.org/10.1038/nphys2378>.
- [29] Sang Won Seo et al. “Observation of vortex-antivortex pairing in decaying 2D turbulence of a superfluid gas”. In: *Scientific Reports* 7.1 (July 2017). ISSN: 2045-2322. DOI: 10.1038/s41598-017-04122-9. URL: <http://dx.doi.org/10.1038/s41598-017-04122-9>.
- [30] Brendan C. Mulkerin et al. “Superfluid density and critical velocity near the Berezinskii-Kosterlitz-Thouless transition in a two-dimensional strongly interacting Fermi gas”. In: *Physical Review A* 96.5 (Nov. 2017). ISSN: 2469-9934. DOI: 10.1103/physreva.96.053608. URL: <http://dx.doi.org/10.1103/PhysRevA.96.053608>.
- [31] Bumsuk Ko, Jee Woo Park, and Y. Shin. “Kibble–Zurek universality in a strongly interacting Fermi superfluid”. In: *Nature Physics* 15.12 (Sept. 2019), 1227–1231. ISSN: 1745-2481. DOI: 10.1038/s41567-019-0650-1. URL: <http://dx.doi.org/10.1038/s41567-019-0650-1>.
- [32] G. I. Harris et al. “Laser cooling and control of excitations in superfluid helium”. In: *Nature Physics* 12.8 (Apr. 2016), 788–793. ISSN: 1745-2481. DOI: 10.1038/nphys3714. URL: <http://dx.doi.org/10.1038/nphys3714>.

- [33] Kazuki Sasaki, Naoya Suzuki, and Hiroki Saito. “Bénard–von Kármán Vortex Street in a Bose-Einstein Condensate”. In: *Physical Review Letters* 104.15 (Apr. 2010). ISSN: 1079-7114. DOI: 10.1103/physrevlett.104.150404. URL: <http://dx.doi.org/10.1103/PhysRevLett.104.150404>.
- [34] Woo Jin Kwon et al. “Observation of von Kármán Vortex Street in an Atomic Superfluid Gas”. In: *Physical Review Letters* 117.24 (Dec. 2016). ISSN: 1079-7114. DOI: 10.1103/physrevlett.117.245301. URL: <http://dx.doi.org/10.1103/PhysRevLett.117.245301>.
- [35] Tapio Simula, Matthew J. Davis, and Kristian Helmerson. “Emergence of Order from Turbulence in an Isolated Planar Superfluid”. In: *Physical Review Letters* 113.16 (Oct. 2014). ISSN: 1079-7114. DOI: 10.1103/physrevlett.113.165302. URL: <http://dx.doi.org/10.1103/PhysRevLett.113.165302>.
- [36] Shaun P. Johnstone et al. “Evolution of large-scale flow from turbulence in a two-dimensional superfluid”. In: *Science* 364.6447 (June 2019), 1267–1271. ISSN: 1095-9203. DOI: 10.1126/science.aat5793. URL: <http://dx.doi.org/10.1126/science.aat5793>.
- [37] Xiaoquan Yu et al. “Theory of the vortex-clustering transition in a confined two-dimensional quantum fluid”. In: *Physical Review A* 94.2 (Aug. 2016). ISSN: 2469-9934. DOI: 10.1103/physreva.94.023602. URL: <http://dx.doi.org/10.1103/PhysRevA.94.023602>.
- [38] Guillaume Gauthier et al. “Giant vortex clusters in a two-dimensional quantum fluid”. In: *Science* 364.6447 (June 2019), 1264–1267. ISSN: 1095-9203. DOI: 10.1126/science.aat5718. URL: <http://dx.doi.org/10.1126/science.aat5718>.
- [39] Matthew T. Reeves et al. “Turbulent Relaxation to Equilibrium in a Two-Dimensional Quantum Vortex Gas”. In: *Physical Review X* 12.1 (Feb. 2022). ISSN: 2160-3308. DOI: 10.1103/physrevx.12.011031. URL: <http://dx.doi.org/10.1103/PhysRevX.12.011031>.
- [40] Woo Jin Kwon et al. “Relaxation of superfluid turbulence in highly oblate Bose-Einstein condensates”. In: *Physical Review A* 90.6 (Dec. 2014). ISSN: 1094-1622. DOI: 10.1103/physreva.90.063627. URL: <http://dx.doi.org/10.1103/PhysRevA.90.063627>.

- [41] S. A. Thorpe. “On the Kelvin–Helmholtz route to turbulence”. In: *J. Fluid Mech.* 708 (Sept. 2012), pp. 1–4. DOI: 10.1017/jfm.2012.383. URL: <https://doi.org/10.1017/jfm.2012.383>.
- [42] A. Mashayek and W. R. Peltier. “The ‘zoo’ of secondary instabilities precursory to stratified shear flow transition. Part 1 Shear aligned convection, pairing, and braid instabilities”. In: *J. Fluid Mech.* 708 (Aug. 2012), pp. 5–44. DOI: 10.1017/jfm.2012.304. URL: <https://doi.org/10.1017/jfm.2012.304>.
- [43] A. Mashayek and W. R. Peltier. “The ‘zoo’ of secondary instabilities precursory to stratified shear flow transition. Part 2 The influence of stratification”. In: *J. Fluid Mech.* 708 (Sept. 2012), pp. 45–70. DOI: 10.1017/jfm.2012.294. URL: <https://doi.org/10.1017/jfm.2012.294>.
- [44] S. A. Thorpe. “Transitional phenomena and the development of turbulence in stratified fluids: A review”. In: *Journal of Geophysical Research* 92.C5 (1987), p. 5231. DOI: 10.1029/jc092ic05p05231. URL: <https://doi.org/10.1029/jc092ic05p05231>.
- [45] R. Blaauwgeers et al. “Shear Flow and Kelvin-Helmholtz Instability in Superfluids”. In: *Phys. Rev. Lett.* 89 (15 2002), p. 155301. DOI: 10.1103/PhysRevLett.89.155301. URL: <https://link.aps.org/doi/10.1103/PhysRevLett.89.155301>.
- [46] Biswaroop Mukherjee et al. “Crystallization of bosonic quantum Hall states in a rotating quantum gas”. In: *Nature* 601.7891 (Jan. 2022), 58–62. ISSN: 1476-4687. DOI: 10.1038/s41586-021-04170-2. URL: <http://dx.doi.org/10.1038/s41586-021-04170-2>.
- [47] A. Mastrano and A. Melatos. “Kelvin-Helmholtz instability and circulation transfer at an isotropic-anisotropic superfluid interface in a neutron star”. In: *Monthly Notices of the Royal Astronomical Society* 361.3 (Aug. 2005), 927–941. ISSN: 1365-2966. DOI: 10.1111/j.1365-2966.2005.09219.x. URL: <http://dx.doi.org/10.1111/j.1365-2966.2005.09219.x>.
- [48] M. Obergaulinger, M. A. Aloy, and E. Müller. “Local simulations of the magnetized Kelvin-Helmholtz instability in neutron-star mergers”. In: *Astronomy and Astrophysics* 515 (June 2010), A30. ISSN: 1432-0746. DOI: 10.1051/0004-6361/200913386. URL: <http://dx.doi.org/10.1051/0004-6361/200913386>.

- [49] D. Hernández-Rajkov et al. “Connecting shear flow and vortex array instabilities in annular atomic superfluids”. In: *Nature Physics* 20.6 (Mar. 2024), 939–944. ISSN: 1745-2481. DOI: 10.1038/s41567-024-02466-4. URL: <http://dx.doi.org/10.1038/s41567-024-02466-4>.
- [50] W. Ketterle, D. S. Durfee, and D. M. Stamper-Kurn. “Making, probing and understanding Bose-Einstein condensates”. In: *arXiv e-prints*, cond-mat/9904034 (Apr. 1999), cond-mat/9904034. arXiv: cond-mat/9904034 [cond-mat].
- [51] D. S. Petrov, C. Salomon, and G. V. Shlyapnikov. “Scattering properties of weakly bound dimers of fermionic atoms”. In: *Physical Review A* 71.1 (Jan. 2005). ISSN: 1094-1622. DOI: 10.1103/physreva.71.012708. URL: <http://dx.doi.org/10.1103/PhysRevA.71.012708>.
- [52] B. DeMarco et al. “Measurement of p-Wave Threshold Law Using Evaporatively Cooled Fermionic Atoms”. In: *Physical Review Letters* 82.21 (May 1999), pp. 4208–4211. DOI: 10.1103/physrevlett.82.4208. URL: <https://doi.org/10.1103/physrevlett.82.4208>.
- [53] A. Amico. “Probing the many dynamics of ultracold repulsive Fermi gases of lithium atoms”. PhD thesis. Università degli studi Firenze, 2018.
- [54] C. A. Regal, M. Greiner, and D. S. Jin. “Observation of Resonance Condensation of Fermionic Atom Pairs”. In: *Physical Review Letters* 92.4 (Jan. 2004). ISSN: 1079-7114. DOI: 10.1103/physrevlett.92.040403. URL: <http://dx.doi.org/10.1103/PhysRevLett.92.040403>.
- [55] Karl-Heinz Bennemann and John B. Ketterson. *Novel Superfluids: Volume 2*. Oxford University Press, Nov. 2014. ISBN: 9780198719267. DOI: 10.1093/acprof:oso/9780198719267.001.0001. URL: <https://doi.org/10.1093/acprof:oso/9780198719267.001.0001>.
- [56] R. Haussmann and W. Zwerger. “Thermodynamics of a trapped unitary Fermi gas”. In: *Phys. Rev. A* 78 (6 2008), p. 063602. DOI: 10.1103/PhysRevA.78.063602. URL: <https://link.aps.org/doi/10.1103/PhysRevA.78.063602>.
- [57] H. Heiselberg. “Collective Modes of Trapped Gases at the BEC-BCS Crossover”. In: *Phys. Rev. Lett.* 93 (4 2004), p. 040402. DOI: 10.1103/PhysRevLett.93.040402. URL: <https://link.aps.org/doi/10.1103/PhysRevLett.93.040402>.

- [58] P. Kapitza. “Viscosity of Liquid Helium below the λ -Point”. In: *Nature* 141.3558 (Jan. 1938), 74–74. ISSN: 1476-4687. DOI: 10.1038/141074a0. URL: <http://dx.doi.org/10.1038/141074a0>.
- [59] J. F. ALLEN and A. D. MISENER. “Flow Phenomena in Liquid Helium II”. In: *Nature* 142.3597 (Oct. 1938), 643–644. ISSN: 1476-4687. DOI: 10.1038/142643a0. URL: <http://dx.doi.org/10.1038/142643a0>.
- [60] L. TISZA. “Transport Phenomena in Helium II”. In: *Nature* 141.3577 (May 1938), 913–913. ISSN: 1476-4687. DOI: 10.1038/141913a0. URL: <http://dx.doi.org/10.1038/141913a0>.
- [61] D. E. Miller et al. “Critical Velocity for Superfluid Flow across the BEC-BCS Crossover”. In: *Physical Review Letters* 99.7 (Aug. 2007). ISSN: 1079-7114. DOI: 10.1103/physrevlett.99.070402. URL: <http://dx.doi.org/10.1103/PhysRevLett.99.070402>.
- [62] Wolf Weimer et al. “Critical Velocity in the BEC-BCS Crossover”. In: *Phys. Rev. Lett.* 114 (9 2015), p. 095301. DOI: 10.1103/PhysRevLett.114.095301. URL: <https://link.aps.org/doi/10.1103/PhysRevLett.114.095301>.
- [63] A.A. Abrikosov. “The magnetic properties of superconducting alloys”. In: *Journal of Physics and Chemistry of Solids* 2.3 (Jan. 1957), 199–208. ISSN: 0022-3697. DOI: 10.1016/0022-3697(57)90083-5. URL: [http://dx.doi.org/10.1016/0022-3697\(57\)90083-5](http://dx.doi.org/10.1016/0022-3697(57)90083-5).
- [64] Thomas Bland et al. “Vortices in dipolar Bose-Einstein condensates”. In: (2023). DOI: 10.48550/ARXIV.2303.13263. URL: <https://arxiv.org/abs/2303.13263>.
- [65] Lauritz Klaus et al. “Observation of vortices and vortex stripes in a dipolar condensate”. In: *Nature Physics* 18.12 (Oct. 2022), 1453–1458. ISSN: 1745-2481. DOI: 10.1038/s41567-022-01793-8. URL: <http://dx.doi.org/10.1038/s41567-022-01793-8>.
- [66] Eva Casotti et al. *Observation of vortices in a dipolar supersolid*. 2024. DOI: 10.48550/ARXIV.2403.18510. URL: <https://arxiv.org/abs/2403.18510>.
- [67] Sam Patrick et al. “Origin and evolution of the multiply quantized vortex instability”. In: *Physical Review Research* 4.4 (Nov. 2022). ISSN: 2643-1564. DOI: 10.1103/physrevresearch.4.043104. URL: <http://dx.doi.org/10.1103/PhysRevResearch.4.043104>.

- [68] E. J. Yarmchuk, M. J. V. Gordon, and R. E. Packard. “Observation of Stationary Vortex Arrays in Rotating Superfluid Helium”. In: *Physical Review Letters* 43.3 (July 1979), 214–217. ISSN: 0031-9007. DOI: 10.1103/physrevlett.43.214. URL: <http://dx.doi.org/10.1103/PhysRevLett.43.214>.
- [69] H. F. Hess et al. “Scanning-Tunneling-Microscope Observation of the Abrikosov Flux Lattice and the Density of States near and inside a Fluxoid”. In: *Physical Review Letters* 62.2 (Jan. 1989), 214–216. ISSN: 0031-9007. DOI: 10.1103/physrevlett.62.214. URL: <http://dx.doi.org/10.1103/PhysRevLett.62.214>.
- [70] Alexander L. Fetter. “Kelvin mode of a vortex in a nonuniform Bose-Einstein condensate”. In: *Phys. Rev. A* 69 (4 2004), p. 043617. DOI: 10.1103/PhysRevA.69.043617. URL: <https://link.aps.org/doi/10.1103/PhysRevA.69.043617>.
- [71] S. J. Rooney et al. “Suppression of Kelvin-induced decay of quantized vortices in oblate Bose-Einstein condensates”. In: *Phys. Rev. A* 84 (2 2011), p. 023637. DOI: 10.1103/PhysRevA.84.023637. URL: <https://link.aps.org/doi/10.1103/PhysRevA.84.023637>.
- [72] Paul K. Newton. *The N-Vortex Problem*. Springer New York, 2001. ISBN: 9781468492903. DOI: 10.1007/978-1-4684-9290-3. URL: <http://dx.doi.org/10.1007/978-1-4684-9290-3>.
- [73] WJ Kwon et al. “Sound emission and annihilations in a programmable quantum vortex collider”. In: *Nature* 600 (2021), pp. 64–69. DOI: 10.1038/s41586-021-04047-4.
- [74] T. D. C. Bevan et al. “Vortex mutual friction in superfluid ^3He ”. In: *Journal of Low Temperature Physics* 109.3–4 (Nov. 1997), 423–459. ISSN: 1573-7357. DOI: 10.1007/bf02396905. URL: <http://dx.doi.org/10.1007/BF02396905>.
- [75] N B Kopnin. “Vortex dynamics and mutual friction in superconductors and Fermi superfluids”. In: *Rep. Progr. Phys.* 65.11 (Sept. 2002), pp. 1633–1678. DOI: 10.1088/0034-4885/65/11/202. URL: <https://doi.org/10.1088/0034-4885/65/11/202>.
- [76] Edouard B. Sonin. *Dynamics of Quantised Vortices in Superfluids*. Cambridge University Press, Dec. 2015. DOI: 10.1017/cbo9781139047616. URL: <https://doi.org/10.1017/cbo9781139047616>.

- [77] Carlo F. Barenghi, Ladislav Skrbek, and Katepalli R. Sreenivasan. “Introduction to quantum turbulence”. In: *Proc. Natl. Acad. Sci. U.S.A.* 111.supplement_1 (Mar. 2014), pp. 4647–4652. DOI: 10.1073/pnas.1400033111. URL: <https://doi.org/10.1073/pnas.1400033111>.
- [78] A. Babiano et al. “Chaotic advection in point vortex models and two-dimensional turbulence”. In: *Phys. Fluids* 6.7 (July 1994), pp. 2465–2474. DOI: 10.1063/1.868194. URL: <https://doi.org/10.1063/1.868194>.
- [79] P G Drazin and W H Reid. *Hydrodynamic Stability*. Cambridge: Cambridge University Press, 2004, pp. 1–31.
- [80] François Charru. *Hydrodynamic Instabilities*. Cambridge University Press, June 2011. DOI: 10.1017/cbo9780511975172. URL: <https://doi.org/10.1017/cbo9780511975172>.
- [81] L. Landau. “Theory of the Superfluidity of Helium II”. In: *Physical Review* 60.4 (Aug. 1941), 356–358. ISSN: 0031-899X. DOI: 10.1103/physrev.60.356. URL: <http://dx.doi.org/10.1103/PhysRev.60.356>.
- [82] Luca Galantucci, Michele Sciacca, and David Jou. “The two-fluid extended model of superfluid helium”. In: *Atti della Accademia Perloritana dei Pericolanti. Classe di Scienze Fisiche, Matematiche e Naturali* 97.S2 (Dec. 2019), A4–1–A4–15. ISSN: 18251242. DOI: 10.1478/AAPP.97S2A4. URL: <https://doi.org/10.1478/AAPP.97S2A4>.
- [83] R. Schäfer and T. Fließbach. “The two-fluid model with superfluid entropy”. In: *Il Nuovo Cimento D* 16.4 (Apr. 1994), 373–390. ISSN: 0392-6737. DOI: 10.1007/bf02451645. URL: <http://dx.doi.org/10.1007/BF02451645>.
- [84] M. Fabrizio and A. Morro. “Thermodynamics and Second Sound in a Two-Fluid Model of Helium II; Revisited”. In: *Journal of Non-Equilibrium Thermodynamics* 28.1 (Jan. 2003). ISSN: 0340-0204. DOI: 10.1515/jnetdy.2003.004. URL: <http://dx.doi.org/10.1515/JNETDY.2003.004>.
- [85] E. Taylor et al. “First and second sound in a strongly interacting Fermi gas”. In: *Physical Review A* 80.5 (Nov. 2009). ISSN: 1094-1622. DOI: 10.1103/physreva.80.053601. URL: <http://dx.doi.org/10.1103/PhysRevA.80.053601>.

- [86] Yan-Hua Hou, Lev P. Pitaevskii, and Sandro Stringari. “First and second sound in a highly elongated Fermi gas at unitarity”. In: *Physical Review A* 88.4 (Oct. 2013). ISSN: 1094-1622. DOI: 10.1103/physreva.88.043630. URL: <http://dx.doi.org/10.1103/PhysRevA.88.043630>.
- [87] Luca Salasnich. “Low-temperature thermodynamics of the unitary Fermi gas: Superfluid fraction, first sound, and second sound”. In: *Physical Review A* 82.6 (Dec. 2010). ISSN: 1094-1622. DOI: 10.1103/physreva.82.063619. URL: <http://dx.doi.org/10.1103/PhysRevA.82.063619>.
- [88] Leonid A. Sidorenkov et al. “Second sound and the superfluid fraction in a Fermi gas with resonant interactions”. In: *Nature* 498.7452 (May 2013), 78–81. ISSN: 1476-4687. DOI: 10.1038/nature12136. URL: <http://dx.doi.org/10.1038/nature12136>.
- [89] Parth B. Patel et al. “Universal sound diffusion in a strongly interacting Fermi gas”. In: *Science* 370.6521 (Dec. 2020), 1222–1226. ISSN: 1095-9203. DOI: 10.1126/science.aaz5756. URL: <http://dx.doi.org/10.1126/science.aaz5756>.
- [90] Zhenjie Yan et al. “Thermography of the superfluid transition in a strongly interacting Fermi gas”. In: *Science* 383.6683 (Feb. 2024), 629–633. ISSN: 1095-9203. DOI: 10.1126/science.adg3430. URL: <http://dx.doi.org/10.1126/science.adg3430>.
- [91] Yuri A. Sergeev. “Mutual Friction in Bosonic Superfluids: A Review”. In: *J. Low Temp. Phys.* (May 2023). URL: <https://doi.org/10.1007/s10909-023-02972-4>.
- [92] H.E. Hall and W.F. Vinen. “The rotation of liquid helium II I. The theory of mutual friction in uniformly rotating helium II”. In: *Proceedings of the Royal Society of London. Series A. Mathematical and Physical Sciences* 238.1213 (Dec. 1956), 204–214. ISSN: 2053-9169. DOI: 10.1098/rspa.1956.0214. URL: <http://dx.doi.org/10.1098/rspa.1956.0214>.
- [93] H.E. Hall and W.F. Vinen. “The rotation of liquid helium II II. The theory of mutual friction in uniformly rotating helium II”. In: *Proceedings of the Royal Society of London. Series A. Mathematical and Physical Sciences* 238.1213 (Dec. 1956), 215–234. ISSN: 2053-9169. DOI: 10.1098/rspa.1956.0215. URL: <http://dx.doi.org/10.1098/rspa.1956.0215>.

- [94] Matteo Caldara et al. “Suppression of the superfluid Kelvin-Helmholtz instability due to massive vortex cores, friction and confinement”. In: *SciPost Physics* 17.3 (Sept. 2024). ISSN: 2542-4653. DOI: 10.21468/scipostphys.17.3.076. URL: <http://dx.doi.org/10.21468/SciPostPhys.17.3.076>.
- [95] Andrea Richaud, Vittorio Penna, and Alexander L. Fetter. “Dynamics of massive point vortices in a binary mixture of Bose-Einstein condensates”. In: *Physical Review A* 103.2 (Feb. 2021). ISSN: 2469-9934. DOI: 10.1103/physreva.103.023311. URL: <http://dx.doi.org/10.1103/PhysRevA.103.023311>.
- [96] Hassan Aref. “On the equilibrium and stability of a row of point vortices”. In: *J. Fluid Mech.* 290 (May 1995), pp. 167–181. DOI: 10.1017/s002211209500245x. URL: <https://doi.org/10.1017/s002211209500245x>.
- [97] T.H. Havelock. “LII. The stability of motion of rectilinear vortices in ring formation”. In: *The London, Edinburgh, and Dublin Philosophical Magazine and Journal of Science* 11.70 (Feb. 1931), pp. 617–633. DOI: 10.1080/14786443109461714. URL: <https://doi.org/10.1080/14786443109461714>.
- [98] J. D. Jackson. *Electrodynamics, Classical*. Apr. 2003. DOI: 10.1002/3527600434.eap109. URL: <http://dx.doi.org/10.1002/3527600434.eap109>.
- [99] J.-P. Martikainen et al. “Generation and evolution of vortex-antivortex pairs in Bose-Einstein condensates”. In: *Physical Review A* 64.6 (Nov. 2001). ISSN: 1094-1622. DOI: 10.1103/physreva.64.063602. URL: <http://dx.doi.org/10.1103/PhysRevA.64.063602>.
- [100] H. von Helmholtz. “Über discontinuierliche Flüssigkeits-Bewegungen [On the discontinuous movements of fluids]”. In: *Monats. Königl. Preuss. Akad. Wiss. Berlin* 23 (1868), pp. 215–228.
- [101] William Smyth and James Moum. “Ocean Mixing by Kelvin-Helmholtz Instability”. In: *Oceanography* 25.2 (June 2012), pp. 140–149. DOI: 10.5670/oceanog.2012.49. URL: <https://doi.org/10.5670/oceanog.2012.49>.
- [102] S. A. Thorpe. “The axial coherence of Kelvin-Helmholtz billows”. In: *Q. J. R. Meteorol. Soc.* 128.583 (July 2002), pp. 1529–1542. DOI: 10.1002/qj.200212858307. URL: <https://doi.org/10.1002/qj.200212858307>.
- [103] Gerald I. Kent. “Transverse Kelvin-Helmholtz Instability in a Rotating Plasma”. In: *Physics of Fluids* 12.10 (1969), p. 2140. DOI: 10.1063/1.1692323. URL: <https://doi.org/10.1063/1.1692323>.

- [104] Hyun Geun Lee and Junseok Kim. “Two-dimensional Kelvin–Helmholtz instabilities of multi-component fluids”. In: *European Journal of Mechanics - B/Fluids* 49 (Jan. 2015), 77–88. ISSN: 0997-7546. DOI: 10.1016/j.euromechflu.2014.08.001. URL: <http://dx.doi.org/10.1016/j.euromechflu.2014.08.001>.
- [105] Garrett Birkhoff. *Helmholtz and Taylor instability*. 1962. DOI: 10.1090/psapm/013/0137423. URL: <http://dx.doi.org/10.1090/psapm/013/0137423>.
- [106] Lord Rayleigh. “On the Stability, or Instability, of certain Fluid Motions”. In: *Proc. London Math. Soc.* s1-11.1 (Nov. 1879), pp. 57–72. DOI: 10.1112/plms/s1-11.1.57. URL: <https://doi.org/10.1112/plms/s1-11.1.57>.
- [107] Kirchhoff. In: *Vorlesungen über Mathematische Physik Mechanik* (1876).
- [108] H. Helmholtz. “Über Integrale der hydrodynamischen Gleichungen, welche den Wirbelbewegungen entsprechen.” ger. In: *Journal für die reine und angewandte Mathematik* 55 (1858), pp. 25–55. URL: <http://eudml.org/doc/147720>.
- [109] Raymond Nagem et al. “Generalized Helmholtz–Kirchhoff Model for Two-Dimensional Distributed Vortex Motion”. In: *SIAM Journal on Applied Dynamical Systems* 8.1 (Jan. 2009), 160–179. ISSN: 1536-0040. DOI: 10.1137/080715056. URL: <http://dx.doi.org/10.1137/080715056>.
- [110] Vítor Sudbrack. *Point vortex dynamics of Kelvin Helmholtz instability*. <https://www.youtube.com/watch?v=fUS3b70AdtM>. 2018.
- [111] S. E. Korshunov. “Analog of Kelvin-Helmholtz instability on a free surface of a superfluid liquid”. In: *J. Exp. Theor. Phys.* 75.8 (Apr. 2002), pp. 423–425. DOI: 10.1134/1.1490015. URL: <https://doi.org/10.1134/1.1490015>.
- [112] G. E. Volovik. “On the Kelvin-Helmholtz instability in superfluids”. In: *J. Exp. Theor. Phys.* 75.8 (2002), pp. 418–422. DOI: 10.1134/1.1490014. URL: <https://doi.org/10.1134/1.1490014>.
- [113] S. E. Korshunov. “Analog of Kelvin-Helmholtz instability on a free surface of a superfluid liquid”. In: *J. Exp. Theor. Phys.* 75.8 (Apr. 2002), pp. 423–425. DOI: 10.1134/1.1490015. URL: <https://doi.org/10.1134/1.1490015>.
- [114] A P Finne et al. “Dynamics of vortices and interfaces in superfluid ^3He ”. In: *Rep. Progr. Phys.* 69.12 (2006), p. 3157. DOI: 10.1088/0034-4885/69/12/R03. URL: <https://dx.doi.org/10.1088/0034-4885/69/12/R03>.

- [115] Hiromitsu Takeuchi et al. “Quantum Kelvin-Helmholtz instability in phase-separated two-component Bose-Einstein condensates”. In: *Phys. Rev. B* 81 (9 2010), p. 094517. DOI: 10.1103/PhysRevB.81.094517. URL: <https://link.aps.org/doi/10.1103/PhysRevB.81.094517>.
- [116] Naoya Suzuki et al. “Crossover between Kelvin-Helmholtz and counter-superflow instabilities in two-component Bose-Einstein condensates”. In: *Phys. Rev. A* 82 (6 2010), p. 063604. DOI: 10.1103/PhysRevA.82.063604. URL: <https://link.aps.org/doi/10.1103/PhysRevA.82.063604>.
- [117] E. Lundh and J.-P. Martikainen. “Kelvin-Helmholtz instability in two-component Bose gases on a lattice”. In: *Phys. Rev. A* 85 (2 2012), p. 023628. DOI: 10.1103/PhysRevA.85.023628. URL: <https://link.aps.org/doi/10.1103/PhysRevA.85.023628>.
- [118] Haruya Kokubo, Kenichi Kasamatsu, and Hiromitsu Takeuchi. “Pattern formation of quantum Kelvin-Helmholtz instability in binary superfluids”. In: *Physical Review A* 104.2 (Aug. 2021). URL: <https://doi.org/10.1103/physreva.104.023312>.
- [119] SeungJung Huh et al. *Beyond skyrmion spin texture from quantum Kelvin-Helmholtz instability*. 2024. DOI: 10.48550/ARXIV.2408.11217. URL: <https://arxiv.org/abs/2408.11217>.
- [120] D. Kobayakov et al. “Turbulence in binary Bose-Einstein condensates generated by highly nonlinear Rayleigh-Taylor and Kelvin-Helmholtz instabilities”. In: *Phys. Rev. A* 89 (1 2014), p. 013631. DOI: 10.1103/PhysRevA.89.013631. URL: <https://link.aps.org/doi/10.1103/PhysRevA.89.013631>.
- [121] A. W. Baggaley and N. G. Parker. “Kelvin-Helmholtz instability in a single-component atomic superfluid”. In: *Phys. Rev. A* 97 (5 2018), p. 053608. DOI: 10.1103/PhysRevA.97.053608. URL: <https://link.aps.org/doi/10.1103/PhysRevA.97.053608>.
- [122] Luca Giacomelli and Iacopo Carusotto. “Interplay of Kelvin-Helmholtz and superradiant instabilities of an array of quantized vortices in a two-dimensional Bose-Einstein condensate”. In: *SciPost Phys.* 14 (2023), p. 025. DOI: 10.21468/SciPostPhys.14.2.025. URL: <https://scipost.org/10.21468/SciPostPhys.14.2.025>.

- [123] G. Valtolina. “Development of an experimental apparatus for the production and study of ultracold atomic gases of fermionic lithium”. MA thesis. University of Milano - Bicocca, 2012.
- [124] G. Valtolina. “Superfluid and spin dynamics of strongly interacting atomic Fermi gases”. PhD thesis. Scuola Normale Superiore di Pisa, 2016.
- [125] Michael E. Gehm. “Preparation of an Optically-Trapped Degenerate Fermi Gas of 6 Li: Finding the Route to Degeneracy.” PhD thesis. Duke University, 2003.
- [126] C.J.Foot. *Atomic Physics*. Oxford master series, 2005.
- [127] Peter van der Straten Harold J. Metcalf. *Laser cooling and trapping*. Springer, 1999.
- [128] Miroslav Gajdacz et al. “Non-destructive Faraday imaging of dynamically controlled ultracold atoms”. In: *Review of Scientific Instruments* 84.8 (Aug. 2013), p. 083105. DOI: 10.1063/1.4818913. URL: <https://doi.org/10.1063/1.4818913>.
- [129] G. Del Pace. “Tunneling transport in strongly-interacting atomic Fermi gases”. PhD thesis. Università degli studi Firenze, 2020.
- [130] A. Burchianti et al. “Efficient all-optical production of large 6Li quantum gases using D1 gray-molasses cooling”. In: *Physical Review A* 90.4 (Oct. 2014). ISSN: 1094-1622. DOI: 10.1103/physreva.90.043408. URL: <http://dx.doi.org/10.1103/PhysRevA.90.043408>.
- [131] A. Aspect et al. “Laser Cooling below the One-Photon Recoil Energy by Velocity-Selective Coherent Population Trapping”. In: *Physical Review Letters* 61.7 (Aug. 1988), pp. 826–829. DOI: 10.1103/physrevlett.61.826. URL: <https://doi.org/10.1103/physrevlett.61.826>.
- [132] G. Zürn et al. “Precise Characterization of 6Li Feshbach Resonances Using Trap-Sideband-Resolved RF Spectroscopy of Weakly Bound Molecules”. In: *Physical Review Letters* 110.13 (Mar. 2013). ISSN: 1079-7114. DOI: 10.1103/physrevlett.110.135301. URL: <http://dx.doi.org/10.1103/PhysRevLett.110.135301>.
- [133] A. Amico. “Measurement of the Equation of State of superfluid Fermi gases of ${}^6\text{Li}$ atoms”. MA thesis. Università degli studi Firenze, 2015.

- [134] S. M. Popoff. “*wavefronthsaping/alp4lib: First release,*”. 2017.
- [135] G. Del Pace et al. “Imprinting Persistent Currents in Tunable Fermionic Rings”. In: *Physical Review X* 12.4 (Dec. 2022). ISSN: 2160-3308. DOI: 10.1103/physrevx.12.041037. URL: <http://dx.doi.org/10.1103/PhysRevX.12.041037>.
- [136] R. Sato et al. “Isothermal Compressibility of an Ultracold Fermi Gas in the BCS–BEC Crossover”. In: *Journal of Low Temperature Physics* 196.1–2 (Dec. 2018), 119–125. ISSN: 1573-7357. DOI: 10.1007/s10909-018-2103-0. URL: <http://dx.doi.org/10.1007/s10909-018-2103-0>.
- [137] Gevorg Martirosyan et al. *A universal speed limit for spreading of quantum coherence*. 2024. DOI: 10.48550/ARXIV.2410.08204. URL: <https://arxiv.org/abs/2410.08204>.
- [138] Songtao Huang et al. *Emergence of Sound in a Tunable Fermi Fluid*. 2024. DOI: 10.48550/ARXIV.2407.13769. URL: <https://arxiv.org/abs/2407.13769>.
- [139] Xi Li et al. “Second sound attenuation near quantum criticality”. In: *Science* 375.6580 (Feb. 2022), 528–533. ISSN: 1095-9203. DOI: 10.1126/science.abi4480. URL: <http://dx.doi.org/10.1126/science.abi4480>.
- [140] *personal correspondence*.
- [141] V. B. Efimov et al. “First-sound rarefaction and compression waves in superfluid He-II”. In: *Journal of Experimental and Theoretical Physics Letters* 69.10 (May 1999), 767–771. ISSN: 1090-6487. DOI: 10.1134/1.568088. URL: <http://dx.doi.org/10.1134/1.568088>.
- [142] Maren E. Mossman et al. “Dissipative shock waves generated by a quantum-mechanical piston”. In: *Nature Communications* 9.1 (Nov. 2018). ISSN: 2041-1723. DOI: 10.1038/s41467-018-07147-4. URL: <http://dx.doi.org/10.1038/s41467-018-07147-4>.
- [143] Wen Wen, Shun-Qing Shen, and Guoxiang Huang. “Propagation of sound and supersonic bright solitons in superfluid Fermi gases in BCS-BEC crossover”. In: *Physical Review B* 81.1 (Jan. 2010). ISSN: 1550-235X. DOI: 10.1103/physrevb.81.014528. URL: <http://dx.doi.org/10.1103/PhysRevB.81.014528>.

- [144] Luca Pezzè et al. “Stabilizing persistent currents in an atomtronic Josephson junction necklace”. In: *Nature Communications* 15.1 (June 2024). ISSN: 2041-1723. DOI: 10.1038/s41467-024-47759-7. URL: <http://dx.doi.org/10.1038/s41467-024-47759-7>.
- [145] S. Eckel et al. “Interferometric Measurement of the Current-Phase Relationship of a Superfluid Weak Link”. In: *Physical Review X* 4.3 (Sept. 2014). ISSN: 2160-3308. DOI: 10.1103/physrevx.4.031052. URL: <http://dx.doi.org/10.1103/PhysRevX.4.031052>.
- [146] Joachim Brand and William P Reinhardt. “Generating ring currents, solitons and svortices by stirring a Bose-Einstein condensate in a toroidal trap”. In: *Journal of Physics B: Atomic, Molecular and Optical Physics* 34.4 (Feb. 2001), L113–L119. ISSN: 1361-6455. DOI: 10.1088/0953-4075/34/4/105. URL: <http://dx.doi.org/10.1088/0953-4075/34/4/105>.
- [147] Stuart Moulder et al. “Quantized supercurrent decay in an annular Bose-Einstein condensate”. In: *Physical Review A* 86.1 (July 2012). ISSN: 1094-1622. DOI: 10.1103/physreva.86.013629. URL: <http://dx.doi.org/10.1103/PhysRevA.86.013629>.
- [148] C. Ryu et al. “Observation of Persistent Flow of a Bose-Einstein Condensate in a Toroidal Trap”. In: *Physical Review Letters* 99.26 (Dec. 2007). ISSN: 1079-7114. DOI: 10.1103/physrevlett.99.260401. URL: <http://dx.doi.org/10.1103/PhysRevLett.99.260401>.
- [149] Yanping Cai et al. “Persistent Currents in Rings of Ultracold Fermionic Atoms”. In: *Physical Review Letters* 128.15 (Apr. 2022). ISSN: 1079-7114. DOI: 10.1103/physrevlett.128.150401. URL: <http://dx.doi.org/10.1103/PhysRevLett.128.150401>.
- [150] Avinash Kumar et al. “Producing superfluid circulation states using phase imprinting”. In: *Physical Review A* 97.4 (Apr. 2018). ISSN: 2469-9934. DOI: 10.1103/physreva.97.043615. URL: <http://dx.doi.org/10.1103/PhysRevA.97.043615>.
- [151] N. Grani. “Instability of persistent currents in fermionic superfluid rings”. MA thesis. Università degli studi Firenze, 2021.
- [152] FEDRIZZI MARCO. “OBSERVING PERSISTENT CURRENTS IN ANNULAR FERMIONIC SUPERFLUIDS”. MA thesis. University of Milano, 2021.

- [153] B G Swingle and T A B Kennedy. “Generation of topological flows by phase imprinting”. In: *Journal of Physics B: Atomic, Molecular and Optical Physics* 38.19 (Sept. 2005), 3503–3515. ISSN: 1361-6455. DOI: 10.1088/0953-4075/38/19/004. URL: <http://dx.doi.org/10.1088/0953-4075/38/19/004>.
- [154] Ke-Ji Chen, Wei Yi, and Fan Wu. *Dynamic Generation of Superflow in a Fermionic Ring through Phase Imprinting*. 2024. DOI: 10.48550/ARXIV.2406.00289. URL: <https://arxiv.org/abs/2406.00289>.
- [155] Masaya Kunimi and Ippei Danshita. “Decay mechanisms of superflow of Bose-Einstein condensates in ring traps”. In: *Physical Review A* 99.4 (Apr. 2019). ISSN: 2469-9934. DOI: 10.1103/physreva.99.043613. URL: <http://dx.doi.org/10.1103/PhysRevA.99.043613>.
- [156] S. Eckel et al. “Interferometric Measurement of the Current-Phase Relationship of a Superfluid Weak Link”. In: *Phys. Rev. X* 4 (3 2014), p. 031052. DOI: 10.1103/PhysRevX.4.031052. URL: <https://link.aps.org/doi/10.1103/PhysRevX.4.031052>.
- [157] W. J. Kwon et al. “Strongly correlated superfluid order parameters from dc Josephson supercurrents”. In: *Science* 369.6499 (July 2020), pp. 84–88. DOI: 10.1126/science.aaz2463. URL: <https://doi.org/10.1126/science.aaz2463>.
- [158] Jérôme Beugnon and Nir Navon. “Exploring the Kibble–Zurek mechanism with homogeneous Bose gases”. In: *Journal of Physics B: Atomic, Molecular and Optical Physics* 50.2 (Jan. 2017), p. 022002. ISSN: 1361-6455. DOI: 10.1088/1361-6455/50/2/022002. URL: <http://dx.doi.org/10.1088/1361-6455/50/2/022002>.
- [159] Toshiaki Kanai, Wei Guo, and Makoto Tsubota. “Merging of Rotating Bose-Einstein Condensates”. In: *J. Low. Temp. Phys.* 195.1-2 (Apr. 2019), pp. 37–50. DOI: 10.1007/s10909-018-2110-1.
- [160] Toshiaki Kanai, Wei Guo, and Makoto Tsubota. “Merging of Rotating Bose–Einstein Condensates”. In: *Journal of Low Temperature Physics* 195.1–2 (Dec. 2018), 37–50. ISSN: 1573-7357. DOI: 10.1007/s10909-018-2110-1. URL: <http://dx.doi.org/10.1007/s10909-018-2110-1>.

- [161] J. Denschlag et al. “Generating Solitons by Phase Engineering of a Bose-Einstein Condensate”. In: *Science* 287.5450 (Jan. 2000), 97–101. ISSN: 1095-9203. DOI: 10.1126/science.287.5450.97. URL: <http://dx.doi.org/10.1126/science.287.5450.97>.
- [162] Tarik Yefsah et al. “Heavy solitons in a fermionic superfluid”. In: *Nature* 499.7459 (July 2013), 426–430. ISSN: 1476-4687. DOI: 10.1038/nature12338. URL: <http://dx.doi.org/10.1038/nature12338>.
- [163] A. Farolfi et al. “Observation of Magnetic Solitons in Two-Component Bose-Einstein Condensates”. In: *Physical Review Letters* 125.3 (July 2020). ISSN: 1079-7114. DOI: 10.1103/physrevlett.125.030401. URL: <http://dx.doi.org/10.1103/PhysRevLett.125.030401>.
- [164] B. P. Anderson et al. “Watching Dark Solitons Decay into Vortex Rings in a Bose-Einstein Condensate”. In: *Physical Review Letters* 86.14 (Apr. 2001), 2926–2929. ISSN: 1079-7114. DOI: 10.1103/physrevlett.86.2926. URL: <http://dx.doi.org/10.1103/PhysRevLett.86.2926>.
- [165] Giulia Del Pace et al. *Shapiro steps in strongly-interacting Fermi gases*. 2024. DOI: 10.48550/ARXIV.2409.03448. URL: <https://arxiv.org/abs/2409.03448>.
- [166] Wout Van Alphen, Hiromitsu Takeuchi, and Jacques Tempere. “Crossover between snake instability and Josephson instability of dark solitons in superfluid Fermi gases”. In: *Physical Review A* 100.2 (2019), p. 023628.
- [167] Giovanni Lombardi et al. “Snake instability of dark solitons across the BEC-BCS crossover: An effective-field-theory perspective”. In: *Physical Review A* 96.3 (2017), p. 033609.
- [168] A Cetoli et al. “Snake instability of dark solitons in fermionic superfluids”. In: *Physical Review A* 88.4 (2013), p. 043639.
- [169] Mark JH Ku et al. “Cascade of solitonic excitations in a superfluid fermi gas: From planar solitons to vortex rings and lines”. In: *Physical Review Letters* 116.4 (2016), p. 045304.
- [170] Michael Tinkham. *Introduction to Superconductivity: v. 1*. 2nd ed. Dover Books on Physics. Mineola, NY: Dover Publications, June 2004.

- [171] K. Xhani et al. “Critical Transport and Vortex Dynamics in a Thin Atomic Josephson Junction”. In: *Phys. Rev. Lett.* 124 (4 2020), p. 045301. DOI: 10.1103/PhysRevLett.124.045301. URL: <https://link.aps.org/doi/10.1103/PhysRevLett.124.045301>.
- [172] Giacomo Valtolina et al. “Josephson effect in fermionic superfluids across the BEC-BCS crossover”. In: *Science* 350.6267 (Dec. 2015), 1505–1508. ISSN: 1095-9203. DOI: 10.1126/science.aac9725. URL: <http://dx.doi.org/10.1126/science.aac9725>.
- [173] Viacheslav V. Dremov et al. “Local Josephson vortex generation and manipulation with a Magnetic Force Microscope”. In: *Nature Communications* 10.1 (Sept. 2019). ISSN: 2041-1723. DOI: 10.1038/s41467-019-11924-0. URL: <http://dx.doi.org/10.1038/s41467-019-11924-0>.
- [174] Arkady Pikovsky and Antonio Politi. *Lyapunov exponents*. Cambridge: Cambridge University Press, 2016.
- [175] B E Warren. *X-Ray Diffraction*. Dover Books on Physics. Mineola, NY: Dover Publications, 1990.
- [176] Allan Griffin, Tetsuro Nikuni, and Eugene Zaremba. *Bose-Condensed Gases at Finite Temperatures*. Cambridge University Press, 2009. DOI: 10.1017/CB09780511575150.
- [177] K. Xhani and N. P. Proukakis. “Dissipation in a finite-temperature atomic Josephson junction”. In: *Physical Review Research* 4.3 (Sept. 2022). ISSN: 2643-1564. DOI: 10.1103/physrevresearch.4.033205. URL: <http://dx.doi.org/10.1103/PhysRevResearch.4.033205>.
- [178] Max Heyl et al. “Vortex dynamics in the two-dimensional BCS-BEC crossover”. In: *Nature Communications* 13.1 (Nov. 2022). ISSN: 2041-1723. DOI: 10.1038/s41467-022-34756-x. URL: <http://dx.doi.org/10.1038/s41467-022-34756-x>.
- [179] Biswaroop Mukherjee et al. “Crystallization of bosonic quantum Hall states in a rotating quantum gas”. In: *Nature* 601.7891 (Jan. 2022), pp. 58–62. DOI: 10.1038/s41586-021-04170-2. URL: <https://doi.org/10.1038/s41586-021-04170-2>.

- [180] Brynmor Haskell and Andrew Melatos. “Models of pulsar glitches”. In: *Int. J. Mod. Phys. D* 24.03 (2015), p. 1530008. DOI: 10.1142/S0218271815300086. URL: <https://doi.org/10.1142/S0218271815300086>.
- [181] D. J. Price and S. Rosswog. “Producing Ultrastrong Magnetic Fields in Neutron Star Mergers”. In: *Science* 312.5774 (2006), pp. 719–722. DOI: 10.1126/science.1125201. URL: <https://www.science.org/doi/abs/10.1126/science.1125201>.
- [182] E. A. L. Henn et al. “Emergence of Turbulence in an Oscillating Bose-Einstein Condensate”. In: *Phys. Rev. Lett.* 103 (4 2009), p. 045301. DOI: 10.1103/PhysRevLett.103.045301. URL: <https://link.aps.org/doi/10.1103/PhysRevLett.103.045301>.